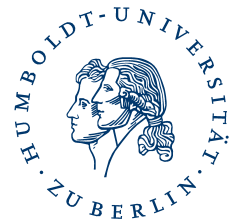


HUMBOLDT-UNIVERSITÄT ZU BERLIN



Mathematisch-Naturwissenschaftliche Fakultät I
Institut für Physik

Search for Neutrino Emission from Supernova 2008D with IceCube

Diplomarbeit

URL: http://www-zeuthen.desy.de/~knick/Diplomarbeit_NiklausKemming.pdf

Niklaus Kemming
Februar 2010

Abstract

Core-collapse supernovae - explosions of very massive “burnt-out” stars - are among the most spectacular phenomena in the universe. They can be observed across the electromagnetic spectrum but are also hypothesized to emit high energy neutrinos detectable by modern neutrino observatories such as IceCube. This analysis searches for neutrinos emitted by Supernova 2008D, the first core collapse supernova to be directly observed before, during, and after the explosion of the stellar envelope. The analysis uses 275 days of data recorded by the 25% completed IceCube-detector in 2007 and 2008. The data is used to determine and reduce the expected background. The characteristics of the expected neutrino signal are simulated in Monte-Carlo studies using a slow jet model and the observed parameters of SN2008D from optical, X-ray, and radio measurements. A multivariate selection cut tailored to the position of SN 2008D and to the slow jet spectrum is developed and optimized for a discovery at a significance level of 5σ . Finally, the search is performed on data from January 9, 2008 using three overlapping temporal and angular search windows. No neutrinos passing the final selection cuts were observed. Assuming that one of the jets predicted by the model is pointing towards Earth, this result yields upper limits on the muon neutrino flux according to the slow jet model for different emission time scales τ_e given by:

$$\Phi_{\nu,\mu\ell}^{(90)}(100 \text{ GeV}) = \begin{cases} 4.8 \times 10^{-3} & \text{for } \tau_e = 100 \text{ s} \\ 8.0 \times 10^{-3} & \text{for } \tau_e = 1,000 \text{ s} \\ 2.4 \times 10^{-2} & \text{for } \tau_e = 10,000 \text{ s} \end{cases}$$

in units of $\text{GeV}^{-1} \text{cm}^{-2}$ and at a confidence level of 90%.

Zusammenfassung

Kernkollaps-Supernovae - Explosionen massiver, "ausgebrannter" Sterne - gehören zu den spektakulärsten Phänomenen im Universum. Sie können in allen Bereichen des elektromagnetischen Spektrums beobachtet werden und sind vermutlich auch Quellen hochenergetischer Neutrinos, die sich mit modernen Neutrinodetektoren wie IceCube beobachten lassen. In der vorliegenden Arbeit wurde nach Neutrinos von Supernova 2008D gesucht, der ersten Kernkollaps-Supernova, die vor, während und nach der Explosion der stellaren Hülle beobachtet wurde. Die Analyse stützt sich auf einen Datensatz, den der zu 25% fertiggestellte IceCube-Detektor über 275 Tage in den Jahren 2007-2008 aufgenommen hat. Mithilfe dieser Daten, wurde die Rate von Hintergrundereignissen bestimmt und reduziert. Das erwartete Neutrinosignal wurde in Monte-Carlo-Studien nach dem Slow-Jet-Modell simuliert, das an die beobachteten Parameter von SN 2008D aus optischen, Röntgen- und Radiomessungen angepasst wurde. Multivariate, auf die Position von SN 2008D und das Slow-Jet-Modell maßgeschneiderte Selektionsschnitte wurden entwickelt und für eine Entdeckung mit einer Signifikanz von 5σ optimiert. Schließlich, wurden die Daten vom 9. Januar 2008 innerhalb dreier ineinander geschachtelter Zeit- und Winkelfenster und anhand der Selektionsschnitte nach Neutrinos durchsucht. Dabei wurden keine Ereignisse gefunden, welche die Selektionsschnitte passierten. Unter der Annahme, dass die im verwendeten Modell postulierten Jets in Richtung der Erde zeigten, ergibt sich daraus eine Obergrenze für den Myonneutrinofluss nach dem Slow-Jet-Modell für die jeweilige Emissions-Zeitskala τ_e von:

$$\Phi_{\nu,\mu\ell}^{(90)}(100 \text{ GeV}) = \begin{cases} 4.8 \times 10^{-3} & \text{für } \tau_e = 100 \text{ s} \\ 8.0 \times 10^{-3} & \text{für } \tau_e = 1,000 \text{ s} \\ 2.4 \times 10^{-2} & \text{für } \tau_e = 10,000 \text{ s} \end{cases}$$

in Einheiten von $\text{GeV}^{-1}\text{cm}^{-2}$ bei 90% Vertrauensniveau.

Contents

1	Introduction	11
2	Neutrinos	13
2.1	Properties	13
2.2	Discovery	13
2.3	Electro-Weak Theory	14
2.4	Neutrino Production	15
2.4.1	Low Energy: β^\pm -decay and e^\pm -capture	16
2.4.2	High Energy: Charged-meson-decay	16
2.5	Low Energy Neutrino Sources	17
2.6	High Energy Neutrino Sources	17
2.6.1	Cosmic Rays	18
2.6.2	Cosmic Accelerators	19
2.6.3	Gamma Ray Bursts (GRB)	19
2.6.4	Active Galaxies	21
3	Supernovae as Neutrino Sources	23
3.1	Supernovae: Properties and Terminology	24
3.1.1	Type Ia	24
3.1.2	Type Ib,Ic,II	24
3.2	Supernova Neutrinos	25
3.2.1	Low Energy	25
3.2.2	High Energy	25
3.3	Supernova-Gamma Ray Burst Connection	26
3.4	Supernova 2008D	27
3.5	Slow Jet Model	29
3.5.1	Phenomenology	29
3.5.2	Analytical Form	31
4	Neutrino Detection	35
4.1	Neutrino Propagation	35
4.1.1	Flavor Oscillations	35
4.1.2	Time Delay	37
4.2	Neutrino Interactions	37
4.3	Muon Propagation	38
4.3.1	Estimated Number of Events for a Supernova at 10 Mpc	39
4.4	Cherenkov Radiation	40
4.5	The IceCube Detector	41

4.5.1	Geometry	42
4.5.2	Coordinate System	43
4.5.3	Hardware	43
4.5.4	Software	44
5	Analysis of SN 2008D	47
5.1	Methodology	48
5.2	Background Data	48
5.2.1	Reducible Background	49
5.2.2	Irreducible Background	50
5.2.3	Necessary Statistics	50
5.3	Data Processing in IceCube	52
5.3.1	Reconstruction Basics	52
5.3.2	First-Guess Line Fit	53
5.3.3	Likelihood Track Reconstruction	54
5.3.4	Umbrella Track Reconstruction	55
5.3.5	Bayesian Likelihood Track Reconstruction	56
5.3.6	Split Track Reconstruction	56
5.3.7	Paraboloid Fit	56
5.3.8	Quality Parameters	58
5.3.9	Processing and Filtering Levels	59
5.4	Signal Simulation	60
5.4.1	Simulation Production	60
5.4.2	Properties of Simulated Signal	61
5.4.3	Signal Expectation	62
5.5	Background Simulation	62
5.5.1	Atmospheric Muons	62
5.5.2	Atmospheric Neutrinos	63
5.5.3	Expected Irreducible Background	63
5.6	Search Window	64
5.6.1	Temporal Size - Time Window	64
5.6.2	Angular Size - Aperture	65
5.7	Event Selection	67
5.7.1	Cut Parameters	67
5.7.2	Multivariate Classifiers	69
5.7.3	Boosted Decision Trees	70
5.7.4	Model Discovery Factor	74
5.7.5	Optimization for Discovery	75
5.7.6	Final Cuts	78
5.8	Significance	79
5.8.1	Monte Carlo Study	79
5.8.2	Significances of Possible Observations	79
5.9	Error Analysis	80
5.9.1	Direction Reconstruction	81
5.9.2	Cut Efficiencies	82
5.9.3	Background Measurement	83
5.9.4	Signal Simulation	83

6 Results	85
6.0.5 Unblinding	85
6.0.6 Limits on the Slow Jet Model	86
6.0.7 Summary and Outlook	87
A Apppendix A	89
A.1 Important Symbols and Abbreviations	89
A.1.1 Abbreviations	89
A.1.2 Symbols	89
A.2 Detailed Significances	90
A.3 Data-Monte-Carlo Comparison	91
A.4 Comparison with Point Source Cuts	93
B Appendix B	95
B.1 Acknowledgments	95
B.2 Erklärung	96

Chapter 1

Introduction

Supernova 2008D was a stroke of luck for astrophysics and a unique event in the long history of supernova observations. These spectacular explosions of stars were first observed more than a thousand years ago, when SN 1006 was visible to the naked eye as a bright disc in the night sky, fading from a quarter the brightness of the full moon into obscurity over the course of several months [1]. Contemporary astronomers noted that the flash could not be a comet since it did not move in the sky, yet the idea that the shining object was an exploding star shedding over a billion times more light than the sun - an established fact today [2] - would have certainly seemed preposterous at the time. Since then, astronomers have studied supernovae with ever more sophisticated methods. Using visible light as a probe, however, they never saw more than the aftermath of the actual explosion: a cloud of debris ejected by the explosion - completely concealing the core.

To catch supernovae in the act of exploding and to look inside the collapsing core, the all-penetrating neutrino constitutes an ideal probe. But it was not until 1987, that a burst of neutrinos was detected in association with a supernova within our galaxy. These low energy neutrinos, produced in well-known fusion reactions in the core provided valuable information about the physics of the explosion. High energy neutrinos, if detected, could not only extend the reach on neutrino astronomy to extragalactic objects - for the subclass of core collapse supernovae, they could also constrain acceleration scenarios and verify the hypothesized connection between core collapse supernovae and long duration γ -ray bursts.

Supernova 2008D, the subject of this analysis, offers a realistic chance to detect high energy supernova neutrinos for the first time. It was serendipitously discovered as an X-ray flash *before* the optical signature of a core collapse supernova was recorded. The observed X-ray peak provides the most precise time information ever available to a study searching for high energy neutrinos from a supernova.

The IceCube neutrino detector currently under construction at the South Pole and scheduled for completion in 2011, is capable of detecting high energy neutrinos of cosmic origin by measuring the light tracks of secondary muons in the transparent deep ice. When SN 2008D was observed, the installation IceCube was about one quarter completed and the detector was already taking data. Using this data, this analysis searches for neutrinos emitted by SN 2008D according to the “slow jet model” [42], [43]. The principal goals motivating this analysis are to:

- develop new methods for IceCube analyses tailored to specific cosmic events or sources with maximum sensitivity;
- show IceCube's capability to detect cosmic neutrinos;
- demonstrate that IceCube is sensitive to a real astrophysical event;
- probe the hypothesized connection between γ -ray bursts and core collapse supernovae;
- and to derive constraints on the slow jet model for core collapse supernovae.

Chapter 2 summarizes the necessary theoretical background on neutrinos, chapter 3 discusses the physics of supernovae as well as the slow jet model for the production of ultrarelativistic neutrinos, chapter 4 describes the principles of neutrino detection and the IceCube detector. In chapter 5, the analysis of IceCube data and the development of a search method optimized for SN 2008D is detailed. Finally, the results of the search are presented and interpreted in chapter 6.

Chapter 2

Neutrinos

Since this analysis is part of an effort to use neutrinos as messenger particles to study astrophysical sources, a brief overview of the properties, discovery, theoretical treatment, and production mechanisms of these unusual particles shall be given.

2.1 Properties

At the current state of knowledge, neutrinos are elementary i.e. indivisible particles populating the entire universe. They are literally all around us and trillions of neutrinos pass through a human body every second. Neutrinos share some of their properties with light: They are never found at rest and travel *practically* at the speed of light¹. Possessing no electrical charge, they experience no deflection in electromagnetic fields. Like photons, neutrinos can be polarized, yet in nature only left handed polarization² appears to be realized (the spin and momentum vectors are anti-parallel). In contrast to photons, neutrinos have a mass, although their mass is hardly measurable. Neutrinos are only subject to the weak force. While photons are scattered or absorbed by charged particles, neutrinos can penetrate concrete walls, mountains, planets, even stars almost unimpeded and interact with ordinary matter extremely seldom. This ghostlike property hints at the aptitude of neutrinos as messenger particles and has two important consequences for their study: First, neutrinos can carry information from e.g. the center of a star or galaxy directly to a terrestrial observer. Second, the terrestrial observer has a rather small chance of detecting a neutrino. Due to the latter, neutrinos although abundant and long-lived, were not discovered until 1956.

2.2 Discovery

The existence of the neutrino was theoretically postulated by Wolfgang Pauli in 1930 to preserve the conservation of energy and momentum in neutron decays [4], but it was not until 1956 that it was detected by Clyde Cowan and Frederick Reines in a reactor experiment [6].

¹This statement is only valid for those neutrinos that have been experimentally detected thus far, i.e. neutrinos with energies $E_\nu \gtrsim \text{MeV}$. For cosmic background neutrinos $\beta \ll 1$ is assumed.

²For neutrinos, the term helicity is more commonly used to describe the alignment/anti-alignment of momentum and spin. However, on account of their small mass, helicity is not conserved for neutrinos, it depends on the reference frame. Instead, the generalized concept of chirality - the eigenvalue of the γ_5 operator, a Lorentz-invariant observable - is used to characterize massive particles. Only fermions of defined chirality, i.e. left- or right-handed fermions, take part in standard model interactions.

Cowan and Reines used a nuclear reactor to produce a flux of 5×10^{13} neutrinos per second per square centimeter. Neutrinos were detected through their interactions with protons in a tank of water producing a neutron and a positron. The subsequent annihilation of the positron into two photons and the gamma radiation from the neutron capture by Cadmium atoms provided an unambiguous signature to identify the reaction.

To be precise, Cowan and Reines discovered the electron antineutrino. It was soon realized and experimentally verified in 1959 by the Brookhaven AGS experiment, that the neutrino produced in pion decays along with a muon is different from that emitted in β^- -decays along with an electron [7]. When the third meson, the tauon was detected in 1975, the existence of a third neutrino seemed theoretically inevitable. The tau neutrino was eventually detected by DONUT in 2000 [8]. Table 2.1 lists the basic properties of the neutrino.

Name	Electron Neutrino	Muon Neutrino	Tau Neutrino
Symbol	ν_e	ν_μ	ν_τ
Electric charge	0	0	0
Spin	$\frac{1}{2}$	$\frac{1}{2}$	$\frac{1}{2}$
Chirality	-1	-1	-1
Mass	$< 2.2 \text{ eV}/c^2$	$< 190 \text{ keV}/c^2$	$< 18.2 \text{ MeV}/c^2$

Table 2.1: Summary of neutrino properties. Masses are to be understood as expectation values. Based on [5].

2.3 Electro-Weak Theory

The standard model of particle physics has been overwhelmingly successful in describing interactions of all known elementary particles. It encompasses twelve elementary particles, six quarks and six leptons as well as their antiparticles. Interactions between elementary particles (fermions) are mediated by exchange particles (bosons) [9].

Mathematically, the standard model is a non-abelian gauge theory. It evolved from the theory of electro-weak interactions which earned Glashow, Weinberg, and Salam the Nobel Prize in 1979 and was later extended to include the strong nuclear force to become the standard model. The gauge group of the standard model, $SU(3)_C \times SU(2)_L \times SU(1)_Y$, describes generalized rotations in the vector space spanned by color C (three dimensions), weak isospin L (two dimensions), and weak hypercharge Y (one dimension) [10].

$$\begin{array}{ccc}
 \text{Quarks:} & \text{Leptons:} & \text{Bosons:} \\
 \left(\begin{array}{c} u \\ d \end{array} \right)_{L,R} & \left(\begin{array}{c} c \\ s \end{array} \right)_{L,R} & \left(\begin{array}{c} t \\ b \end{array} \right)_{L,R} & \left(\begin{array}{c} e \\ \nu_e \end{array} \right)_L & \left(\begin{array}{c} \mu \\ \nu_\mu \end{array} \right)_L & \left(\begin{array}{c} \tau \\ \nu_\tau \end{array} \right)_L & Z^0 & W^+ & g \\
 & & & e_R & \mu_R & \tau_R & \gamma & W^- & (H)
 \end{array}$$

Figure 2.1: Elementary particles of the standard model. For quarks and leptons, Arabic and Greek letters denote Dirac spinors of defined chirality L or R . Both quarks and leptons are organized in three 'families'. Note that right-handed neutrinos do not exist in the standard model.

The standard model is based on two fundamental principles: relativistic covariance, which leads to the description of fundamental particles by Dirac spinors, complex fermion fields (4-spinors) with defined handedness, and local gauge invariance, which results in the introduction of gauge bosons, particles that are exchanged whenever two elementary fermions interact. Because some of these exchange particles carry not only charge, but also mass, theorists had to sacrifice the principle of gauge invariance and include another fundamental boson, the Higgs H to the standard model, which is still to be detected. Figure 2.1 gives an overview of the standard model particles based on [11].

Interactions of elementary particles can be visualized with Feynman diagrams which translate directly into mathematical rules to calculate interaction probabilities and cross sections, the fundamental quantities of interest in an experiment (see e.g. [12]). While in this analysis, neutrino *production* is modeled in a simplified manner combining experimentally measured parameters with basic assumptions³, neutrino *detection* is simulated using numerically computed interaction probabilities. It should be noted that such calculations are perturbative and approximate in character and the predicted cross sections become increasingly inaccurate at extreme energies. While they have proven precise for purely electro-weak interactions, the complex strong interactions responsible for the substructure of e.g. protons and neutrons can still not be described in a satisfactory way by perturbative calculations. Instead, nuclear form factors are empirically measured and manually inserted into fundamental quark-neutrino cross sections to account for the nuclear structure [55].

2.4 Neutrino Production

The fundamental interactions in which neutrinos are produced shall be illustrated by the corresponding Feynman graphs (see e.g. [5]). With the abbreviations: $q_u \in \{u, c, t\}$ and $q_d \in \{d, s, b\}$ for up quarks and down quarks, $\ell \in \{e, \mu, \tau\}$ for leptons and X for hypothetical, weakly interacting particles, neutrino producing interactions can be summarized in four groups:

Figure 2.2: Neutrino production through charged boson annihilation.

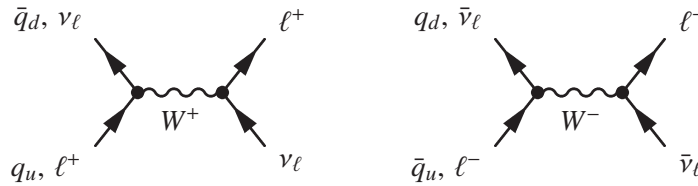
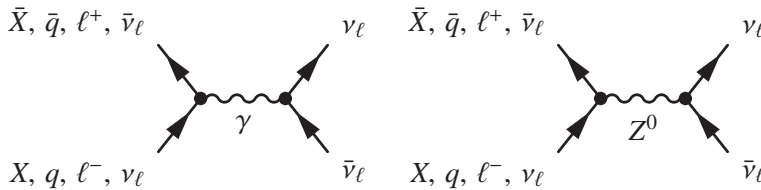
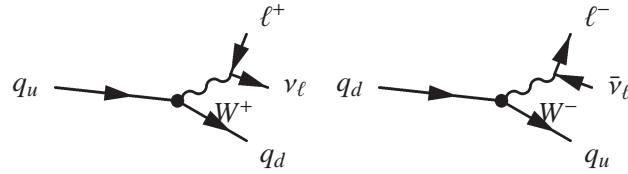
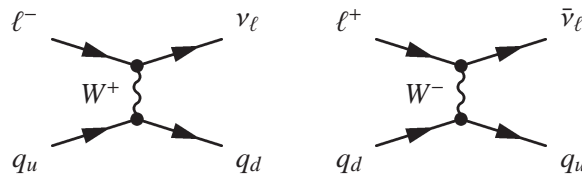


Figure 2.3: Neutrino pair production from photons (left) or neutral bosons (right).



³For example simply assuming one neutrino is produced per accelerated proton carrying $\frac{1}{8}$ of its energy.

Figure 2.4: Neutrino production through quark flavor conversion.**Figure 2.5:** Neutrino production through lepton decay with charged boson exchange and quark flavor change.

The symbol X was included to illustrate the potential of neutrinos contributing to the detection of new particles, e.g. the weakly interacting massive particle (WIMP).

In practice, free quarks are not observed and any quark q taking part in the above interactions must be part of a baryon ($|qqq\rangle$; neutron, proton, etc.) or meson ($|q\bar{q}\rangle$; pion, kaon, etc.). Therefore production mechanisms can be classified according to the participating baryon/meson.

2.4.1 Low Energy: β^\pm -decay and e^\pm -capture

Beta decay and electron/positron capture are responsible for the production of low energy neutrinos in nuclear fusion and fission reactions. Both are irrelevant to this analysis and shall therefore be stated without any further discussion:

$$n \longrightarrow p + e^- + \bar{\nu}_e \quad (\beta^- \text{-decay}) \qquad p \longrightarrow n + e^+ + \nu_e \quad (\beta^+ \text{-decay}) \quad (2.1)$$

$$e^- + p \longrightarrow n + \nu_e \quad (e^- \text{-capture}) \qquad e^+ + n \longrightarrow p + \bar{\nu}_e \quad (e^+ \text{-capture}) \quad (2.2)$$

2.4.2 High Energy: Charged-meson-decay

When charged mesons, bound quark-antiquark states, decay, a constituent quark undergoes the process shown in Fig. 2.2, a neutrino is produced. Of all mesons, only charged pions and kaons make a relevant contribution to the neutrino production in realistic astrophysical or laboratory settings. These particles are produced abundantly in ultrarelativistic particle collisions when the center of mass energy fragments into a hadronic/electromagnetic cascade. This process has been studied in detail in particle colliders such as Tevatron⁴ (proton-antiproton collisions). In astrophysical settings, due to the dominance of hydrogen, proton-proton and proton-photon collisions are the prevalent source of pions and kaons:

$$p + p \longrightarrow \dots \pi^\pm / K^\pm \quad (2.3)$$

$$p + \gamma \longrightarrow \Delta^+ \longrightarrow n \pi^+ \quad (2.4)$$

Since kaons have a much higher rest mass than pions ($m_{\pi^\pm} = 139.57 \text{ MeV}$, $m_{K^\pm} = 493.78 \text{ MeV}$), they are produced in greater numbers as the center of mass energy rises.

⁴<http://www-bdnew.fnal.gov/tevatron/>

After production charged pions and kaons rapidly ($\tau \sim 10^{-8}$ s) decay in the following reactions:

$$\pi^+ \longrightarrow \ell^+ \nu_\ell \quad \pi^- \longrightarrow \ell^- \bar{\nu}_\ell \quad (2.5)$$

$$K^+ \longrightarrow \ell^+ \nu_\ell \quad K^- \longrightarrow \ell^- \bar{\nu}_\ell \quad (2.6)$$

where pions decay quasi exclusively into the end states $\mu^\pm + \nu_\mu (\bar{\nu}_\mu)$ with a branching ratio of $> 99.9\%$. For kaons, this branching ratio is reduced to 63.5% by concurrent hadronic and semileptonic decay modes. A pion or kaon decay into a $\tau \nu_\tau$ pair is ruled out by the large mass of the tauon ($m_\tau = 1.78 \text{ GeV} \gg m_{K^\pm}, m_{\pi^\pm}$). After a mean lifetime of $\tau_\mu = 2.2 \mu\text{s}$, muons further decay into electrons:

$$\mu^- \longrightarrow e^- \bar{\nu}_e \nu_\mu \quad \mu^+ \longrightarrow e^+ \nu_e \bar{\nu}_\mu \quad (2.7)$$

In short notation, the relevant mechanism for production read as follows:

$$p + X \longrightarrow \dots \pi^\pm / K^\pm \longrightarrow e^\pm \bar{\nu}_e \nu_\mu \bar{\nu}_\mu (e^\pm \nu_e \bar{\nu}_\mu \nu_\mu) \quad (2.8)$$

Neutrinos produced in these decays can have almost arbitrarily large energies, with an upper limit set by the energy of the parent protons (a more precise picture will be given in Sec. 3.5). In cosmic ray experiments, protons with energies of $\sim 10^{20}$ eV have been observed. These high energy protons should produce neutrinos of similar energies. Their mere existence proves that cosmic accelerators can boost particles to such extreme energies unreachable in terrestrial experiments. Thus, the search for sources of ultrarelativistic neutrinos is essentially a search for cosmic accelerators.

2.5 Low Energy Neutrino Sources

Although neutrinos produced by β^\pm -decay and e^\pm -capture have energies $E_\nu \sim \text{MeV}$ far below the threshold of this analysis, virtually all of our knowledge about neutrinos has been obtained from MeV-neutrinos. They represent the foundation of the emerging field of high energy neutrino physics and shall be summarized briefly:

- **Nuclear Reactors** produce neutrinos in fission reactions through the β^\pm -decay and e^\pm -capture of unstable isotopes
- **The Sun** emits a steady flux of *solar neutrinos*, produced in nuclear fusion reactions in the center of the sun
- **Cosmic Background Neutrinos** are believed to be an omnipresent remnant of $e^+e^- \leftrightarrow \nu\bar{\nu}$ reactions in the primordial plasma

2.6 High Energy Neutrino Sources

High energy or ultrarelativistic neutrinos ($E_\nu \gtrsim 100 \text{ GeV}$) produced in charged pion and kaon decays have been proven to be produced in terrestrial accelerators (skipped here), in cosmic ray showers and are believed to originate from certain astrophysical sources.

2.6.1 Cosmic Rays

Cosmic rays take an intermediary role between terrestrial and cosmic sources. Cosmic rays are composed of ultrarelativistic charged particles (protons, alpha particles, heavy ions) hitting the Earth's atmosphere isotropically from all directions at a constant rate. The spectrum and composition of cosmic rays has been studied for almost a century. In fact, measuring the cosmic ray spectrum and composition at high energies is one of the scientific goals of IceCube (IceTop array).

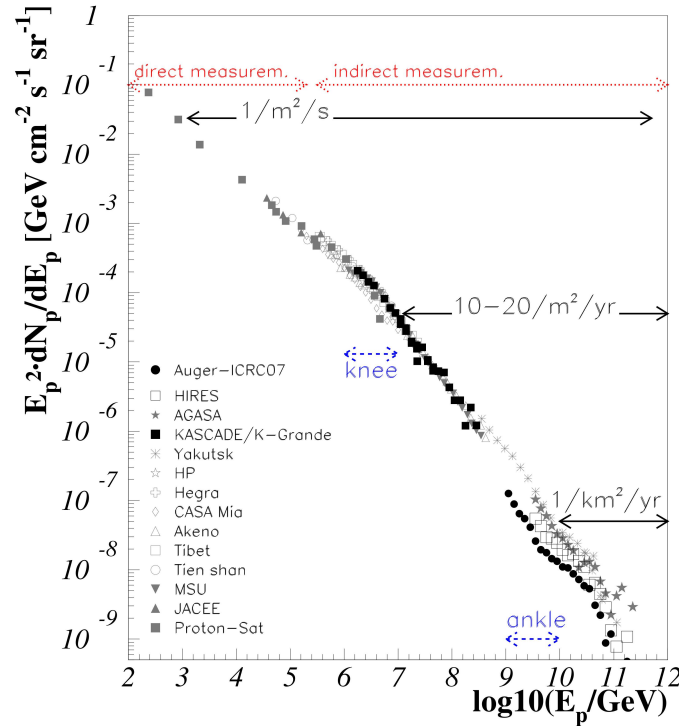


Figure 2.6: All particle cosmic ray spectrum, E_p^2 -weighted. Symbols indicate measurements by a number of experiments. From [13].

When cosmic rays collide with particles of the upper atmosphere, they initiate hadronic cascades (also called showers) encompassing neutrino production via the reaction 2.8. At high energies $E_\nu \gtrsim 10^5$ GeV, the decay of charmed D -mesons is also believed to contribute so called *prompt* atmospheric neutrinos which have, however, not been measured to date. While electrons, photons, mesons and baryons are efficiently absorbed in the atmosphere, neutrinos as well as muons reach the Earth's surface in large numbers. Whether muons reach the surface or not depends on their energy (decay length) and their stochastic energy loss (for details, see Sec. 4.3), however, muons are the most copious shower particles detectable at the surface. The observed spectra of atmospheric muons and muon neutrinos at the surface are shown in Fig. 2.7. Since muons are completely absorbed by the Earth, their directions only range from down-going to horizontal. Neutrinos, in contrast, can traverse the Earth and are therefore coming from all angles including vertically upwards. At neutrino energies above a few PeV, the Earth becomes opaque to neutrinos since their absorption probability increases with energy [16].

Cosmic rays with energies above 10^{20} eV have been detected [17] and impose the ques-

tion in which cosmic settings particles can be accelerated to such energies. The directions of their trajectories are randomized by galactic and inter-galactic magnetic fields so that their flux is isotropic and individual particles can not be attributed to a specific source. Today, cosmic rays are believed to originate from sources throughout the universe, namely active galactic nuclei and supernovae - the same sources thought to produce cosmic neutrinos.

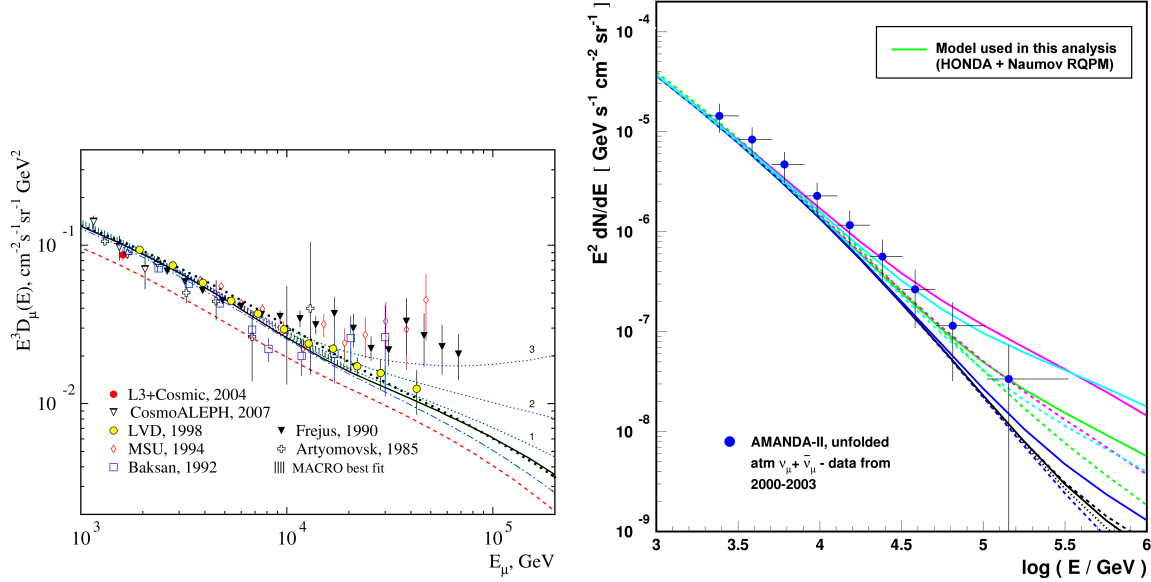


Figure 2.7: Left: Atmospheric muon neutrino spectrum, E_ν^2 -weighted. Circles denote measurements by AMANDA, the predecessor of IceCube. The various lines indicate model spectra, the solid green line represents the model assumed in this analysis [51], [52]. Adapted from [13]. **Right:** Atmospheric muon spectrum at the Earth's surface, E_μ^3 -weighted. Markers indicate measurements, lines represent models. Adapted from [14].

2.6.2 Cosmic Accelerators

Theories for high energy neutrino emission exist for a variety of astrophysical phenomena, specifically core collapse supernovae. These events will be described in detail in chapter 3. Here, two classes of objects shall be discussed, not primarily because of their high prospects as neutrino sources, but rather because they share important features with core collapse supernovae.

2.6.3 Gamma Ray Bursts (GRB)

Gamma ray bursts (for a review, see [21]) show striking similarities with core collapse supernovae. They were first detected in the 1960s as mysterious point-like flashes of electromagnetic radiation in the gamma ray band ($E_\gamma \approx 0.1 - 1$ MeV) [18]. Later systematic searches (e.g. [19]) recorded thousands of these events isotropically distributed across the sky, which suggested an extragalactic origin and extraordinary luminosities. The durations of the bursts showed a bimodal distribution with maxima at ~ 0.2 s and ~ 20 s and to the classification into short (< 2 s) and long (> 2 s) GRBs. Variability time scales of $\sim 10^{-3}$ s constrained source dimensions to ~ 1000 km and hinted at an association of GRBs with stars or black holes. Redshift measurements (e.g. [20]) proved the cosmological origin of GRBs and energy releases

that would - if isotropic - amount to $10^{51} - 10^{54}$ ergs. Theoretical difficulties in explaining this extreme energy release by an Earth-sized source as well as polarization measurements gave rise to the idea that GRBs, have relativistic jets of $5^\circ - 20^\circ$ opening angle. This theory was supported by the fact that collimated emission in jets allowed modelling the distribution of the shapes of GRB light curves. Follow-up observations after the prompt (burst) emission showed an X-ray, optical, infrared, and radio afterglow decaying according to a powerlaw over several months or even years .

GRBs are among the most promising candidates for cosmic neutrino sources. The favored model to explain the broken power law photon spectrum, the relativistic fireball model, inherently predicts neutrino production . Leaving the question what type of central engine powers the GRB open, the model assumes that shells of mass are ejected at relativistic velocities, then slow down and collide with subsequent mass shells (inner shock) creating a shock front which travels outward in the plasma with a velocity $v \sim c$. When a shock front travels through a magnetized plasma, charged particles are accelerated in a process called Fermi acceleration: The charged particle is scattered back and forth within the shock and gains energy in each cycle. Under the assumption that the probability of the particle to escape the shock during each cycle and the energy gain in each cycle are constant, this process results in a powerlaw spectrum $\propto E^{-\gamma}$ with $\gamma \simeq 2$ for the charged particles [24].

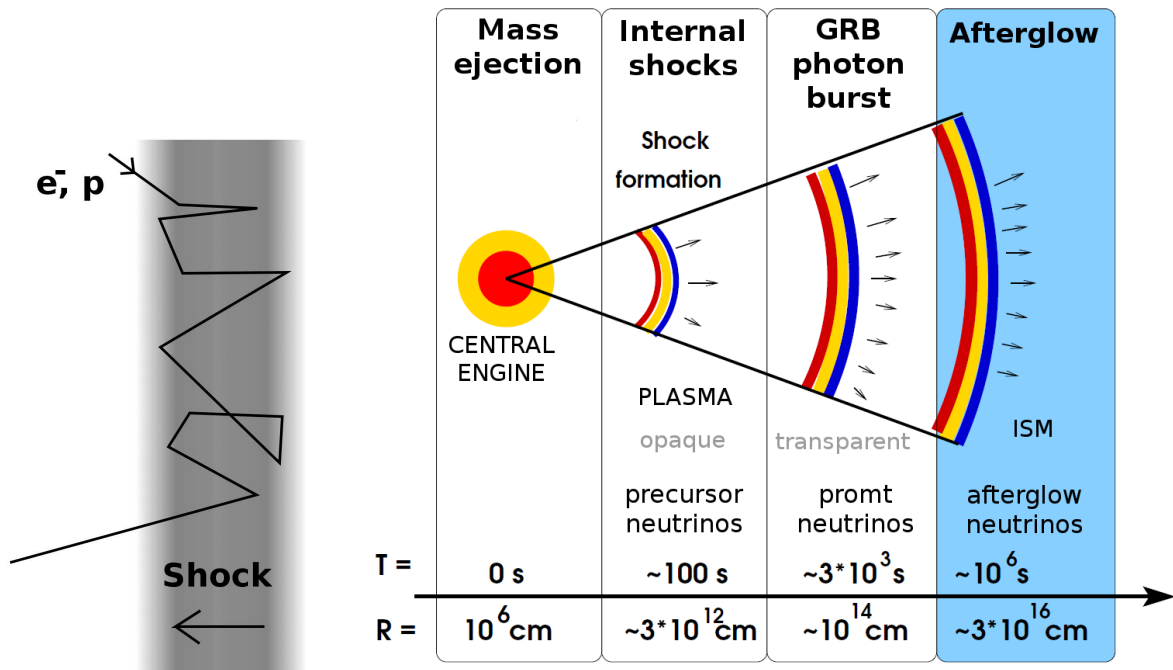


Figure 2.8: **Left:** Illustration of Fermi acceleration: a charged particle is trapped in a shock front and released with an increased energy. **Right:** Schematic view of the fireball scenario. Adapted from [13].

The observed photon spectrum of GRBs can be explained by Fermi acceleration and subsequent synchrotron emission of electrons, if electron cooling is included to account for the spectral break at $E_\gamma \simeq 250$ keV. Though irrelevant for synchrotron emission, the ubiquitous protons are also Fermi accelerated and believed to produce neutrinos in reactions like 2.8 [22], [23]. Theorists distinguish *precursor neutrinos* produced in internal shocks and in a short burst before the GRB, *prompt neutrinos* coincident with the GRB, and *afterglow neutrinos*

produced in external shock, each type possessing a distinct spectrum.

2.6.4 Active Galaxies

While relativistic jets are essential to GRB models they have not been directly observed in association with GRBs and such a detection would require a GRB to occur in our own galaxy. The existence of such jets, was however impressively proven by observations of active galaxies. This short review is based on [26] and

A number of unusual phenomena, historically been named according to their observational properties, are today believed to be associated to active galaxies, namely Seyfert galaxies, radio galaxies, quasars, and blazars. A galaxy is classified active if its central region (nucleus) emits unusually intense and “hot” electromagnetic radiation (especially UV) and has an irregular spectrum, clearly distinct from typical star or galaxy spectra. The first observed active galaxies were believed to be point-like such as stars [25] and consequently named “quasi stellar objects”: Their host galaxies were only discovered years later as a dim haze around these quasars. Steep inner rotation curves, extreme thermal broadening of emission lines, and short variability time scales hinted at the existence of a supermassive black hole in the center of an active galaxy. The existence of a central blackhole of $M \simeq 10^7 - 10^9 M_{\odot}$ has been confirmed for a number of active galaxies through indirect, yet convincing measurements.

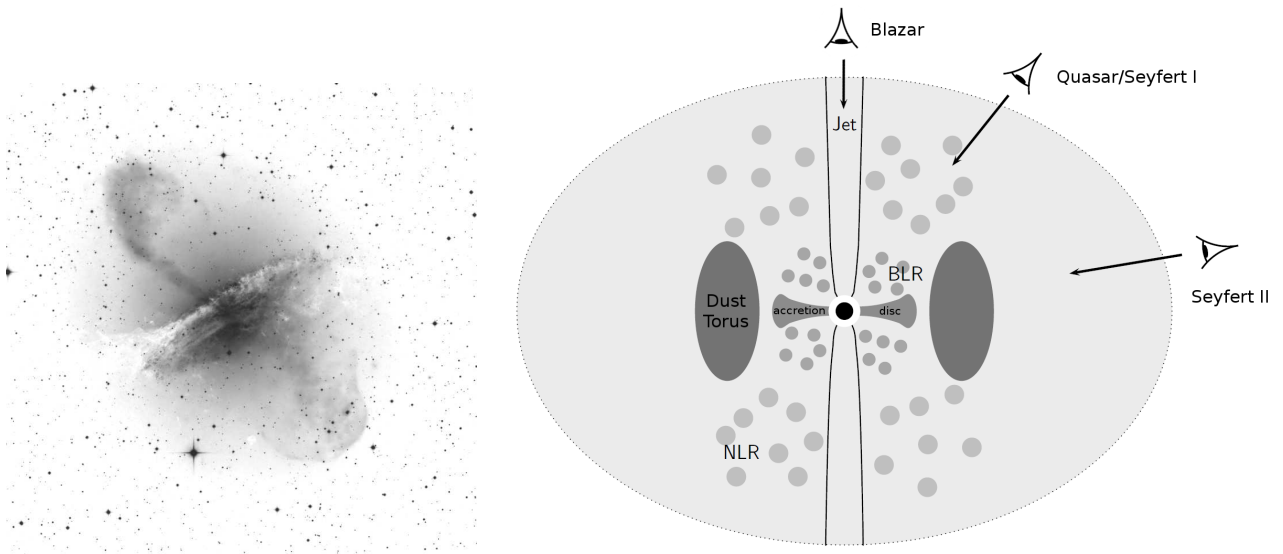


Figure 2.9: **Left:** Optical image of the active galaxy NGC 5128 (Credit: Hubble Space Telescope). **Right:** Schematic illustration of an active galaxy with a central supermassive black hole. Some of the observational categories of active galaxies are indicated with the corresponding viewing angle. Adapted from [26].

Today’s standard model of active galaxies is shown in Fig. 2.9. Due to the complex geometry, the galaxy’s visible signature depends on the inclination angle at which it is observed. The extraordinary luminosity of the central region is generated through mass accretion into the black hole: Hot material in the accretion disc loses gravitational energy and angular momentum through friction, heats up, and falls into the black hole. Potential energy

is radiated away in a continuous high energy spectrum. Surrounding gas maintains a hot equilibrium by absorbing part of this radiation and re-emitting hydrogen lines which are broad in the inner regions (broad line region, BLR) and narrow in the outer region (narrow line region, NLR). In addition, the idea of a dust torus which obscures the inner region for certain viewing angles has been introduced to explain observations of some active galaxies along their galactic plane.

Angular momentum conservation requires the central black hole as well as its accretion disc to rotate at high velocities - regardless of the exact formation process. This rotation powers magnetic fields which drive two jets: relativistic, highly collimated outflows perpendicular to the accretion disc, which shoot hot plasma many kiloparsec into the intergalactic medium. Jets have been observed in several active galaxies and proven to be highly variable on short timescales (days). Single "blobs" of material being shot out in the jet have been recorded.

Neutrino emission from active galaxies is attributed to the Fermi acceleration of protons or bulk acceleration of "blobs" in the highly variable jets [27]. Protons that subsequently collide with photons or other protons would produce neutrinos, while escaping protons would be observed as cosmic rays .

Chapter 3

Supernovae as Neutrino Sources

The term supernova is used for the explosive disruption of a star, visible as an optical flash. For durations ranging from a few days to several weeks, supernovae can exceed the luminosity of an entire galaxy and emit as much energy as the sun produces in its full life span. During the past millenium, six supernovae were observed within our own galaxy, most recently SN 1987A, which was visible to the naked eye. It is estimated that in the entire universe supernovae occur with a frequency of one per second. Supernovae are of enormous scientific interest in a variety of areas: They play a crucial role in understanding the chemical composition and evolution of the universe, galaxy evolution, the origin of cosmic rays, the formation of black holes, and in measuring cosmological parameters. Representing gigantic particle accelerators as well as fusion reactors, supernovae harbor conditions similar to those in the early universe and provide an opportunity to study the behavior of matter at extremely high densities, temperatures, and energies. Traditionally, supernovae have been observed in the optical and ultra-violet part of the electromagnetic spectrum. In the past 50 years, radio, infrared, X-ray, and gamma ray measurements have been included in the study of supernovae. In one case, that of SN 1987A, low energy neutrinos ($E_\nu \sim \text{MeV}$) have been detected. Since detectors for electromagnetic radiation cannot provide full-time and full-sky coverage, discovering supernova always requires luck. Moreover, in the electromagnetic spectrum, the extremely dense inner regions of a supernova are obscured.

High energy neutrinos, if emitted by supernovae as predicted, could open a new window to the study of the physics of these explosions. Neutrino telescopes like IceCube can monitor large portions of the sky and take data more than 90% of the time. They can contribute to supernova searches and analyses in two ways: First, IceCube data can be scanned real-time for nearly collinear neutrino multiplets and trigger optical follow-up searches for supernovae at the respective coordinates. This technique has already been implemented and might lead to the first early supernova detections in the near future [57]. Second, if electromagnetic observations provide precise timing information, IceCube data can be searched for neutrinos from the corresponding direction by hindsight. Such analyses have the advantage of being fine-tuned to the observed properties of a supernova and extracting signal at a significance level that would leave no doubts about its cosmic origin. Since this analysis takes the latter approach, examining a single, known supernova, the best possible knowledge of its properties is crucial. This section therefore outlines the properties of supernovae in general and core collapse supernovae specifically and presents evidence for a connection between core collapse supernovae and long duration γ -ray bursts. Finally, a model for neutrino emission by core-collapse supernovae is discussed and adapted to SN 2008D.

3.1 Supernovae: Properties and Terminology

Supernovae are classified by their observed spectral properties, rather than by theoretical criteria. The classification type I/II is based on the absence/presence of hydrogen absorption lines in the supernova spectrum. Type Ia have a strong absorption line of singly ionized silicon (Si II) while type Ib, Ic lack this feature.

Nevertheless, a clear distinction between type Ia and type Ib, Ic, II can be made based on the physical mechanism leading to the explosion. The following descriptions are based on [5] and [28] and inevitably gloss over some theoretical disaccord especially about the physics of core collapse supernovae.

3.1.1 Type Ia

Type Ia supernovae are a rather rare type, approximately 100 times less frequent than Type Ib, Ic, II, characterized by the absence of hydrogen lines in their spectra. Their rarity is owed to the underlying mechanism requiring rather singular conditions:

Stars with masses less than $\sim M_{\odot}$ (M_{\odot} - mass of the sun) die a peaceful death: Once the fuel for the nuclear fusion sustaining their hydrostatic equilibrium is exhausted, they blow off their stellar envelope and the bare core remains and cools into obscurity. These end products of low mass stellar evolutions are called white dwarfs and have masses $< 1.4 M_{\odot}$ condensed into a sphere of the size of the Earth. Electron degeneracy pressure - no more than two electrons can occupy an elementary phase space volume of h^3 - prevents their gravitational collapse. If a white dwarf, however, exceeds a mass of $1.4 M_{\odot}$, the *Chandrasekhar mass*, electrons become relativistic and their equation of state abruptly changes, facilitating further compression. The most commonly assumed scenario explaining the necessary mass transfer are close binary systems in which one star is a white dwarf accreting mass from its stellar companion. Once the star passes the Chandrasekhar limit, compression sets in and quickly creates densities and temperatures high enough to allow runaway energy release by carbon and oxygen fusion: A thermonuclear explosion disrupts the entire star leaving nothing behind but a cloud of debris (and possibly the stellar companion).

Due to their almost universal mass and luminosity, type Ia supernovae are used as standard candles for cosmological distance measurements. They can easily be identified by their characteristic light curve, the absence of hydrogen features in the spectrum, and a strong Si II absorption line.

3.1.2 Type Ib,Ic,II

Type Ib,Ic,II are collectively named core-collapse supernovae. They occur in stars with masses greater than $\sim 8 M_{\odot}$, when the stellar core exceeds the Chandrasekhar mass and collapses. In contrast to accreting white dwarfs, the cores of massive stars consist mainly of heavy elements like iron, for which exothermic nuclear fusion to heavier elements is not possible. Therefore, the core-collapse proceeds and rising temperatures only lead to the photodisintegration of iron and neutron production via electron capture by protons and nuclei:



Combined, these reactions enrich the core with neutron-rich nuclei and significantly reduce the electron density and electron degeneracy pressure, further facilitating the collapse.

Eventually, when the core reaches about twice the density of an atomic nucleus, it becomes quasi incompressible, and the collapse “recoils” blocked by repulsive nuclear forces. This recoil propagates as a sound wave into the infalling mantle material and condenses into a shock front that travels outward and reverses the implosion of the mantle. There is still significant uncertainty about the process that allows the shock front to transform into bulk motion and power the ejection of the mantle. In computer simulations the shock front tends to stall at radii of only ~ 100 km.

As observational data shows, however, the shock does break out of the stellar envelope and deposits its energy in the very thin outer layers. Following shock break out, the mantle is driven outward into the interstellar medium forming a bubble of several parsec diameter. The ejected mantle emits the long-lived (\sim days - months) optical signature of the supernova which is powered by decays of radioactive isotopes produced in the explosion (mainly ^{56}Ni). In its center, a dense, fast spinning neutron star remains observable as a radio pulsar. For stars more massive than $\sim 20 M_{\odot}$, the core collapses into a black hole instead of a neutron star.

Type Ib, Ic are believed to occur when the stellar progenitor has already stripped its outer hydrogen (helium) shell through stellar winds before the core-collapse. Such stars are called Wolf-Rayet stars. In type II supernovae, the hydrogen shell is still intact when the core explodes and the spectrum of the optical afterglow exhibits Balmer absorption lines.

3.2 Supernova Neutrinos

To avoid confusion, the different types of “supernova neutrinos” and their production mechanisms shall be presented briefly:

3.2.1 Low Energy

Low energy supernova neutrinos have energies of \sim MeV and originate from two processes, electron capture (Eq. 2.2) by protons in the extreme environment of the core during collapse and neutrino and pair production ($e^+e^- \leftrightarrow \nu\bar{\nu}$, Fig. 2.3) in the cooling core after the explosion. The former process, also called *neutronization* produces a short ~ 10 s burst of $\sim 10^{57}$ neutrinos with $E_{\nu} \sim 10$ MeV i.e. a total of $\sim 10^{53}$ erg. The latter gives rise to a more long lived emission of *thermal* neutrinos. The emission of low energy neutrinos by core-collapse supernovae has been directly observed for SN 1987A, a galactic type II supernova at only 50 kpc. A burst of 24 neutrinos within 12 s was observed by three water-Cherenkov detectors in close coincidence with the optical flash and marked the beginning of extrasolar neutrino astronomy [5]. Low energy neutrinos can be detected in IceCube as an transient and collective increase in the hit rates of all sensors [29]. They shall, however, not be discussed any further and the term “neutrino” shall stand for high energy neutrinos in the following.

3.2.2 High Energy

Neutrinos with energies of energies $E_{\nu} > 1$ GeV, are further subdivided into very high energy (VHE) neutrinos with $E_{\nu} > 50$ GeV, ultra high energy (UHE) neutrinos with $E_{\nu} > 10^3$ GeV and extremely high energy (EHE) neutrinos with $E_{\nu} > 10^{10}$ GeV. Their production requires either the annihilation of equally energetic (or very massive) particles or collisions of highly

accelerated particles. In the following, possible production mechanisms shall be narrowed down to:

$$\text{proton acceleration} \rightarrow pp, p\gamma \text{ collisions} \rightarrow \text{charged mesons} \rightarrow \text{neutrinos} \quad (3.4)$$

The AMANDA and IceCube detectors have detected high energy neutrinos copiously with energies up to $E_\nu > 100 \text{ TeV}$ (energy reconstructions for muon neutrinos from their secondary muon can only provide a lower bound). Their spectrum was, however, consistent with expectations for atmospheric neutrinos. In other words, high energy neutrinos *have* been observed, but no neutrinos from cosmic sources have been detected thus far. This includes supernovae for which high energy neutrino emission seems plausible, yet remains speculative.

3.3 Supernova-Gamma Ray Burst Connection

Observations in recent years have given rise to the idea that core collapse supernovae and long duration γ -ray bursts have a common origin or may even be two different aspects of the same physical phenomenon, the death of a massive star (see e.g. [31]). Moreover, observed associations of supernovae with XRFs, short X-ray flashes with similar characteristics as long GRB, suggest to include XRF in the SN-GRB connection. XRF are considered a separate observational category from GRB, however a common origin and a continuous sequence connecting them have been suggested [32] [33] and are commonly assumed. X-ray flashes could be long GRBs with very weak jets or simply long GRBs observed at a different angle [31].

A total of six long duration, weak, and soft-spectrum γ -ray bursts (or X-ray flashes) have been observed in coincidence with a core collapse supernova thus far: SN 1998bw [34], SN 2003lw [36], SN 2003dh [35], SN 2006aj [37], SN 2007gr [38], and SN 2008D [39]. In addition, recent radio observations of SN 2007gr provide strong evidence that this core collapse supernova possesses mildly relativistic jets with $\Gamma \sim 1.25$ [38].

In a unified model, the core collapse at the death of a massive star might lead to an "ordinary" core collapse supernova if the energy release is completely spherical and to an X-ray flash or long γ -ray burst followed by a supernova if a mildly relativistic jet ($\Gamma \sim 1 - 10$) is formed. Short bursts with their highly relativistic jets $\Gamma \sim 100 - 1000$ could be accommodated if the observed ratio of short γ -ray bursts to core collapse supernovae (roughly 1:1000 [30]) coincided with the small fraction of core collapses with fast rotating progenitors. To the observer, this simple scenario would, however, be confused by the fact that associated γ -ray bursts are rarely observable since the jet axis must be somewhat aligned with the optical axis. Moreover, because of the relative rarity of γ -ray bursts with respect to supernovae, they are generally observed at much larger distances $\gtrsim 100 \text{ Mpc}$ where dim afterglows are difficult to observe.

In the unified model, core-collapse supernovae form a continuous sequence of kinetic energy release $E_K \simeq 10^{51} - 10^{53} \text{ erg}$ and jet Lorentz factors $\Gamma_j \simeq 1 - 1000$. An associated γ -ray burst is only observable if the jet is sufficiently powerful to break out of the core and optically thin so that γ photons can escape. In less energetic core collapse supernovae, the jets may not be able to break through the stellar envelope at all. For this hypothetical scenario the term *choked* or *hidden* jet is used and neither gamma radiation nor the electromagnetic signature of the jet should be detectable: An observer would see an "ordinary" core collapse supernova, possibly accompanied by an X-ray flash.

Feature	core collapse SN	long GRB
X-ray flash	yes	yes
Explosion Asymmetry	yes	yes
Jets	evidence	yes
Optical Afterglow	yes	yes
Radio Afterglow	yes	yes
Expansion velocity > 10,000 km/s	yes	yes

Table 3.1: Observations favoring a common origin of core collapse SNe and long GRBs.

The detection of high energy neutrinos could directly and convincingly show the presence of jets, even of choked jets. The emission of high energy neutrinos is expected for core collapse supernovae with mildly relativistic jets based on similar considerations as described in section 2.6.3 for γ -ray bursts. A model adapted to core collapse supernovae is presented in Sec. 3.5.

3.4 Supernova 2008D

On a lucky day for astronomy, January 9, 2008, the X-ray telescope aboard the SWIFT¹ satellite recorded a bright X-ray flash in the galaxy NGC 2770 during a routine observation of previous supernovae in the same galaxy. Extensive optical, infrared, and radio follow-up observations were triggered unusually early and confirmed that the X-ray flare was associated with a type Ib/c supernova: SN 2008D [39]. The SWIFT data is the first direct observation of the shock break out emission from a core collapse supernova. Due to the lack of hydrogen features and the presence of the Si II line in its spectrum, SN 2008D was classified as a type Ib/c. (The Asiago Supernova Catalogue lists SN 2008D as type Ib because of the presence of helium features. The distinction is irrelevant for the purposes of this analysis.) Some observed properties of SN 2008D which will be referred to in the following chapters are listed in Table 3.4.

The possible supernova - γ -ray burst connection described in Sec. 3.3 motivates a search for high energy neutrinos emitted by SN 2008D. The existence of mildly relativistic jets and an energy release comparable to that of a γ -ray burst have been suggested based on the observational properties of SN 2008D [45]. A quantitative model for this scenario exists and shall be discussed in the following section.

¹www.nasa.gov/mission_pages/swift/main/

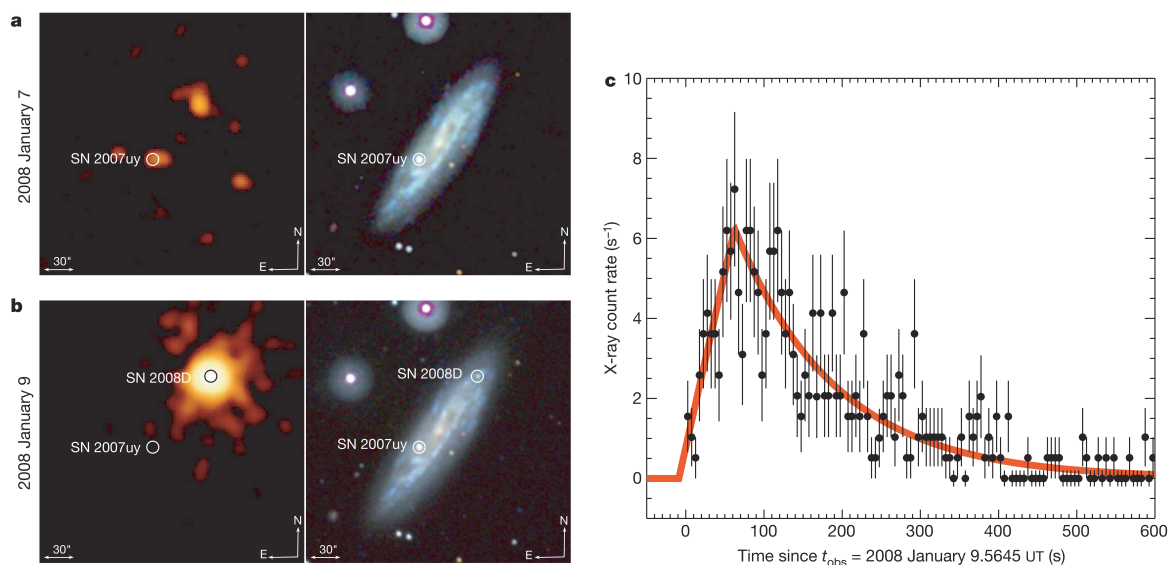


Figure 3.1: Left: X-ray (left) and optical (right) images of NGC 2770 taken before (top) and during (bottom) the X-ray flash. Right: X-ray lightcurve of SN 2008D measured by SWIFT. Both figures were taken from [39].

Parameter	Value
Type	Ib/c
Apparent V-Band Magnitude	17.5
Distance	27 Mpc
Time of shock break-out	Jan 9, 13:32:40 UT 54474.56435 MJD
Timing uncertainty (90% CL)	+20 – 9 s
RA (J2000)	09h 09min 31s
DEC (J2000)	+33° 08' 20"
Zenith	123.14°
Azimuth	264.26°

Table 3.2: Observed properties of SN2008D from [39] and [40]. The zenith and azimuth coordinates are given in the IceCube coordinate system (see Sec 4.5.2) for the quoted shock breakout time.

3.5 Slow Jet Model

A model for the emission of high energy neutrinos by core collapse supernovae has been proposed by Waxman and Loeb [41], refined by Razzaque, Meszaros, and Waxman [42] and further elaborated by Ando and Beacom [43]. The end result, published in [43] shall be called “slow jet model” in the following. A brief summary of its physical motivation and a derivation of its analytical form shall be presented using the notation of [43].

3.5.1 Phenomenology

The slow jet model builds on the fireball model for γ -ray bursts and requires the collapse of a massive star $M_{\text{star}} \gtrsim 8 M_{\odot}$ with subsequent formation of a neutron star or black hole, rotating sufficiently to power jets with bulk Lorentz factors of $\Gamma_b \sim 1 - 10$ and opening angles $\theta_j \approx 1/\Gamma = 5^\circ - 50^\circ$. The rebounding core collapse is assumed to deposit $E_j \sim 10^{51}$ erg in the kinetic energy of the material ejected in the jets². A fraction of $\epsilon_e \sim 0.1$ of the bulk kinetic energy is converted into random electron motion through Fermi acceleration, and a fraction $\epsilon_B \sim 0.1$ is bound in magnetic fields. In the slow jet model, synchrotron radiation emitted by electrons and positrons cannot escape because of the optical density in the jet. Synchrotron photons thermalize instead so that no γ -radiation i.e. no typical γ -ray burst can be observed. Instead, a comptonized component of the thermal emission might be detectable as an X-ray flash.

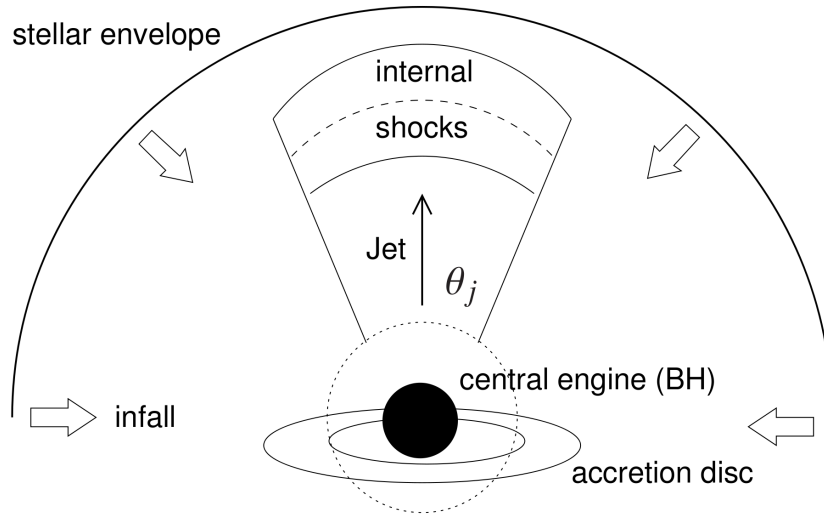


Figure 3.2: Cartoon of a mildly relativistic jet buried inside the envelope of a collapsing star. A black hole is assumed as the central engine. The jet may deposit its kinetic energy and help blow up the envelope but may not get out itself. From [42].

Protons are also Fermi accelerated by the Fermi mechanism to a E_p^{-2} spectrum normalized to the total kinetic energy of the jet E_j . The proton spectrum has a cutoff at a maximum energy of $E_{p,max}$ at which protons immediately lose any energy gained in Fermi acceleration through photopion production $p\gamma \rightarrow \Delta^+ \rightarrow n\pi^+$. In consequence, protons are blocked from higher energies, where the photopion cross section decreases again. Thus, in contrast

²Values of up to $E_j = 6 \times 10^{51}$ erg have been suggested for SN 2008D [45].

to common γ -ray burst models where $p\gamma$ collisions represent the main process for neutrino production, core collapse supernova are expected to produce neutrinos mainly in pp collisions. Below the maximum energy, protons efficiently produce charged pions and kaons in through $pp \rightarrow \dots \pi^\pm / K^\pm$.

As discussed in section 2.4.2, charged mesons decay into neutrinos via: $\pi^\pm / K^\pm \rightarrow \mu^\pm \nu_\mu (\bar{\nu}_\mu)$. At the relevant energies, decays of secondary muons (e.g. $\mu^- \rightarrow e^- \bar{\nu}_e \nu_\mu$) do not contribute high energy neutrinos because muons immediately lose most of their energy through inverse Compton scattering and synchrotron radiation (radiative cooling).

The produced mesons follow the primary E^{-2} proton spectrum with $\sim 20\%$ of the proton energy for each pion or kaon. The resulting neutrino spectrum, however does not follow the pion/kaon spectrum at *production*, but rather at *decay*, i.e. one pion/kaon lifetime later. Before decaying, mesons lose energy. While this energy loss is negligible at low meson energies $\lesssim 10$ GeV, it significantly reduces the number of high energy ($> \text{TeV}$) mesons which decay into neutrinos. The dominant processes for meson cooling are hadronic (elastic πp and $K p$ scattering) and electromagnetic (inverse Compton scattering and synchrotron emission) reactions. To obtain the break energies above which each cooling process becomes relevant, the corresponding energy-dependent cooling timescale is equated with the proper lifetime of the charged pion/kaon.

Above a first break energy, more than one hadronic cooling interaction takes place during a pion/kaon lifetime. This shifts pions/kaons to lower energies and causes a steepening of the neutrino spectrum $\propto E^{-1}$. At the second break energy, radiative cooling becomes significant and causes another steepening of E^{-1} in the neutrino spectrum which finally breaks off at $E_{v,max} = 0.2 \Gamma_b E_{p,max} / 4$ corresponding to the maximum proton energy. (The factor Γ_b transforms from the comoving frame in the jet into the observer's rest frame.)

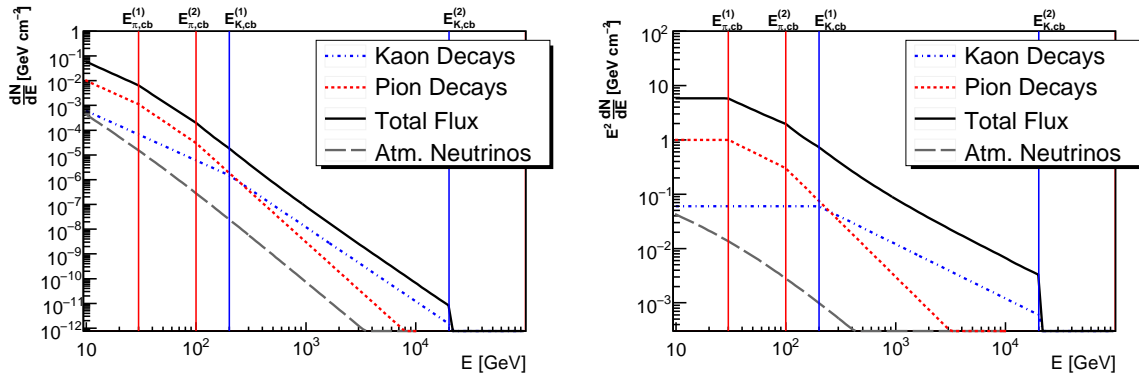


Figure 3.3: Muon neutrino (both ν_μ and $\bar{\nu}_\mu$) spectrum of SN 2008D according to the slow jet model. Both plots show the same spectrum, however, the right plot is scaled with E^2 , a common scaling for neutrino spectra. Contributions from pion and kaon decays are marked by the dotted lines. The break energies (top axis) indicate where electromagnetic/hadronic cooling set in and suppress the neutrino spectrum. The dashed line represents the atmospheric neutrino spectrum from a 10° circle around the position of SN 2008D and for a 100 s measurement.

Since kaons have a much higher mass ($m_{\pi^\pm} = 139.57 \text{ MeV}$, $m_{K^\pm} = 493.78 \text{ MeV}$) and shorter lifetime than pions ($\tau_{K^\pm} = 1.24 \times 10^{-8} \text{ s}$, $\tau_{\pi^\pm} = 2.60 \times 10^{-8} \text{ s}$), they have much less time to cool and hadronic cooling ($\propto m^4$) is much slower. Therefore the cooling breaks occur

at different energies in the spectra of neutrinos from kaon and pion decay and kaons yield the main contribution to the total neutrino spectrum at high energies. This effect is slightly reduced by the fact that nearly all π^\pm decay into μ^\pm while this is only the case for 63% of all K^\pm . Ando and Beacom estimate that neutrinos are produced with 50% of the pion/kaon energy.

Neutrinos are expected to be emitted in alignment with the jets since shocks travel along the jet and accelerate protons in the direction of their propagation. Secondary mesons and neutrinos are nearly collinear with the primary protons since $p_p \approx p_{\text{CMS}}$ holds for the proton and center of mass four momenta in the relevant energy regime. The energy range of the neutrinos is set by the jet opening angle and by the maximum proton energy and reaches far into the sensitive range of the IceCube detector ($E_\nu \gtrsim 10 \text{ GeV}$).

3.5.2 Analytical Form

With the considerations from the previous section, an analytical expression for the $\nu_\mu + \bar{\nu}_\mu$ -spectrum of a slow jet supernova can be written down in a straight forward manner. First, the primary neutrino spectrum, normalized to the kinetic energy release, is given by:

$$\frac{dN_p}{dE_p}(E_p) = \frac{E_j}{\ln(E_{p,max}/E_{p,min})} E_p^{-2} \quad (3.5)$$

From the primary proton spectrum the secondary neutrino spectrum is calculated as follows:

$$\frac{dN_\nu}{dE_\nu}(E_\nu) = \sum_{i=\pi,K} \frac{dN_p}{dE_p}(E_p(E_\nu)) \times \frac{dE_p}{dE_i} \frac{dE_i}{dE_\nu} \frac{dN_\nu}{dN_i} \frac{dN_i}{dN_p} \times f_{\text{cool},i}(E_\nu) \quad (3.6)$$

With the estimate $E_\nu = \frac{\Gamma_b E_{\pi/K}}{2} = \frac{\Gamma_b E_p}{8}$, the factors $\frac{dE_p}{dE_i}$ and $\frac{dE_i}{dE_\nu}$ are easily calculated, while $\frac{dN_\nu}{dN_i}$ and $\frac{dN_i}{dN_p}$ are well known ratios:

$\frac{dE_i}{dE_p} = \frac{1}{4}$	fraction of proton energy going into each charged pion/kaon
$\frac{dE_\nu}{dE_i} = \frac{1}{2}$	fraction of pion/kaon energy going into each neutrino
$\frac{dN_\nu}{dN_\pi} = B_\pi$ $\frac{dN_\nu}{dN_K} = B_K$	number of neutrinos produced by each charged pion/kaon, branching ratio for $\pi^\pm/K^\pm \rightarrow \mu^\pm \nu_\mu (\bar{\nu}_\mu)$
$\frac{dN_\pi}{dN_p} = \langle n \rangle_\pi$ $\frac{dN_K}{dN_p} = \langle n \rangle_K$	number of charged pions/kaons produced by each proton (pion/kaon multiplicity)

The last term describes the energy dependent suppression of neutrino production due to meson cooling before decay:

$$f_{\text{cool},i}(E_\nu) = \begin{cases} 1 & E_\nu < E_{i,cb}^{(1)} \\ E_\nu^{-1} E_{i,cb}^{(1)} & E_{i,cb}^{(1)} \leq E_\nu < E_{i,cb}^{(2)} \\ E_\nu^{-2} E_{i,cb}^{(1)} E_{i,cb}^{(2)} & E_{i,cb}^{(2)} \leq E_\nu \leq E_{\nu,max} \end{cases} \quad (3.7)$$

Finally the neutrino number flux is spread over the area $A = 2\pi\theta_j^2 d^2$ of the two jet caps at the distance d of the Earth to obtain a flux in units of $\text{GeV}^{-1} \text{cm}^{-2}$. The flux $\Phi_\nu(E_\nu)$ can be written in compact form as follows:

$$\Phi_\nu(E_\nu) = \sum_{i=\pi,K} \Phi_\nu^{(i)} = \sum_{i=\pi,K} \eta_i \cdot \begin{cases} E_\nu^{-2} & E_{p,min} \leq E_\nu < E_{i,cb}^{(1)} \\ E_\nu^{-3} E_{i,cb}^{(1)} & E_{i,cb}^{(1)} \leq E_\nu < E_{i,cb}^{(2)} \\ E_\nu^{-4} E_{i,cb}^{(1)} E_{i,cb}^{(2)} & E_{i,cb}^{(2)} \leq E_\nu \leq E_{\nu,max} \end{cases} \quad (3.8)$$

$$\eta_i = \frac{\langle n \rangle_i B_i E_j}{8 (2\pi \theta_j^2 d^2) \ln(E_{p,max}/E_{p,min})}$$

Figure 3.4: Analytical form of the slow jet model; descriptions and values of the parameters are given in table 3.5.2.

Parameter	Description	Value
E_j	Kinetic energy of the jet	3×10^{51} erg
Γ_b	Bulk Lorentz factor of the jet	3
$\theta_j \simeq \Gamma_b^{-1}$	Opening angle of the jet, measured with respect to the symmetric axis, the angular diameter is $2\theta_j$	0.33 rad (17°)
d	Luminosity distance of SN 2008D	27 Mpc
$E_{p,max}$	Maximum proton energy	7×10^4 GeV
$E_{p,min}$	Minimum proton energy (can be set arbitrarily low)	10 GeV
$E_{\nu,max}$	Maximum neutrino energy	2.1×10^4 GeV
$B_\pi (B_K)$	Branching ratio for $\pi^\pm \rightarrow \mu^\pm \nu_\mu (\bar{\nu}_\mu)$ ($K^\pm \rightarrow \mu^\pm \nu_\mu (\bar{\nu}_\mu)$)	1 (0.63)
$\langle n \rangle_\pi$ ($\langle n \rangle_K$)	Pion (kaon) multiplicity	1 (0.1)
$E_{\pi,cb}^{(1)}$ ($E_{K,cb}^{(1)}$)	first cooling break energy for pions (kaons)	30 GeV (200 GeV)
$E_{\pi,cb}^{(2)}$ ($E_{K,cb}^{(2)}$)	second cooling break energy for pions (kaons)	100 GeV (20.000 GeV)

Table 3.3: Estimated parameters used to predict the muon neutrino spectrum of SN 2008D in the slow jet model. From [43] with the exception of the distance d [39].

In order to detect these neutrinos, the jet must be pointing towards Earth (5% chance for a jet with an opening angle of 17° , i.e. 34° diameter). Due to the unknown pointing, however, no constraints can be placed on the model in the case of a non-detection. To do so with a confidence level of e.g. 90% would require a large sample of ~ 200 nearby supernovae. In contrast, a significant detection would not only indicate the jet's direction, but also yield constraints on the slow jet model. Constraints entirely independent of observations in the electromagnetic spectrum. If, in addition, a resolved neutrino spectrum could be recorded with future neutrino detectors, the features of the slow jet model would place strong constraints on the physical parameters of the supernova jet given the sensitive parameter dependencies listed in Table 3.5.2.

Feature	Description	Dependence
$E_{\nu,max}$	Maximum neutrino energy	$\propto \Gamma$
$E_{\pi,cb}^{(1)}$	first break energy	$\propto E_j^{-1} \Gamma_b^7 \theta_j^2 t_j^2 t_v^2$
$E_{\pi,cb}^{(2)}$	second break energy	$\propto (\epsilon_e + \epsilon_B)^{-1} \Gamma_b$
$E_{K,cb}^{(1)}$	third break energy	$\propto E_j^{-1} \Gamma_b^7 \theta_j^2 t_j^2 t_v^2$
$E_{K,cb}^{(2)}$	fourth break energy	$\propto (\epsilon_e + \epsilon_B)^{-1} \Gamma_b$

Table 3.4: Parameter dependencies of the features of the slow jet spectrum, from [43].

Chapter 4

Neutrino Detection

There is no indication for the existence of neutrinos in everyday life - we cannot see them. In fact, most sensitive microelectronics have to be combined with hundreds of tons of water or ice into gigantic detectors, the size of a football stadium, to catch a few of the billions of neutrinos passing through the Earth each second. This section shall outline the principles of neutrino detection and their practical application in the IceCube detector.

4.1 Neutrino Propagation

Neutrinos produced in cosmic sources, e.g. the center of a distant galaxy, are unaffected by magnetic fields and hardly absorbed by intergalactic matter. Therefore, they point back to their source and should soon allow mapping the high energy sky in neutrinos. Before neutrino detection techniques are discussed, two effects affecting the neutrino signal on its way from the source to the detector shall be mentioned.

4.1.1 Flavor Oscillations

The lack of solar electron neutrinos first observed by the Homestake experiment and by other later experiments, gave rise to the theory of neutrino oscillations (mixing). Today an overwhelming amount of evidence exists in favor of neutrino mixing from atmospheric, solar, and accelerator neutrino experiments (see e.g. [9, Ch. 13], [5]). According to this theory, neutrinos of different flavor cannot be regarded as isolated, static particles. Rather, the neutrino constitutes a system of three flavor eigenstates $|\nu_\alpha\rangle \in \{e, \mu, \tau\}$ and three mass eigenstates $|\nu_i\rangle \in \{1, 2, 3\}$ periodically transitioning from one to state to another. Consequently, a neutrino produced with flavor x can be detected with a different flavor y and if a neutrino's mass is measured, its flavor is undefined. For neutrinos, oscillations into another state depend not only on time, but also on their energy and the medium in which they propagate. When participating in a weak interaction (production, detection) neutrinos fall into a defined flavor eigenstate. When propagating freely, however, a neutrino must be described as a superposition of different flavor or mass eigenstates. Neutrino mixing is described by a unitary 3×3 matrix U :

$$|\nu_\alpha\rangle = \sum_i U_{\alpha i}^* |\nu_i\rangle \quad (4.1)$$

$$U = \begin{pmatrix} 1 & 0 & 0 \\ 0 & c_{23} & s_{23} \\ 0 & -s_{23} & c_{23} \end{pmatrix} \begin{pmatrix} c_{13} & 0 & s_{13}e^{-i\delta} \\ 0 & 1 & 0 \\ -s_{13}e^{i\delta} & 0 & c_{13} \end{pmatrix} \begin{pmatrix} c_{12} & s_{12} & 0 \\ -s_{12} & c_{12} & 0 \\ 0 & 0 & 1 \end{pmatrix} \quad (4.2)$$

The matrix is parametrized by one phase δ three mixing angles θ_{ij} ($c_{ij} = \cos \theta_{ij}$ and $s_{ij} = \sin \theta_{ij}$ with $i = 1, 2$ and $j = 1, 2, 3$). Including the vacuum time evolution (propagation) of the mass eigenstates with their energy E_i , an arbitrary neutrino state at time t after production at $t_0 = 0$ can be written as:

$$|\nu_\alpha(t)\rangle = \sum_i U_{\alpha i}^* \exp[-i H_i t] |\nu_i(0)\rangle \quad (4.3)$$

$$\text{or: } |\nu_\alpha(L; E)\rangle = \sum_i U_{\alpha i}^* \exp[-im_i^2 L/2E] |\nu_i(0)\rangle \quad (4.4)$$

Where in the second line, the ultrarelativistic approximation $E_i \approx E + \frac{m_i^2}{2E}$ was used and time was replaced with the distance L since neutrinos move with $\gamma > 10^6$ and $E \gg m_i$ holds. E denotes the total neutrino energy, m_i the mass of the i -th mass eigenstate. This enables us to write down the probability for a neutrino produced as ν_α to be detected as ν_β at a distance L :

$$P_{\nu_\alpha \rightarrow \nu_\beta} = \left| \langle \nu_\beta(t) | \nu_\alpha(0) \rangle \right|^2 \quad (4.5)$$

$$= \delta_{\alpha\beta} - 4 \sum_{j>i} U_{\alpha i} U_{\beta i} U_{\alpha j} U_{\beta j} \sin^2(1.27 \Delta m_{ij}^2 (L/E)) \quad (4.6)$$

Where $\Delta m_{ij}^2 = m_i^2 - m_j^2$ measured in eV^2 , L in km, and E in GeV. To apply this result to the muon neutrino signal from SN 2008D predicted by the slow jet model, we consider the oscillation length L_{ij} :

$$\frac{L_{ij}}{\text{km}} = 2.47 \left(\frac{E_\nu}{\text{GeV}} \right) \left(\frac{\Delta m_{ij}^2}{\text{eV}^2} \right)^{-1} \quad (4.7)$$

For $E_\nu = 1 \text{ TeV}$ and the smallest measured $\Delta m^2 \sim 10^{-5}$, the oscillation length is of order 10^8 km much larger than the upper bound for the neutrino production region given by the radius of a supernova progenitor $R \sim 10^6 \text{ km}$. Therefore, the \sin^2 term in Eq. 4.6 cannot be averaged to 0.5 over the source and the probability of losing initial muon neutrinos to undetectable electron or tau neutrinos depends sensitively on the distance of SN 2008D. This distance ($d = 27 \text{ Mpc}$), however, has an error $\Delta d \sim 1 \text{ Mpc} = 3 \times 10^{19} \text{ km}$. In conclusion, the estimate:

$$r_{\text{source}} \ll L_{ij} \ll \Delta d \quad (4.8)$$

rules out the possibility of calculating in which composition the initial $(\nu_e : \nu_\mu : \nu_\tau) = (0 : 1 : 0)$ signal arrives in the detector.

Because of the energy dependence of the oscillation probability parts of the predicted spectrum might be damped, others enhanced by flavor oscillations. Again, this effect cannot be quantified due unknown distance relations and the absence of a precise energy reconstruction for muon neutrinos.

4.1.2 Time Delay

Because of their non vanishing mass, neutrinos travel slightly slower than photons. An assumed neutrino with $E_\nu = 1$ TeV and a mass of $m = 10$ MeV travels at:

$$v = c \sqrt{1 - \frac{m^2}{E^2}} = \sqrt{1 - 10^{-10}} c \quad (4.9)$$

For a distance of $27 \text{ Mpc} = 3 \times 10^{19} \text{ m}$, this causes a delay with respect to photons of:

$$\Delta t = L/c - L/v \approx 30 \text{ s} \quad (4.10)$$

Even under extreme assumptions for the neutrino mass, the time delay with respect to an optical trigger (X-ray flash in the case of SN 2008D) is contained in the time windows used in this search. The same is true for delays predicted by theories of Lorentz invariance violation, which have smaller values at these distances [59]. Timing will be discussed in greater detail in Sec. 5.6.1.

4.2 Neutrino Interactions

The difficulty in detecting neutrinos is owed to the minuscule cross section of neutrino-nucleon interactions, $\sim 10^{-37} \text{ cm}^2$ at $E_\nu \sim 100 \text{ GeV}$ [5]. Because the cross section for neutrino-electron interactions is even smaller at most energies¹, only neutrino-nucleon interactions are suitable for detecting astrophysical fluxes.

Neutrino-nucleon interactions can be divided into charged-current (CC) and neutral-current (NC) events. In both cases, a fraction of the neutrino energy is liberated at the vertex.

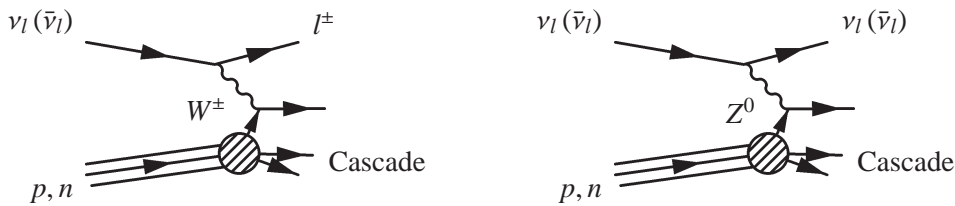
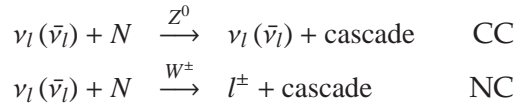


Figure 4.1: Neutrino-nucleon scattering through charged (left) and neutral (right) current.

For neutral-current events, this local energy release is the only detectable signature since the neutrino continues to exist and leaves no trace after the interaction. In the case of charged-current interactions of electron or tau neutrinos, the produced leptons lose all of their energy in the vicinity of the vertex and the tauon subsequently decays in a second vertex. The signature of these events is a spherical, slightly elongated light emission, and possibly a second vertex for tau neutrinos of sufficiently high energy (double bang signature).

¹With the exception of the *Glashow resonance* in Fig. 4.2.

While IceCube is sensitive to these events and analyses promise to detect the first ultrarelativistic electron and tau neutrinos soon (see e.g. [60]), they were not included in this analysis even though electron and tau neutrinos from SN 2008D are expected due to oscillations of the emitted muon neutrinos.

The primary goal of IceCube and consequently of this analysis is the detection of secondary muons produced in charged-current interactions of muon neutrinos with nuclei within or in the vicinity of the detector: $\nu_\mu N \rightarrow \mu^- X$ and $\bar{\nu}_\mu N \rightarrow \mu^+ X$. As Fig. 4.2 shows, the cross section for this reaction increases with E_ν^1 up to energies of $\sim 10^4$ GeV and then flattens to a $E^{0.5}$ profile. While the rising interaction probability improves detection prospects at high energies, it also leads to an increased absorption, e.g. by the Earth, which for IceCube means that neutrinos with $E_\nu \gtrsim$ PeV from the northern hemisphere cannot be detected. In charged-current interactions of muon neutrinos, secondary muons are produced with energies $E_\mu < E_\nu$ and travel nearly collinear with the primary neutrino. The angular deviation $\Delta\omega$ decreases with energy [61]:

$$\Delta\omega \simeq 0.7^\circ \left(\frac{E_\nu}{\text{TeV}} \right)^{-0.7} \quad (4.11)$$

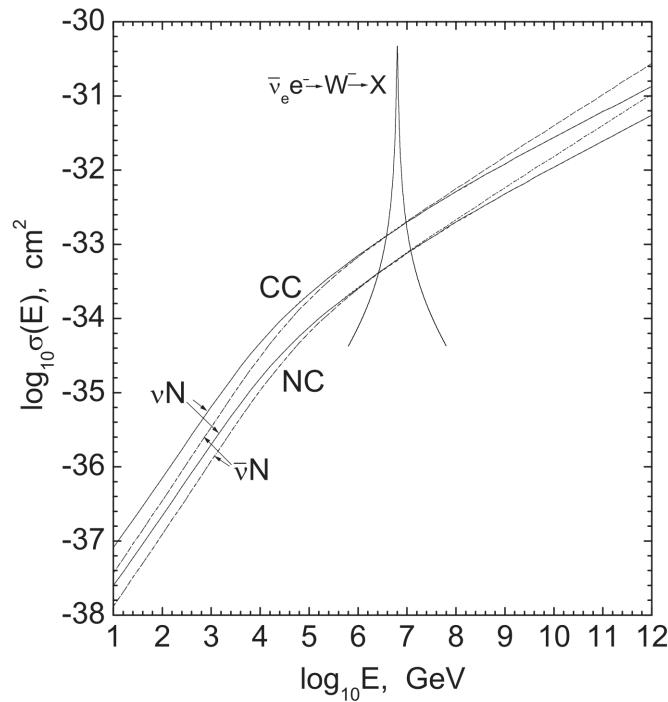


Figure 4.2: νN ($\bar{\nu}N$) cross sections from [54]. Because of lepton universality, cross sections only differ between neutrinos and antineutrinos, not between different flavors. Also shown is the so called *Glashow resonance* for $\bar{\nu}_e e^- \rightarrow W^-$ at $\sim 6 \times 10^6$ GeV.

4.3 Muon Propagation

Muons are well-studied charged particles with a mass of $m_\mu = 105.66 \text{ MeV}/c^2$ and decay after a lifetime $\tau_\mu = 2.2 \times 10^{-6} \text{ s}$. When moving at velocities $v \sim c$, their observed lifetime from a rest frame, e.g. attached to the detector is boosted to $\tau'_\mu = \gamma\tau_\mu$. (This effect was one of the first

confirmations of special relativity.) Therefore relativistic muons produced by high energy neutrinos travel on average a distance $L = \gamma c \tau_\mu$ for an observer at rest. A 400 GeV muon, for example, decays 2,640 km from its production vertex.

In these considerations, muons were assumed to propagate in a vacuum. In the presence of a medium - air, water, ice - muons lose kinetic energy to the medium and therefore slow down. At lower energy, ionization is the principal mechanism for energy loss, while at higher energies $\gtrsim 100$ GeV, bremsstrahlung, photo-nuclear interactions, and e^+e^- pair production become dominant. The average energy loss dE while moving an infinitesimal distance dx can be approximated as:

$$dE_\mu = -(\alpha(E_\mu) + \beta(E_\mu) E_\mu) dx \quad (4.12)$$

The parameters α and β become nearly constant at high energy and have been simulated for ice as $\alpha = 2.9 \text{ MeVcm}^2\text{g}^{-1}$ and $\beta = 5.1 \times 10^{-6} \text{ cm}^2\text{g}^{-1}$ (average values for stochastic energy loss over $E_\mu = 20 - 10^{11}$ GeV [68]). This allows for the calculation of a muon range,

$$R_\mu(E_\mu) = \frac{1}{\beta \rho_{ice}} \ln \left(1 + \frac{\beta}{\alpha} E_\mu \right) \quad (4.13)$$

the average distance a muon of energy E_μ can travel before undergoing catastrophic energy loss, e.g. being captured by an atom. In ice for example, a 2 TeV muon has a range of about ~ 4 km [68]. Thus IceCube can detect neutrinos produced far outside the detector volume which significantly increases its sensitivity. Of course, the muon range is meaningless, if the muon decays into an electron before completing this distance.

4.3.1 Estimated Number of Events for a Supernova at 10 Mpc

At this point, we can make an order-of-magnitude check of the expected number of neutrinos from a slow jet supernova at 10 Mpc detected in an IceCube-sized Cherenkov detector. For this purpose, the detector is assumed to be an area of $A_{geom} = 1 \text{ km}^2$ which detects *every* muon passing through it (if the muon is above a certain energy threshold, here $E_\nu = 10$ GeV). Muons produced in charged-current neutrino-nucleon interactions with the cross section $\sigma_{\nu N}(E_\nu)$ are assumed to obtain half of the parent neutrino energy: $E_\mu = E_\nu/2$. First, for every energy interval dE_ν , the number of nuclei in a volume spanned by A_{geom} and the muon range $R_\mu(E_\nu/2)$ is calculated: $n_{ice} A_{geom} R_\mu$ where $n_{ice} = 4.4 \times 10^{23} \text{ cm}^{-3}$ is the nucleon density in ice. Second, this number is multiplied with the cross section $\sigma_{\nu N}$ to obtain the neutrino effective area and again multiplied with the incident flux $\Phi_\nu(E_\nu)$ (see Sec. 3.5) which yields the number of events in the energy interval dE_ν . Finally, energy integration yields the total number of events:

$$N = n_{ice} A_{geom} \int_{10 \text{ GeV}} R_\mu(E_\nu/2) \sigma_{\nu N}(E_\nu) \Phi_\nu(E_\nu) dE_\nu \quad (4.14)$$

For the numerical evaluation, tabulated cross sections from the CTEQ-5² tables were used and neutrinos and antineutrinos were treated separately. Moreover, the muon range was bounded from below to 1 km in order to include all muons fully contained in the detector. In this way, a signal expectation of $N = 24.2$ was calculated in good agreement with [43] where $N \sim 30$ is quoted for the same parameters.

²<http://www.phys.psu.edu/cteq/>

4.4 Cherenkov Radiation

In a medium, muons do not only lose energy through ionization - if the velocity of their propagation exceeds the speed of light $c' = c/n$ of a medium with refraction index n , they also emit Cherenkov radiation. Although the energy loss to Cherenkov photons is negligible, this radiation is predestined as a detection signature and has inspired an entire class of *Cherenkov detectors*, including IceCube.

Cherenkov emission is treated analogously to the emission of a sonic shock front (Mach cone) by an airplane flying faster than the speed of sound, see Fig. 4.4. As a consequence, Cherenkov photons are emitted at a well defined angle with respect to the muon's direction of motion, the Cherenkov angle θ_c :

$$\cos \theta_c = \frac{1}{\beta n} \quad (4.15)$$

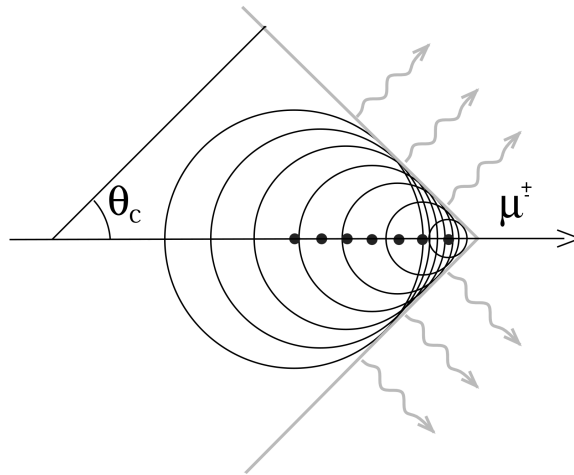


Figure 4.3: Schematic pattern of cone-like Cherenkov radiation emitted by a relativistic muon at an angle of θ_c with respect to the muon momentum.

For highly relativistic particles with $\beta \approx 1$, the Cherenkov angle in a given medium is nearly constant. As muons slow down, they fall below the threshold energy for Cherenkov emission when $\beta n \rightarrow 1$, i.e. $\theta_c \rightarrow 0^\circ$. Apart from a high refraction index n , a good medium for a Cherenkov detector should also be free of ambient light and allow the emitted Cherenkov photons to reach the optical sensors in a straight line, without scattering or absorption. The deep ice, 2 km down in the Antarctic glacier fulfills these requirements extraordinarily well. With $n = 1.33$ ice has a threshold muon energy of $E_{\min,\mu} \approx 120 \text{ MeV}$ and a Cherenkov angle for $\beta \approx 1$ of $\theta_c \approx 41^\circ$. Cherenkov photons emitted by relativistic muons passing through ice have wavelengths primarily in the optical (blue) and UV band, $\lambda = 300 - 600 \text{ nm}$ [58, Ch. 2].

4.5 The IceCube Detector

IceCube is a neutrino detector designed to detect high energy muon neutrinos of cosmic origin [58]. To detect a muon neutrino IceCube measures the Cherenkov radiation emitted by the secondary muon in the dark ice with an array of photomultipliers. Its geometry is optimized for muon neutrinos with primary energies $E_\nu > 100 \text{ GeV}$ and allows for the reconstruction of muon tracks with an angular resolution of $\Delta\theta \sim 1^\circ$. Located at the geographic South Pole, IceCube takes advantage of the properties of the Antarctic glacier, a 3 kilometer thick sheet of ice covering the bedrock of the Antarctic continent. The detector consists of a control center at the surface and a large number of light sensors, frozen into the deep ice 1.5 kilometers below the surface, where complete darkness reigns.

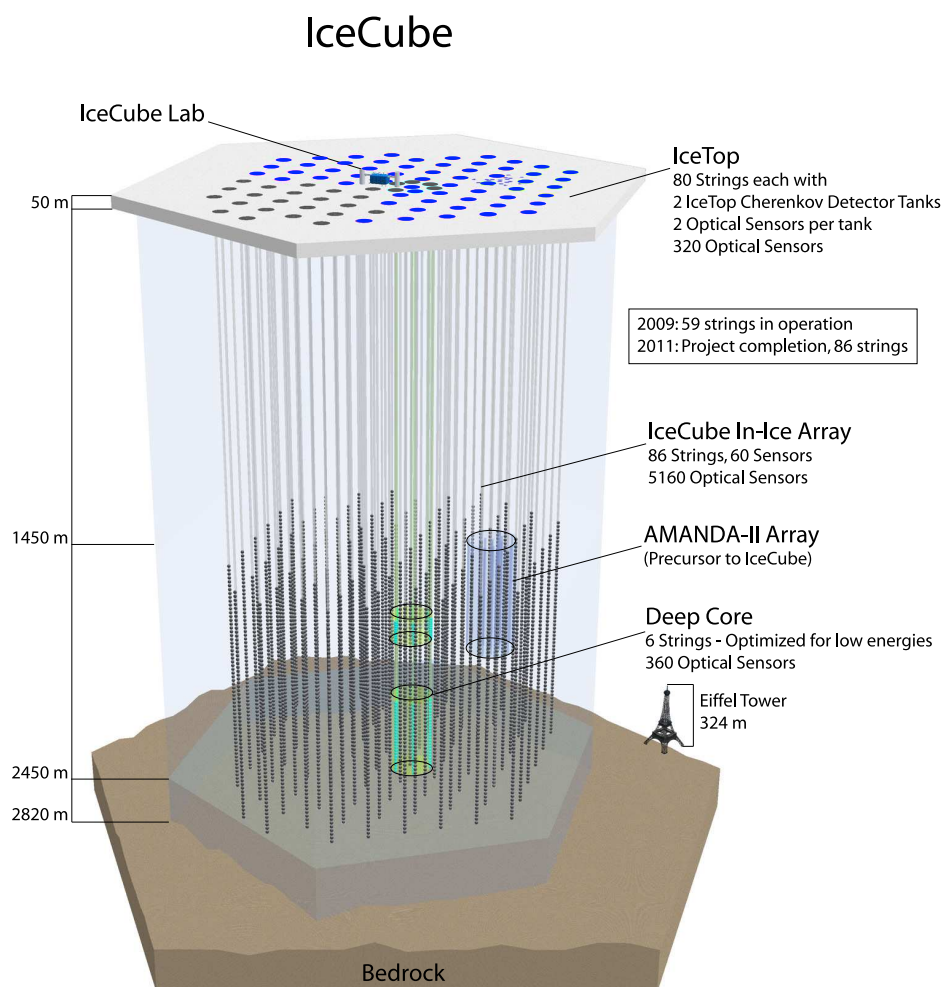


Figure 4.4: Schematic three-dimensional view of the IceCube detector with its components InIce, IceTop, and DeepCore. Also shown is the predecessor of IceCube, the AMANDA II detector which is now contained in IceCube.

4.5.1 Geometry

The instrumented ice volume of IceCube is called *InIce*. It has a hexagonal base, measuring about 1.2×1.2 km, and rises from a depth of 2450 m (roughly 400 m above bedrock) to 1450 m. Thus, one cubic kilometer of deep, highly transparent ice is equipped with light sensors called optical modules. A total of 4,800 optical modules is distributed evenly throughout this volume, aligned on signal and support cables running vertically to the surface. These “strings” are spaced 125 m in a triangular grid. Each of the 80 strings holds 60 optical modules, vertically spaced 17 m from each other. At the surface, two ice tanks containing optical modules are placed above each string, forming the *IceTop* array. IceTop is intended to measure cosmic ray air showers and study the composition of the highest energy cosmic rays.

As an extension to the original IceCube design, *DeepCore*, is being installed until February 2010 and will consist of 6 additional strings arranged in a circle around the central IceCube string. Each DeepCore string carries 60 optical modules, 50 of which are densely spaced (7 m) between a depth of 2100 and 2450 m while the remaining 10 are installed at shallower depths to improve reconstructions of extremely vertical muons. The principle goal of DeepCore is an increased sensitivity to low energy neutrinos, with energies as low as ~ 10 MeV. The installation of IceCube started in late 2004 and is scheduled to be completed by spring 2011. In the construction process, hot water drills are used to create 60 cm wide and 2450 m deep holes filled with melt water into which the strings carrying the optical modules are lowered and locked into position when the hole refreezes. Currently, 79 of the final 86 strings are deployed.

The data used in this analysis was recorded by *IceCube 22*, the intermediate yet fully operational configuration from March 31, 2007 until April 4, 2008, when construction was about 25% completed with 22 strings deployed. In contrast to the final detector which will be nearly invariant under the Earth’s rotation, IceCube 22 was highly asymmetric with an approximately rectangular base. As the Earth rotates, the sensitivity of IceCube 22 for a given direction varies strongly with azimuth (see Figure 5.9 on page 61).

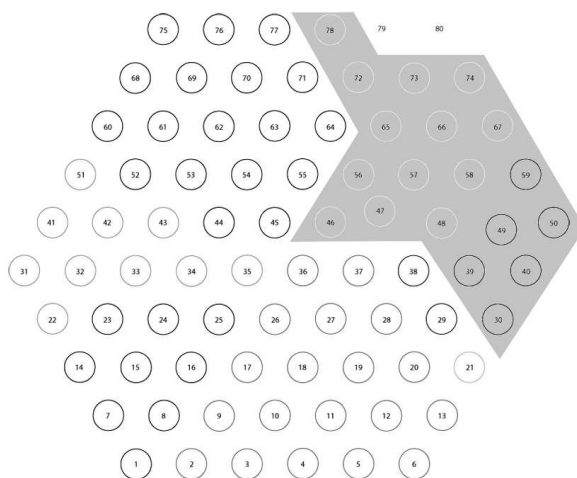


Figure 4.5: Top view of all 80 IceCube holes. The strings deployed in the IceCube 22 configuration are indicated by the shaded area.

4.5.2 Coordinate System

In IceCube, a Cartesian coordinate system is used with an origin approximately at the geometrical center of the detector. The y-axis is “Grid North”, i.e. aligned with the Prime Meridian, pointing towards Greenwich, UK, the x-axis is “Grid East”, pointing 90 degrees clock-wise from Grid North, and the z-axis is normal to the Earth’s surface, pointing “up”. Directions are measured in the azimuth angle ϕ in the xy-plane increasing counter clockwise from the x-axis and the zenith angle θ relative to the z-axis. A particle travelling straight downward into the ice has $\theta = 0^\circ$ while a track coming from the center of the Earth has $\theta = 180^\circ$. Throughout this thesis, tracks with $\theta < 80^\circ$ will be referred to as *downgoing*, those with $\theta > 80^\circ$ as *upgoing*.

4.5.3 Hardware

South Pole Ice

Constituting both the target material for neutrino-nucleon interactions and the optical medium for Cherenkov radiation, the glacial ice in which IceCube is embedded is the principal hardware component of the detector. The Antarctic glacier was formed by snowfall and compression by subsequent snow layers over some 165,000 years. At the relevant depths, below 1.5 km, the ice is highly compressed and free of enclosed gas bubbles. The main source of absorption and scattering are micron-sized dust particles, e.g. from prehistoric volcanic eruptions, that were initially airborne and then trapped in the ice by snowfall. During the drilling of the IceCube holes, the distribution of dust in the ice was measured with millimeter depth resolution. These measurements not only provide important information for detector simulation and calibration but also a valuable climatological record [62], [63]. In the deep ice, a 400 nm photon can on average travel 120 m before begin absorbed and 20 m before undergoing scattering. These ice properties studied in the predecessor detector AMANDA, played a key role in the design of IceCube, e.g. the 125 m string spacing.

Property	Symbol	Value
Mass density	ρ_{ice}	0.92 g cm ⁻³
Absorption length	$\lambda_a(\lambda)$	$\lambda_a(500 - 300 \text{ nm}) \simeq 20 - 130 \text{ m}$
Effective scattering length	$\lambda_e(\lambda)$	$\lambda_e(300 - 500 \text{ nm}) \simeq 20 - 30 \text{ m}$
Index of refraction	$n(\lambda)$	$n(300 - 600 \text{ nm}) = 1.33 - 1.31$

Table 4.1: Properties of South Pole ice. Average values for depths below 1.4 km are given. Note that scattering and absorption have a layered structure and vary by up to a factor of 2 between different layers at a given wavelength. From [63].

Optical Modules

The optical modules are the heart and soul of IceCube. Designed to catch a maximum of the scarce Cherenkov photons (~ 300 per cm track length) emitted by muons passing up to a few hundred meters away, the optical modules house sensitive photomultiplier tubes (PMTs) in their 35.5 cm glass pressure spheres. The PMTs are oriented downward to favor up-going muon tracks and have a peak sensitivity at 420 nm reaching a gain of 10^7 over ten high

voltage dynodes. When a photon hits the PMT, a discriminator triggers the signal readout and voltage pulses are digitized within the module by two complementing analog-to-digital converters, the first (ATWD) sampling a short time window of 400 ns with a resolution of $\Delta t_{RMS} \approx 3.3$ ns, while the second (FADC) covers a longer time span of 6.4 μ s at a lower resolution to include scattered late photons in high energy events. Each optical module communicates with its neighbor to establish whether they have been hit in a “local coincidence”. Only if this requirement is met, the digital *waveform* - electrical charge over time - is sent to the surface through ordinary twisted pair cables. To allow for in situ calibration and measurements of the ice properties after deployment, each optical module is equipped with LED flashers that emit light of a defined intensity .

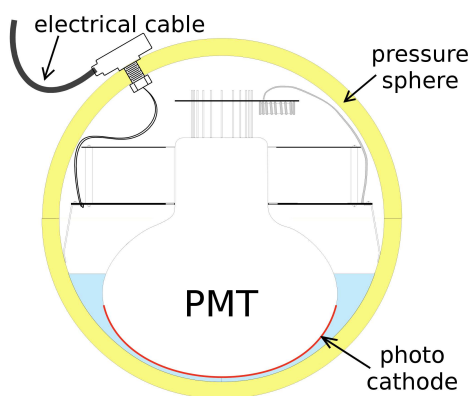


Figure 4.6: Schematic design of an optical module containing a photomultiplier tube (PMT).

Strings

After serving their initial purpose of holding the optical modules in place until the melt water refreezes, the strings provide a data link to the surface through twisted pair network cables. In the IceCube lab at the surface, a *string processor* (Linux PC) gathers the data from all 60 optical modules and establishes whether further coincidence requirements are met.

Computing

If a series of signals causes the trigger system to fire, raw data from all strings is gathered in a computer cluster, the Processing and Filtering (PnF) cluster, which combines the data from the various hit strings into events and distributes the events to so called Filtering Clients. These run first, fast reconstruction algorithms and use their results to reduce the event rate to a bandwidth which can be transferred to the North via satellite link (GOES-3 and TDRS satellites, maximum bandwidth ~ 55 GB/day).

4.5.4 Software

Trigger

Several levels of triggers help to avoid the readout and processing of noise signals or background events [46]: First, the beforementioned *local coincidence* trigger running in the elec-

tronics of each optical module rejects any signal not accompanied by a neighboring hit³. From this point down the data processing chain, all triggers are software-based and run on ordinary Linux computers. They use only the arrival time of the first photon hit; the full waveform is only read out after a positive trigger decision. While *string triggers* running of each string processor and *subdetector triggers* for InIce/IceTop are incorporated in the IceCube design and provide the possibility of low level triggering, IceCube 22 data taking relied on a simple *global trigger*, the *simple multiplicity trigger* which required 8 hit modules within $5\ \mu\text{s}$. Once a global trigger fires, the full raw data within a minimum $21\ \mu\text{s}$ time window⁴ around the trigger condition is read out by the *event builder*, combined into an event, and sent to the online filtering system.

Data Processing

IceCube software is divided into online and offline software: *Online* software runs on the computers at the South Pole and must operate in real-time and use the slim computing resources sparingly (power supply computing is provided by generators whose operation at the South Pole has significant costs). The tasks of the online software are the extraction and calibration of the relevant information from the raw data, the evaluation of trigger decisions to reject noise and background events, and the execution of first-guess reconstruction algorithms to further reduce background events. *Offline* software is run on computing clusters in the North (e.g. at University of Wisconsin at Madison) and comprises sophisticated, computationally intensive reconstructions.

Online Processing

During online filtering, the raw data is calibrated module by module using the measured characteristics of each sensor and the data from 29 optical modules which have known malfunctions is removed from the event (launch cleaning). Then, fast first-guess algorithms attempt to reconstruct different signatures, including a simple line fit for muon tracks (see Sec. 5.3.2 below), and subsequent cuts on the output parameters of these reconstructions are applied. For events passing all these selection criteria, the full raw data, that is waveforms from all hit modules, is sent to the North via satellite.

Offline Processing

Data arriving from the South Pole is distributed to a number of computing clusters, where more sophisticated data processing is possible. The most important part of this *offline* processing with respect to this analysis are likelihood reconstructions (see Sec. 5.3.3). In this analysis data was processed at the NPX2 cluster at the University of Wisconsin, Madison, and at the CPU farm at Desy, Zeuthen.

³In IceCube 22, the local coincidence span was set to 2, requiring at least one hit in one of the nearest or second-nearest neighbor modules.

⁴Note that muons travelling at $v \approx c$ traverse the detector in no more than $3\ \mu\text{s}$.

Chapter 5

Analysis of SN 2008D

Supernova 2008D represents an ideal candidate for a cosmic neutrino source detectable by IceCube. The slow jet model discussed in Sec. 3.5 predicts a significant flux of muon neutrinos based on known phenomena and observations and the detector was in full operation at the time of SN 2008D. In this context it is not surprising that even the discoverers of SN 2008D suggested that neutrino astronomers search for neutrinos emitted by this supernova [39]. The immense challenge of finding no more than one or two events within a constant torrent of background events is generally insuperable for supernovae since their timing uncertainty is on the order of days. SN 2008D was, however, pinned down much more precisely, and a simple back-of-the-envelope calculation shows that a dedicated IceCube analysis of SN 2008D is worthwhile. Consider an experiment simply counting the number of neutrinos within 100 seconds. Background events shall occur at a very low average rate of b events per 100 s bin and the number N of events in each bin is assumed to be Poisson-distributed $p_b(N) = b^N e^{-b}/N!$. We demand that two observed events contradict the background-only hypothesis at a significance level of 5 sigma, in other words a background fluctuation resulting in the observation of two events or more shall occur no more than once in a million trials. Next, we calculate the required background rate b under these conditions:

$$\sum_{N>1}^{\infty} p_b(N) \approx p_b(2) \stackrel{!}{<} 10^{-6} \quad \Rightarrow \quad b \lesssim 0.001 \quad (5.1)$$

First, measuring such a background rate requires a background dataset of at least $t > \frac{100s}{b} \approx 1$ day lifetime, ideally a factor of 100 more to establish a statistically solid mean. This criterion is easily met in the case of IceCube as Sec. 5.2 will show. Second, assuming an initially higher background rate \sim Hz, selection cuts reducing background to 10^{-5} Hz need to be found. A look at the results of the recent IceCube 22 point source analysis [50] which had a final event rate of $\sim 10^{-4}$ Hz suggests that a significant detection of SN 2008D is within reach with minor improvements. This chapter shall document how this analysis has achieved this goal.

5.1 Methodology

The methodology of the present analysis can roughly be divided into three steps: The assembly of sufficient background data and the production of signal data through Monte Carlo simulations (Sec. 5.2 - 5.5), the development of optimized selection cuts to separate signal and background (Sec. 5.6 - 5.7), and finally their application on the relevant experimental data and the interpretation of the results (Ch. 6). Fig. 5.1 gives an overview of the principal tasks in each of these steps.

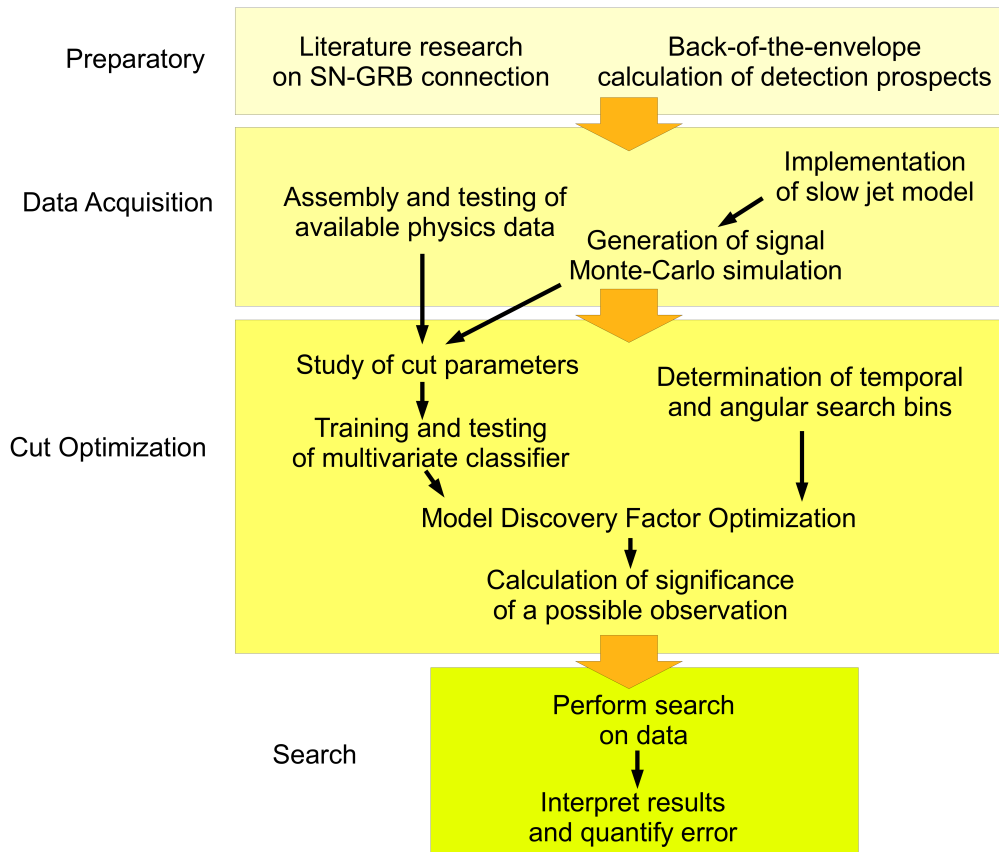


Figure 5.1: Methodology of this analysis.

5.2 Background Data

The data sample used to measure and characterize background was taken by IceCube in the 22 string configuration over 275.72 days of detector live time between May 2007 and March 2008. The sample is identical to the one used for the *IceCube 22 Point Source Analysis* [50]. In IceCube, experimental data is organized in *runs* of several hours duration. In order not to include signal in the background sample, the run during which the supernova was detected was kept *blind*, i.e. excluded from the development phase of the analysis. This *signal run* started ~ 40 minutes before the detected X-ray flare from SN 2008D and ended ~ 110 minutes after (2.7 hours total). Due to the uncertainty in the time of the neutrino emission, the two runs preceding the signal run were kept blind as well. Nevertheless, event rates during the

signal run were analyzed at a low (background-dominated) cut level to that the detector was in stable operation during the supernova observation.

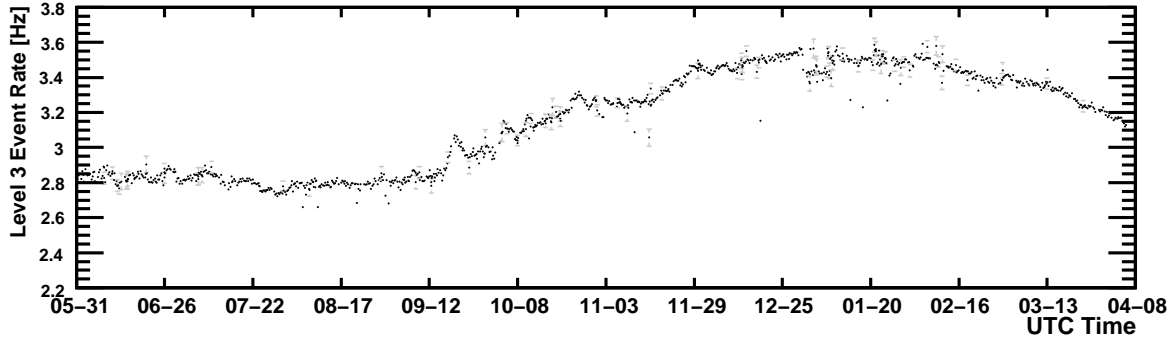


Figure 5.2: Level 3 Event rates of detector runs between May 2007 and March 2008 at filtering level 3 (see Sec. 5.3.9). Dates are given in the format month-day. Each dot represents a detector run. Statistical errors are only discernible for short (< 1 hour) runs.

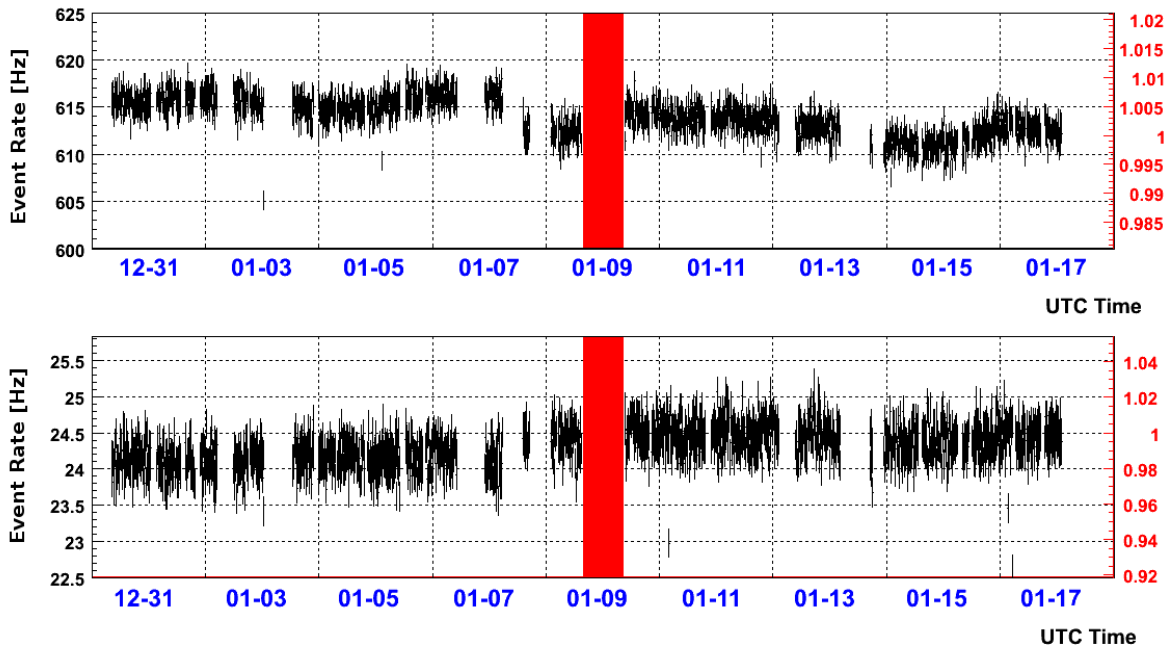


Figure 5.3: Trigger rates (top) and muon filter rates (bottom) for January 2008. the bin size is 10 minutes, lines indicate Poissonian error. Dates are given in the format month-day. The shaded region indicates the blinded data. The relative scale on the right hand side illustrates the scale of the rate fluctuations, consistent with purely statistical fluctuations of a steady flux.

Background data consists of two principal components:

5.2.1 Reducible Background

Most events that trigger IceCube are muons produced by cosmic rays in the upper atmosphere. Unfortunately, event reconstruction algorithms often *misreconstruct* them as coming

through the Earth from below, not from above. Thus, even when looking in the direction of SN 2008D ($\theta = 123^\circ$ i.e. through the Earth) a large number of these noise events appear to come from this direction. Mistaking downgoing particles for up-going, however, the reconstructions of these events yield poor quality parameters (see Table 5.1). This allows for a rejection of most atmospheric muons through selection cuts on such quality parameters. Consequently, atmospheric muons constitute a *reducible background*. Now how can we be certain, that we really see atmospheric muons in the data? The atmospheric muon rate varies with the seasons, i.e. the atmospheric temperature and density. In Fig. 5.2, this variation is clearly visible. Furthermore, cosmic rays have been studied and measured with great precision. The expected rate of atmospheric muons produced by cosmic rays has been successfully reproduced by the Monte-Carlo simulation software CORSIKA, described in Sec. 5.5.1. The CORSIKA results agree very well with the measured data and demonstrate that background in IceCube mainly consists of misreconstructed atmospheric muons - for details see Appendix A.3.

5.2.2 Irreducible Background

At very high filter level, events that unmistakably traverse the detector from the bottom towards the top become the dominant constituent of the data. They are muons produced below or within the detector by neutrinos, which have penetrated the Earth. Most if not all of these neutrinos are produced by cosmic rays hitting the atmosphere over Northern hemisphere. Their rate is expected to be constant over time and depend only on the zenith angle, that is on how much material they have to traverse. Unfortunately, there is nothing which distinguishes atmospheric neutrinos from cosmic neutrinos originating e.g. from a supernova. Therefore, atmospheric neutrinos are an *irreducible background*. Their expected rate can be determined through Monte-Carlo simulations based on the well-studied properties of cosmic rays (See Sec. 5.5.2). Luckily, for a sufficiently small angle and time interval as used in this analysis, the irreducible background does not overwhelm the expected signal: For example, 0.001 atmospheric neutrino events are predicted by simulations within 100 seconds and within a 10-degree circular aperture, while 0.25 events are predicted for SN 2008D (see Sec. 5.4.3). This ratio can be further improved by applying selection cuts which favor the direction and the slightly higher energy spectrum of SN 2008D. Comparing the signal expectations to the *irreducible* background expectation only is reasonable, since it is indeed possible to remove all reducible background and obtain a pure irreducible background sample. In this process, some atmospheric neutrinos are inevitably lost, too. However, multivariate selection cuts can yield a pure sample of atmospheric neutrinos while losing only about 50% of them and even less of the simulated signal for SN 2008D ($\sim 60\%$). These issues will be examined in greater detail in Sec. 5.7.

5.2.3 Necessary Statistics

As discussed above, background can be reduced to arbitrarily low levels with a suitable set of selection cuts - although signal is lost at the same time - and it is possible to remove background altogether if cuts are chosen sufficiently strong. For example, once all reducible background is removed from the 275 day data sample, only about 5000 atmospheric neutrino events remain and their rate is only about 0.2 mHz. At these high filtering levels, long-time measurements are required to determine the average rate with sufficient confidence. The limiting factor in reducing the background is the fact, that if cuts leave only a few events, the

uncertainty in the thus measured rate becomes very large due to statistical (Poissonian) fluctuations: the measurement “runs out” of background events. A background measurement at a cut level where e.g. only 10 events are observed has a statistical error of $1/\sqrt{N} \approx 33\%$. Once all background events are rejected by cuts, the expected rate can no longer be reduced or predicted in a meaningful way. - Thus the larger the background dataset, the more the background rate can be reduced and the more precisely it can be predicted. For these reasons, the largest available sample of background data, the full 275.72 days of IceCube 22 operation were used in this analysis. As a convenient side effect, seasonal effects in the background data were “averaged out” in this manner since the sample covers roughly one calendar year.

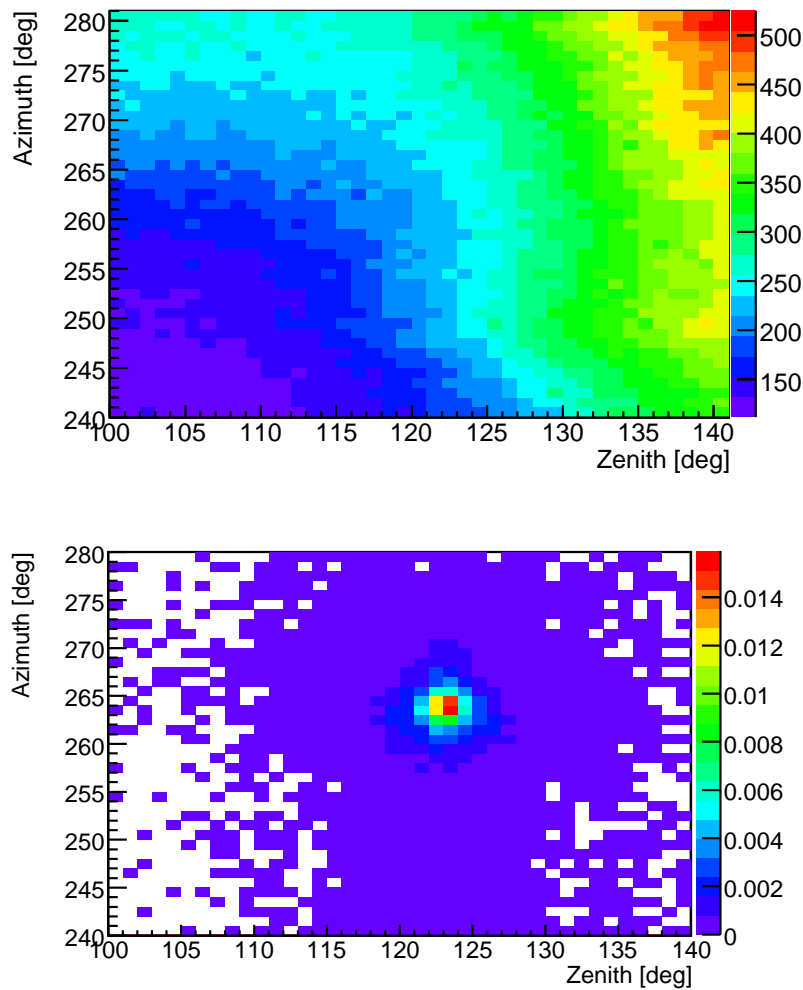


Figure 5.4: Distribution of *reconstructed* directions in detector coordinates (arbitrary linear color scale). Bins are weighted with their inverse solid angle $(\sin \theta d\theta d\phi)^{-1}$. **Top:** 275-day data sample. **Bottom:** simulated signal for SN 2008D. The data plot is dominated by misreconstructed downgoing muons, atmospheric neutrinos are not discernable at this filtering level. The inhomogeneous distribution of the misreconstructions is owed to the detector geometry. Signal simulation shows a strong concentration around the true direction of SN 2008D. The source appears point-like since the Earth’s rotation only causes a smearing-out of 0.4° degrees in azimuth for an assumed neutrino flash of 100 s duration.

5.3 Data Processing in IceCube

IceCube 22 was triggered roughly 500 times each second. If all these events were recorded, this analysis would have to cope with some 12 billion events and the chance of finding a single supernova neutrino would be close to zero. To reach the low background rates mentioned in the previous section, a number of sophisticated reconstruction algorithms is sequentially applied to experimental data.

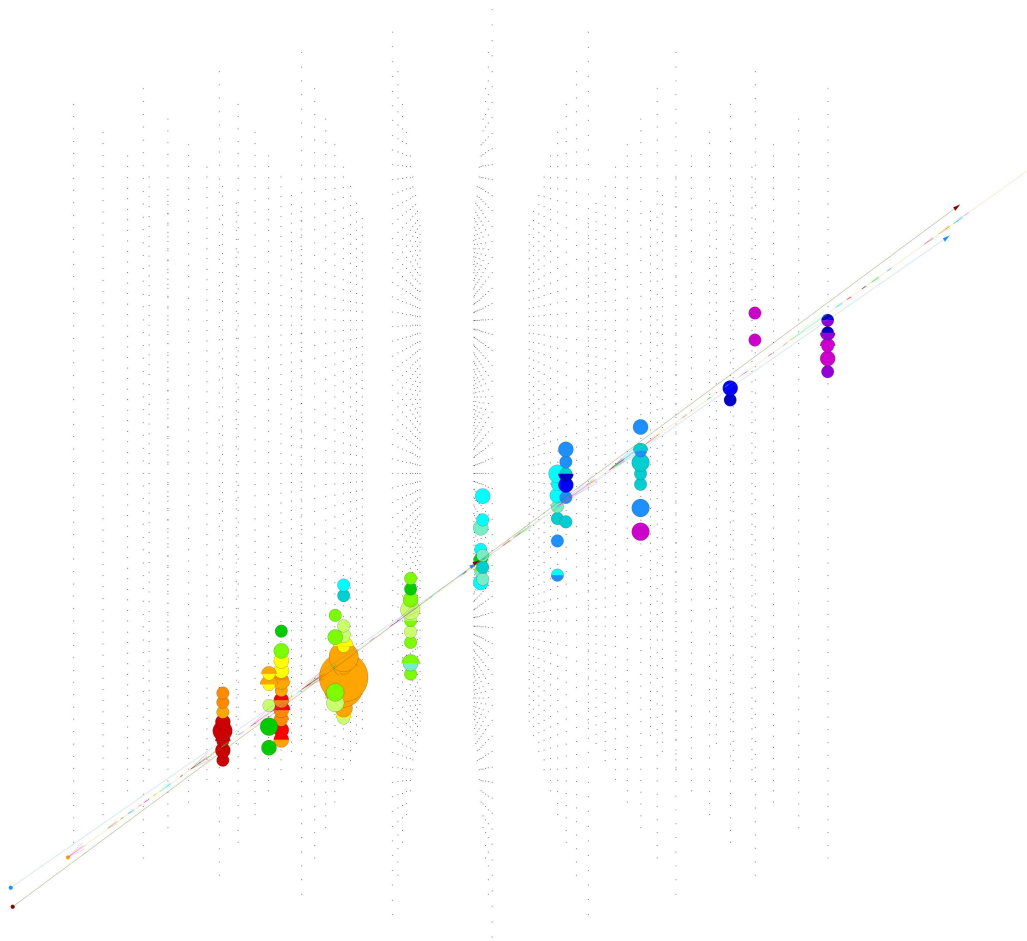


Figure 5.5: This simulated 10 TeV muon track in IceCube illustrates a typical hit pattern. Dots represent optical modules, colored circles indicate hit modules, with red circles hit earliest and violet circles latest. Circle size corresponds to number of detected photons. Note that this figure shows the full 80 string detector.

5.3.1 Reconstruction Basics

Each optical module in IceCube produces digital time series of the recorded signal (waveforms) corresponding to the electric current in the photomultiplier caused by incident photons. In a first processing step called *feature extraction*, *pulse series* consisting of (time, charge) pairs are extracted from the waveforms where the charge (height) of a pulse corresponds to

the number of photons it contains. Next, a sliding time window of $6\mu\text{s}$ is adjusted to contain a maximum number of hit modules and all pulses outside of this window are discarded. This procedure is referred to as *time window cleaning*. The challenge for the reconstruction algorithms is to find the track¹ hypothesis best matching the pattern of photon arrival times at all optical modules $\{t_i\}$ with $i = 1, 2 \dots N$. Commonly used reconstruction algorithms in IceCube only use the first pulse in each cleaned pulse series and do not make use of the charge (\sim number of photons) of each pulse. These *single photoelectron* (SPE) methods have been used in the present analysis. *Multi photoelectron* (MPE) algorithms were evaluated, but proved to yield no advantages in the context of this analysis, that is at high filtering levels and energies $< 10^{4.5}$ GeV (for details, see Sec. 5.6.2).

5.3.2 First-Guess Line Fit

The first-guess line fit algorithm [48] is run online at the South Pole to reconstruct the direction of muon tracks and allow for the rejection of downgoing tracks of atmospheric origin which are an unwanted background for astrophysical analyses. It uses the arrival times $\{t_i\}$ of the first photon hits at all triggered modules and assumes that all light originates from a single vertex \vec{r} , travels parallel, unscattered, and unabsorbed along a velocity vector \vec{v} and reaches the i -th module at position \vec{r}_i after a time t_i . Under these assumptions illustrated in Fig. 5.3.3, the vertex position is approximately given by:

$$\vec{r} \simeq \vec{r}_i - \vec{v} t_i \quad (5.2)$$

where \vec{v} is the velocity vector and \vec{r} the vertex position.

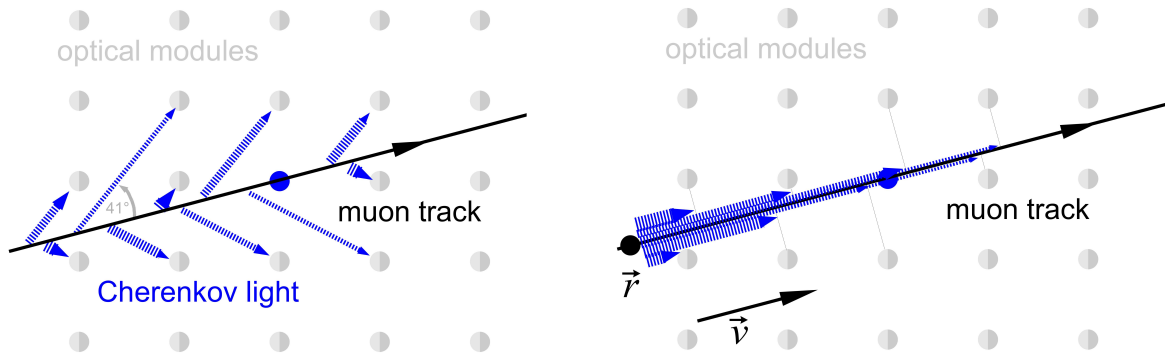


Figure 5.6: **Left:** Physical light signature of a muon track. **Right:** Simplified light propagation hypothesis for the line fit reconstruction.

The fit parameters \vec{v} and \vec{r} can be found by minimizing the residual χ^2 :

$$\chi^2 = \sum_{i=1}^N (\vec{r}_i - \vec{r} - \vec{v} t_i)^2 \quad (5.3)$$

¹Cascade reconstructions shall be omitted in this thesis. For a detailed description, see [60].

The analytical minimization of χ^2 with respect to \vec{v} and \vec{r} allows for their direct calculation from the measured t_i and known \vec{r}_i :

$$\vec{v} = \frac{\langle v_i t_i \rangle - \langle v_i \rangle \langle t_i \rangle}{\langle t_i^2 \rangle - \langle t_i \rangle^2} \quad \vec{r} = \langle r_i \rangle - \vec{v} \langle t_i \rangle \quad (5.4)$$

Here, $\langle \dots \rangle$ denotes the mean over all hit modules $i = 1, 2 \dots N$. This simple algorithm can be computed for all triggered events in real time. The obtained direction $\vec{n} = \vec{v}/v$ serves as a first cut parameter to reject downgoing muon tracks ($\theta < 80^\circ$). Moreover, the reconstructed vertex and direction are used as a seed (initial guess) for more sophisticated likelihood reconstructions.

5.3.3 Likelihood Track Reconstruction

If the probability with which a model with a set of parameters $\mathbf{a} = \{a_i\}$ leads to the observation of a quantity x_i is known and can be analytically expressed by a *probability density function* $p(x_i | \mathbf{a})$, we can write down a *likelihood function*:

$$\mathcal{L}(\mathbf{x} | \mathbf{a}) = \prod_{i=1}^N p(x_i | \mathbf{a}) \quad (5.5)$$

which quantifies how likely the observation of the values $\mathbf{x} = \{x_i\}$ is for a source model with the parameters \mathbf{a} , or in other words how well described the observation is by the model with the parameters set to \mathbf{a} . By maximizing the likelihood function by varying the parameters \mathbf{a} , the model best explaining the observation can be identified, i.e. the physical event can be reconstructed. For computational reasons, it is common to minimize the negative log-likelihood $-\log \mathcal{L}$ instead of maximizing \mathcal{L} .

Adapting the likelihood approach to the reconstruction of muon tracks [48], the parameters of interest are the track vertex $\vec{r} = \{x, y, z\}$, the time of vertex passage t , and the direction (θ, ϕ) , in short $\mathbf{a} = \{x, y, z, t, \theta, \phi\}$. The available measurements consist in the arrival times of the first photon detected at each optical module $\mathbf{t} = \{t_1, \dots, t_N\}$. For unhit modules the index i is omitted in the calculation of Eq. 5.9 so that the product has only $N_{hit} \leq N$ factors.

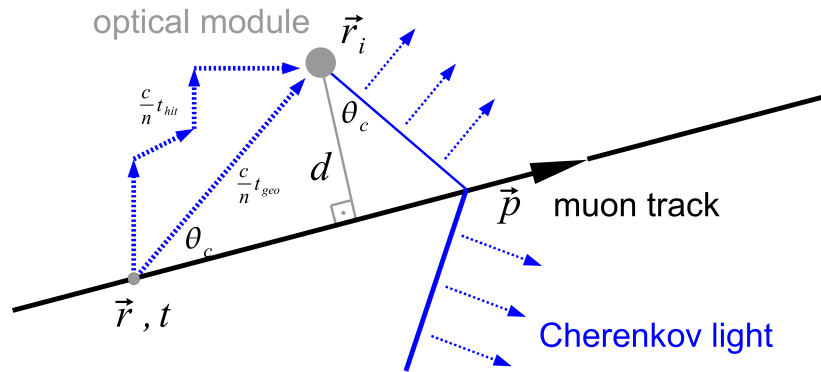


Figure 5.7: Useful notation for the calculation of a track likelihood function. If scattered, a photon arrives a time $t_{res} = t_{hit} - t_{geo}$ later than in the unscattered case.

In order to find a relation between a track hypothesis and an observed hit pattern $\{t_i\}$, we make a useful variable substitution using the notation shown in Fig. 5.3.3 and introducing the *residual time* $t_{res,i}$:

$$t_{hit,i} = t_i - t \quad (5.6)$$

$$t_{res,i} = t_{hit,i} - t_{geo,i} \quad (5.7)$$

$$t_{geo,i} = t + (\vec{\mathbf{p}}/p \cdot (\vec{\mathbf{r}} - \vec{\mathbf{r}}_i) + d_i \tan \theta_c) / c \quad (5.8)$$

where t is the time of passage through a vertex $\vec{\mathbf{r}}$ arbitrarily chosen along the track, $\vec{\mathbf{p}}$ is the muon momentum vector, θ_c is the Cherenkov angle in ice, and c is the vacuum speed of light. The impact parameter d_i is a fixed parameter easily calculated from a module's positions and the given track hypothesis. The residual time $t_{res,i}$ is zero for a *direct hit*, that is a Cherenkov photon arriving unscattered at the optical module. The likelihood function can now be expressed analytically and in terms of $\mathbf{t} = \{t_{res,i}\}$:

$$\mathcal{L}(\mathbf{t} | \mathbf{a}) = \prod_{i=1}^N p_P(t_{res,i} | d_i) \quad (5.9)$$

where $p_P(t_{res,i} | \mathbf{a})$ is the so called Pandel function [49] describing the distribution of residual times for a given impact parameter:

$$p_P(t_{res,i} | d_i) = \frac{1}{N(d_i)} \frac{\tau^{-d/\eta} t_{res}^{d/(\eta-1)}}{\Gamma(d_i/\eta)} \exp \left\{ - \left[t_{res} \left(\frac{1}{\tau} + \frac{c}{n \lambda_a} \right) + \frac{d_i}{\lambda_a} \right] \right\} \quad (5.10)$$

with the gamma function Γ and a normalization constant:

$$N(d_i) = e^{-d_i/\lambda_a} \left[1 + \frac{\tau c}{\lambda_a n} \right]^{-d_i/\lambda_a} \quad (5.11)$$

Here, η and τ are free parameters obtained from simulation studies of photon propagation in ice, λ_a is the absorption length and n the refractive index in ice (see Sec. 4.5.3). In addition, the Pandel function is convoluted with Gaussian noise through a simple integral transform, in order to account for the jitter of the photomultipliers. Despite the daunting looks of these formulas, they are easily evaluated numerically and yield a single number, the negative log-likelihood for each track hypothesis. Finding the global minimum of this function in a five dimensional parameter space is now merely a computational problem for which generic solutions exist. In IceCube reconstructions, the TMinuit package offered in ROOT² is used for this purpose. This minimization algorithm is seeded with the first guess parameters from the line fit method described above. Moreover, the minimization is re-run with varying seeds in an *n-fold iteration* in order to prevent the minimization to be trapped in a *local* rather than *global* minimum. In this analysis, a first 1-iteration reconstruction seeded with the line fit results was used seed another 32-iteration track fit, the currently most precise track reconstruction algorithm available in IceCube.

5.3.4 Umbrella Track Reconstruction

This procedure is identical to the aforementioned in all but one aspect: The 32-iteration minimization is seeded with the inverse of the direction determined by the 1-iteration likelihood reconstruction. If this flipped fit results in a likelihood \mathcal{L}_{Umb} exceeding \mathcal{L} , the track is more likely downgoing and can be rejected by a selection cut on the ratio $\log(\mathcal{L}_{Umb}/\mathcal{L})$.

²<http://root.cern.ch>

5.3.5 Bayesian Likelihood Track Reconstruction

In this reconstruction, the likelihood is formulated as follows:

$$\mathcal{L}_B(\mathbf{a}|\mathbf{t}) = \prod_{i=1}^N p(\mathbf{a}|t_{res,i}) \quad (5.12)$$

In contrast to Eq. 5.9, this describes the likelihood of obtaining the reconstruction result \mathbf{a} given the arrival times \mathbf{t} . Bayes' theorem is used to express the new product probabilities in terms of the Pandel function:

$$p(\mathbf{a}|t_{res,i}) = \frac{p_P(t_{res,i}|\mathbf{a}) p(\mathbf{a})}{p(t_{res,i})} \quad (5.13)$$

This procedure introduces additional probability density functions, so called *Bayesian priors*: While $p(t_{res,i})$ can be chosen constant since no residual time is favored per se, the intrinsic probability $p(\mathbf{a})$ of a certain track hypothesis can be approximated from the measured distribution of atmospheric muons which constitute the overwhelming majority of the events. Their distribution is known to be strongly zenith dependent due to the absorption of muons below the horizon. Therefore the approximation

$$p(\mathbf{a}) = p(x, y, z, \theta, \phi) \approx p(\theta) = \begin{cases} \text{large} & \theta < 90^\circ \\ \text{small} & \theta > 90^\circ \end{cases} \quad (5.14)$$

is justified and leads to

$$\mathcal{L}_B = \mathcal{L} \cdot p(\theta) \quad (5.15)$$

As a result of this alternative approach, the minimization routine favors tracks describing a downgoing muon and disfavors those misreconstructed as up-going. Therefore, poorly reconstructed up-going muons - most likely misreconstructed downgoing particles - can be identified by their small Bayesian likelihood (i.e. large $-\log \mathcal{L}_B$). The only parameter from the Bayesian reconstruction used in this analysis is the *Bayesian ratio* (see Table 5.1) which takes small negative values for well-reconstructed up-going tracks.

5.3.6 Split Track Reconstruction

Another source of contamination of the data are pairs of atmospheric muons creating complex hit patterns easily mistaken for single upgoing tracks. A strategy to identify and remove these events is two split all hits belonging to an event in two parts according to their time and to perform a separate reconstructions on each part (namely 1-iteration likelihood track reconstructions). Thus, two *sub-tracks* are obtained, aligned for single events and diverting for coincident events and/or downgoing events. For the latter, one of the two tends to reconstruct as downgoing. This procedure also helps to evaluate the quality of the direction reconstruction of an upgoing track, since - if both parts are reconstructed parallel and up-going - the inverse direction is highly unlikely. In this analysis, the minimum of the two sub-track zeniths is used as a cut parameter.

5.3.7 Paraboloid Fit

The paraboloid method is a secondary reconstruction performed on the results of the likelihood track reconstruction. It attempts to fit a paraboloid to the two-dimensional likelihood

function over the (θ, ϕ) -plane. The paraboloid is sliced at the point where $-\log \mathcal{L}$ has increased by 0.5 with respect to the minimal value. The slice has the shape of an ellipse and its half axes can be used to estimate the uncertainty of the directional reconstruction.

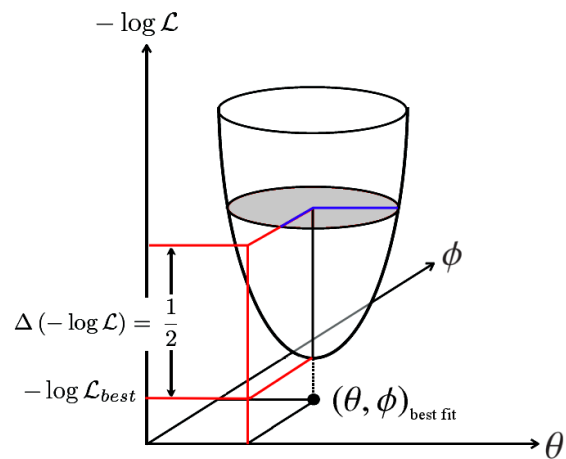


Figure 5.8: Illustration of the paraboloid fit procedure.

5.3.8 Quality Parameters

The quality of a final fit can be quantified by a number of parameters calculated by the minimization software. For likelihood reconstructions, these parameters evidently comprise the negative log-likelihood itself. Table 5.1 lists the quality parameters relevant in this analysis.

Parameter	Description
$-\log \mathcal{L}$	log-likelihood Minimum value of the log-likelihood obtained in the 32-iteration track fit
$\mathcal{L}_R = -\frac{\log \mathcal{L}}{N_{dof}}$	Reduced log-likelihood log-likelihood divided by the number of degrees of freedom (dof). N_{dof} is given by the number of hit modules minus the 5 parameters of the track fit. With this normalization, the likelihood for events with few / many hit modules can be compared.
$N_{dir,E}$	Number of direct hits (from 32-iteration track reconstruction) A hit is considered direct if it arrives within a short time window around the time of arrival predicted for unscattered Cherenkov emission, that is $-15 \text{ ns} < t_{res} < 250 \text{ ns}$
$L_{dir,E}$	Direct hit length Length between the two most extreme projections of the direct hits onto the track based on the $N_{dir,E}$ hits
S_{all}	Smoothness Smoothness parameter (based on all hits): Parameter describing of the distribution of hit projections onto the track. A well reconstructed track has a continuous energy deposition along the particle path and small values of $ S_{all} $.
$\theta_{ST,min}$	Minimum split track zenith Minimum of the two zenith angles from the split track (ST) reconstruction. This variable requires that at least one of the split track fits has succeeded.
σ_p	Paraboloid Error Root mean square of the two half axes of the paraboloid fit to the likelihood function in (θ, ϕ) -space. σ_p is measured in radians and quantifies the angular uncertainty of the reconstructed track direction.
$R_B = \log \mathcal{L} / \mathcal{L}_{Bayes}$	Bayesian ratio Logarithm of the ratio of the likelihoods from the standard and the Bayesian 32-iteration track fit.
$R_U = \log \mathcal{L} / \mathcal{L}_{Umb}$	Umbrella ratio Logarithm of the ratio of the likelihoods from the standard and the inverted 32-iteration track fit.

Table 5.1: Quality parameters used in this analysis.

5.3.9 Processing and Filtering Levels

IceCube data is processed and reduced in several stages also referred to as levels. Each level comprises reconstructions and subsequent selection cuts. The event rate is thus reduced from 600 Hz at trigger level to 3 Hz at level 3. In this analysis, level 3 was used as the starting point and an additional angular cut to a 10° signal region was applied to bring the data volume down to a manageable size. The full 275.72 day raw background sample - 7.5 million events or roughly 2 TB of data at Muon Filter level - was reduced to 860,000 events or 56 MB at level 4.

Level	Rate [Hz]	Reconstructions	Applied Cuts
Trigger Level	~ 600	waveform digital-analog conversion	Simple coincidence trigger: 8 hit modules within $5 \mu s$
Muon Filter (online)	~ 25	pulse extraction time window cleaning line fit	$(\theta_{\text{linefit}} \geq 70^\circ \text{ and } N_{ch} \geq 10)$ or $(\theta_{\text{linefit}} \geq 60^\circ \text{ and } N_{ch} \geq 40)$ or $(\theta_{\text{linefit}} \geq 50^\circ \text{ and } N_{ch} \geq 50)$ where N_{ch} is the number of hit modules
Level 1 (Offline)	~ 25	improved pulse extraction time window cleaning line fit	none
Level 2	~ 25	1-iteration likelihood fit 1-iteration Bayesian fit 1-iteration paraboloid fit Split track fit	none
Level 3	~ 3.1	32-iteration likelihood fit 32-iteration Bayesian fit 32-iteration paraboloid fit 32-iteration Umbrella fit	$\mathcal{L}_{R,1-iter} \leq 13$ $\theta_{1-iter} \geq 80^\circ$ $\theta_{32-iter} \geq 80^\circ$
Level 4	$\sim 3.0 \times 10^{-2}$	none	32-iteration track direction \vec{n} must lie within 10° of SN 2008D $\Delta\omega = \arccos(\vec{n}_{SN} \cdot \vec{n}) < 10^\circ$ for passing events, the paraboloid fit and at least one split track reconstruction must have converged

Table 5.2: Filtering levels for IceCube 22 muon data.

5.4 Signal Simulation

When searching for something particular, we need to know *what* we are looking for. Since nobody has ever detected high energy neutrinos from a core collapse supernova, the question arises what they would look like in the detector. While the slow jet model is a plausible scenario, it only models the *source*. The only way to get an idea of how such a source would be visible in processed data is to run a full simulation of such supernova neutrinos traversing the Earth, decaying into muons, the muons emitting Cherenkov photons, the photons propagating and hitting optical modules, and the modules converting photon signals into electrical pulses triggering IceCube. Such simulations rely on random generators to model stochastic processes and are therefore called *Monte Carlo* simulations. IceCube simulation software is sophisticated enough to predict not only how many events to expect from a given source, but also what these events look like. This information can be used to distinguish the simulated signal from background data and to develop a suitable filter for the final search in experimental data.

5.4.1 Simulation Production

Neutrino Generation

The first step in simulation production is the generation of primary neutrinos according to a power law spectrum $\propto E^{-\alpha}$, in this analysis $\alpha = 1$ between $E_{min} = 10 \text{ GeV}$ and $E_{max} = 10^5 \text{ GeV}$. Using a generic spectrum rather than a particular source spectrum allows for a more versatile use of simulation data by later reweighting the primary spectrum. For the simulation of atmospheric events, primary neutrinos are distributed over a full 4π solid angle, while for the simulation of SN 2008D primary events were generated in a small box $\Delta\Omega = 0.01^\circ \times 0.002^\circ$ around the supernova coordinates - a trick that allowed using standard simulation software, namely *neutrino-generator*. For this analysis, only muon neutrinos were generated.

Neutrino Propagation

Neutrino-generator also simulates each neutrino's propagation through the Earth and through South Pole ice by modeling charged and neutral current neutrino-nucleon interactions and neutrino-electron scattering (based on [54]). Neutrino oscillations are neglected. Secondary particles produced in such interactions, e.g. $\mu^- \rightarrow e^- \bar{\nu}_e \nu_\mu$, are recorded. Finally, remaining neutrinos are forced to interact in a cylindrical volume ($r = 1 \text{ km}$, $H = 1.95 \text{ km}$) containing the detector and surrounding ice from which photons can reach an optical module. The probability of each forced reaction is stored for later reweighting of the primary spectrum with the true interaction probability (see Sec. 5.4.3).

Muon Propagation

All secondary muons, assumed collinear with parent neutrinos, are passed to the muon propagation software *Muon Monte Carlo* (MMC) which simulates their stochastic energy loss (see Sec. 4.3 and [68]), treated in discrete steps for $E_\mu > 0.5 \text{ GeV}$ and continuously for $E_\mu < 0.5 \text{ GeV}$.

Photon Propagation

Relativistic muons emit hundreds of photons per centimeter - propagating each photon individually would make simulation impractically slow. Therefore, photon propagation is modeled separately using a one-dimensional (depth-dependent) ice model which accounts for absorption and scattering [47]. The resulting photon distributions are stored in look-up tables. For a light source at a given depth with a given direction, these *photonics tables* contain the mean number of photons arriving at each optical module. The tables used in this analysis had a spacial (angular) resolution for the sources of 40 m (10°).

Detector Simulation

Photons reaching an optical module are processed by *PMT-simulator* which models the photomultiplier response and *DOM simulator* which simulates the subsequent analog to digital conversion in the modules, i.e. the generation of waveforms. A trigger simulation (*trigger-sim*) mimics the response of the IceCube trigger system and sets off the event builder which in simulation is identical to the software running at the South Pole. From this point down the filter chain, all processing is performed exactly as on observational data (see Table 5.2).

5.4.2 Properties of Simulated Signal

For the simulation of SN 2008D, a total of 16,100,000 primary neutrinos was produced in 161 jobs (files) with 100,000 primary neutrinos each. This led to about 2,500 events per file at level 1 and 1,600 events at level 3 or a total of 263,000 level 3 events. Particular care was taken to assure that the simulated signal was processed in an identical manner to experimental data from 2007/2008, i.e. according to the processing levels described in Table 5.2.

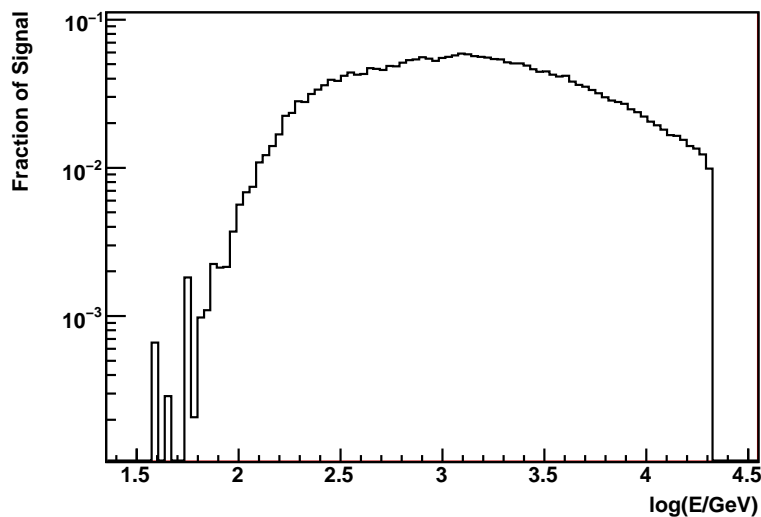


Figure 5.9: Normalized spectrum of primary (true) energies of the simulated signal events at level 3. The reader is invited to compare this with the source spectrum shown in Fig. 3.3, left. As the distribution shows, signal events with primary energies above a few hundred TeV contribute the most events to the expected signal.

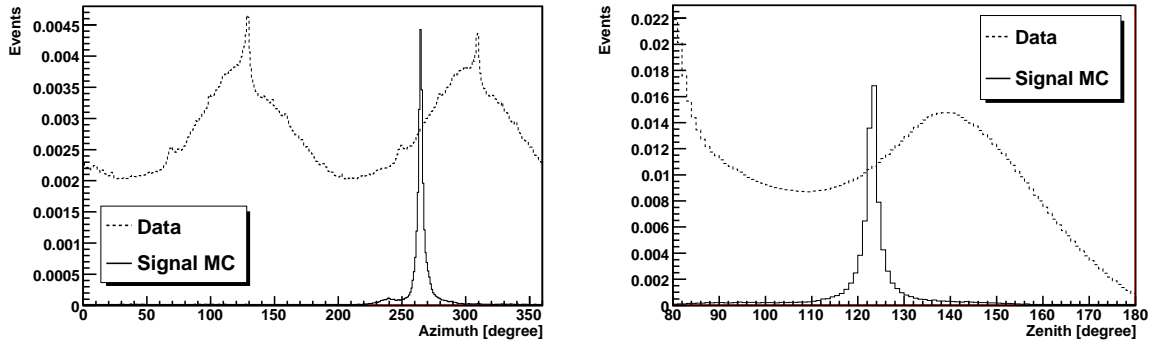


Figure 5.10: Distribution of reconstructed directions for 275-day background sample and simulated signal in detector coordinates, projected onto azimuth (top) and zenith (bottom). Data was normalized, signal was scaled for best illustration. Due to its geometry, IceCube 22 has certain “preferred” directions in azimuth. This can be seen in bumps at $\sim 130^\circ$ and $\sim 310^\circ$ and by the apparent symmetry under $\phi \rightarrow \phi + 180^\circ$ corresponding to opposite tracks. The zenith distribution has a maximum for slightly downgoing tracks ($\sim 80^\circ$) and falls to 0 due to the absorption of muons by the Earth. The increase at $\theta \sim 140^\circ$ is a geometrical effect: Looking through the detector horizontally $\theta = 90^\circ$ it appears thin, i.e. has a small sensitivity. As θ increases, muons travel an increasing length inside the detector and are more likely to be detected.

5.4.3 Signal Expectation

Simply put, the result of the highly complex detector simulation is a single number for each event, the so called *OneWeight* W_i , which quantifies how many units of detected flux a unit of source flux corresponds to for a given energy and direction. Therefore, calculating an event prediction for a given spectrum amounts to summing up these weights multiplied with the source flux for all events passing a certain cut level and then normalizing the sum to the number of generated events³:

$$N_{sim} = \sum_{i=1}^{N_{passing}} W_i \Phi(E_{\nu,i}, \theta_i, \phi_i) / N_{generated} \quad (5.16)$$

was

The signal expectation thus calculated for SN 2008D is **0.37** events at level 3 and **0.26** at level 4 - on the condition that the jet is pointing towards Earth. This number is proportional to the jet energy of the supernova and related to the power law index of the proton spectrum and the cooling break energies in a more complex way.

5.5 Background Simulation

5.5.1 Atmospheric Muons

For the simulation of downgoing atmospheric muons, the *CORSIKA* air shower simulation software is used. It generates primary cosmic ray particles of masses up to iron according to

³A technical note: In the simulation for this analysis, primaries were generated only within a small solid angle $\Delta\Omega$ which enters multiplicative into the weights W_i . Therefore, the weights W_i were divided by $\Delta\Omega$ and the point source flux Φ was spread over 4π to obtain the correct results.

the *polygonato* (multi-knee) spectral model [53] and simulates their propagation through the atmosphere. When an interaction occurs, the resulting particle shower is simulated and all secondary muons are passed on to the muon propagation module MMC. One event, triggered by a *single* primary particle, can contain a large number of muons and several of them can reach the detector in coincidence. From this point on, background simulation and processing follow the same procedure as described in Sec. 5.4.1 for signal. For this analysis, no specific atmospheric muon simulations were conducted. Instead standard CORSIKA datasets commonly used within the IceCube collaboration were used, primarily to assure that simulation accurately models experimental data. So called *coincident* CORSIKA datasets - each event comprises a *pair* of primary cosmic ray particles - were included, which significantly improved the agreement of experimental and simulated data. A detailed data-Monte Carlo comparison can be found in Appendix A.3.

5.5.2 Atmospheric Neutrinos

Since neutrinos produced by cosmic rays in the atmosphere are indistinguishable from cosmic neutrinos, they are simulated identically as discussed in Sec. 5.4.1. Primary neutrinos are, however, distributed over the full sky and weighted with the Honda (Naumov) model spectrum for conventional (prompt) atmospheric neutrinos [51] ([52]). Again, existing simulation datasets available to the collaboration were utilized.

5.5.3 Expected Irreducible Background

The predicted rate of atmospheric neutrinos was computed using Eq. 5.16 to sum the weights of all events in a standard atmospheric neutrino simulation dataset. For a 10° signal region around the position of SN 2008D (level 4), the calculated rate was 1.06×10^{-5} Hz. Since the total background rate at level 4 is 2.5×10^{-2} Hz, a pure neutrino sample is roughly reached at a cut efficiency of around 4.2×10^{-4} .

Level	Signal events	Atmospheric ν rate [Hz]	Atmospheric μ rate [Hz]	Data rate [Hz]
Level 1/2	0.77	0.0019	—	~ 25
Level 3	0.38	0.0010	2.7	~ 3.1
Level 4	0.26	1.06×10^{-5}	0.0023	~ 0.0025

Table 5.3: Predicted and measured event rates or numbers at various filtering levels. Note that for atmospheric muon predictions, both simple and coincident CORSIKA datasets. For these, level 1 rates were not provided in the dataset information. The discrepancy of the CORSIKA prediction of 2.7 and the observed event rate of 3.1 at level 3 could not be resolved within the scope of this analysis and appears to be a normalization issue given the excellent qualitative agreement of data and simulation (see Appendix A.3).

	Signal	Atmospheric ν 's	Atmospheric μ 's	Data
Generator	neutrino-generator (adapted)	neutrino-generator	CORSIKA	—
Dataset	161 custom files	dataset 1834	single: dataset 1541 (coincident: 1731)	full exp. data
Events				
- generated	1.6×10^7	5.0×10^8	5.5×10^9 (8.5×10^8)	—
- triggered	1.0×10^6	3.0×10^6	2.7×10^8 (9.3×10^6)	1.2×10^{10}
- level 3	2.6×10^5	1.0×10^6	1.1×10^6 (1.1×10^5)	7.5×10^7
- level 4	1.8×10^5	1.2×10^4	7.0×10^3 (9.1×10^2)	6.6×10^5

Table 5.4: Statistics for simulation and experimental data used in this analysis. Note that the number of events in a simulation dataset is no direct indicator for the predicted event rate, since each event has a weight. For event rates, refer to Table 5.3 Also note that the factor 10 greater loss of atmospheric neutrinos compared to signal neutrinos from trigger level to level 4 is due to the “half-sky” cut $\theta > 80^\circ$.

5.6 Search Window

A crucial decision in devising this analysis is the choice of the angular and temporal window in which SN 2008D neutrinos are searched. Taking e.g. 1000 seconds and a 20-degree circle might ensure that no neutrinos from SN2008D are missed, but at the same time reduces their significance by including too many background events. While it is desirable to let an unambiguous optimization algorithm determine the ideal size of the search window, some physical considerations need to be taken into account beforehand.

5.6.1 Temporal Size - Time Window

Unfortunately, the theoretical knowledge of the time profile of neutrino emission in the slow jet scenario is very limited. The choice of time windows for this search was designed to include the few available theoretical constraints and to accommodate a wide range of plausible time scales.

Beginning

Since neutrinos practically do not interact after their production, they are expected to arrive first of all particles associated to internal shock collisions and shock break-out. Since there is no evidence for further acceleration processes after the X-ray peak, neutrinos can be assumed to arrive before or at most in coincidence with the X-ray flash.

Duration

The duration of a search window linearly determines the expected background and should therefore be kept as short as possible. On the other hand, several choices of time scales can be motivated by physical considerations. Although the slow jet model lacks any quantitative

prediction of time scales, several considerations which are compatible with the model were adopted:

1. **Long-GRB-Analogy** - The scenario of a jetted supernova suggests the analogy with long duration γ -ray bursts for which the existence of jets seems physically imperative. In these events, γ -rays produced by shock accelerated electrons are emitted on time scales of 10 - 100 s possibly accompanied by a prompt neutrino flash of ~ 1000 s duration and preceded by a precursor neutrino burst of 10 - 100 s [23].
2. **Shock breakout** - The observed X-ray emission from SN2008D, attributed to a spherical shock breakout, lasts about 600 s and provides a time scale for the duration of the shock breakout, in which neutrinos are possibly produced as well. Models of neutrino production in the shock breakout predict time scales of ~ 1 hour [41].
3. **Jet Formation** - The formation of jets and their propagation to the surface might take several hours ($\sim 10,000$ s), during which internal shock collisions could produce numerous neutrino bursts. Estimates range from several [44] up to 10 hours [41].

To account for this wide array of predicted time scales, three search windows of different durations were chosen and placed asymmetrically around the time of the X-ray peak:

- **Window 1:** $\Delta t_1 = 100$ s, beginning 30 s before the X-ray peak
- **Window 2:** $\Delta t_2 = 1,000$ s, centered around the X-ray peak
- **Window 3:** $\Delta t_3 = 10,000$ s beginning 9000 s before the X-ray peak

5.6.2 Angular Size - Aperture

The results of signal simulation (Fig. 5.4) suggest using a circular aperture. Its size, given by its opening angle ω is a crucial parameter since it determines the expected ratio of signal to background. The mean angular resolution of the track reconstructions provide a lower limit for the opening angle - in comparison the uncertainty of the astronomical coordinates of SN 2008D is negligible. A defined upper bound is not given - simulation shows that some signal events are reconstructed more than 20° from their true direction, although claiming a correlation of such an event with SN 2008D seems more than questionable. The most compelling argument for limiting the aperture size is the need to include a minimum of background. Fig. 5.12 shows that the included background increases roughly as ω^2 while very little signal is gained by increasing the opening angle beyond 10° . Instead of requiring a priori that a certain fraction of the signal be contained, the opening angle for each time window is used as a free parameter in the optimization of the model discovery factor (Sec. 5.7.5) and chosen according to the highest discovery potential.

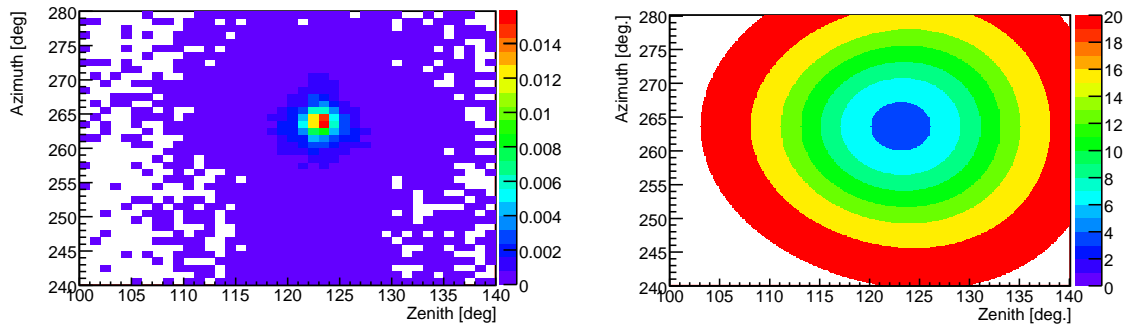


Figure 5.11: Left: Angular distribution of signal (level 3) Right: Different choices of circular apertures in identical scaling for comparison; color scale indicates the opening angle.

Due to the Earth's rotation, SN2008D moves in azimuth with a velocity of 0.0042° per second, i.e. 4.2° during a search of 1000 s duration. This source motion in the fixed detector coordinate system was addressed with an aperture that tracks the position of SN 2008D. Since the sensitivity of IceCube 22 - and thus of the background rate - varies strongly with azimuth, a tracking aperture contains varying background rates. To err on the side of caution, the maximum background rate taken from Fig. 5.12 (right) for each search window was assumed in all calculations.

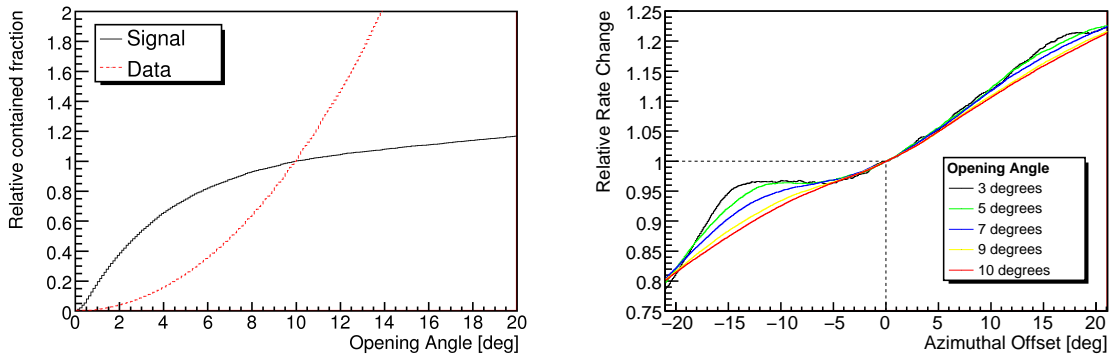


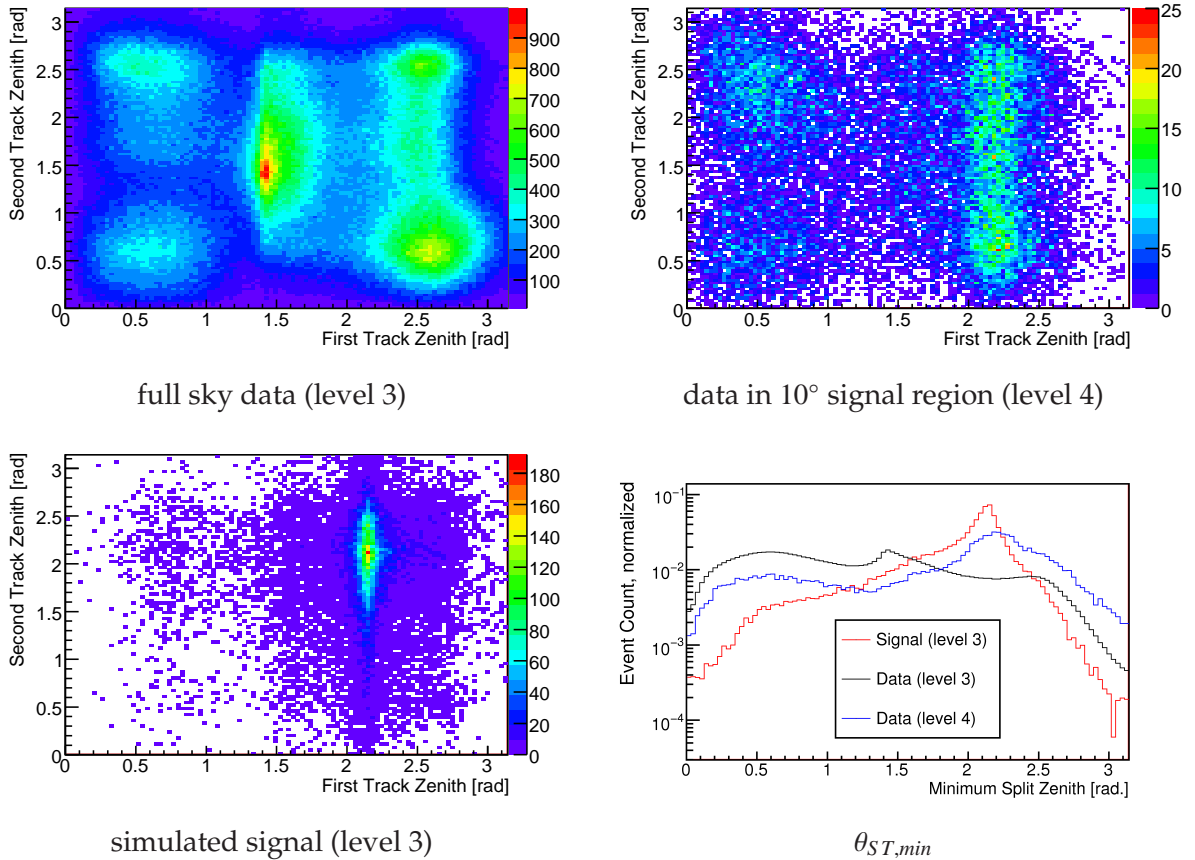
Figure 5.12: Left: Contained signal/data as a function of opening angle, normalized to a 10° aperture in which 0.26 signal events or 69.4% of all signal are contained. Right: Contained background in an aperture moving across the sky due to the Earth's rotation. The range on the x-axis spans 10,000 s. $t = 0$ corresponds to the position of SN 2008D at the beginning of the X-ray flash. Both plots were generated using 657,000 data events and 130,000 signal events.

5.7 Event Selection

5.7.1 Cut Parameters

Finding a needle in a hay stack requires good knowledge of needles and hay. In the case of this analysis, the needle is the neutrino and the straws of hay are atmospheric muons. A first step towards separating the two is to find criteria by which to distinguish them. Around 100 parameters from the different reconstruction algorithms were studied with regard to their aptitude as cut parameters. The parameters finally selected are shown in Figs. 5.13 and 5.14, their definitions are summarized in Table 5.1. All plots are in logarithmic scaling and show one month of data (15.11 days livetime) at level 3 and 34,370 simulated signal events, weighted to the source spectrum.

Figure 5.13: Zeniths of sub-tracks from split track reconstruction, the minimum of both was used as a cut parameter since it provides an excellent veto for coincident downgoing muons appearing as one single upgoing track. The color scales indicate the number of events per bin. The concentration around $(\theta_{ST,1}, \theta_{ST,2}) \approx (80^\circ, 80^\circ)$ for full sky data is due to the large number of almost horizontal tracks of atmospheric origin (compare with Fig. 5.10) and is removed at level 4.



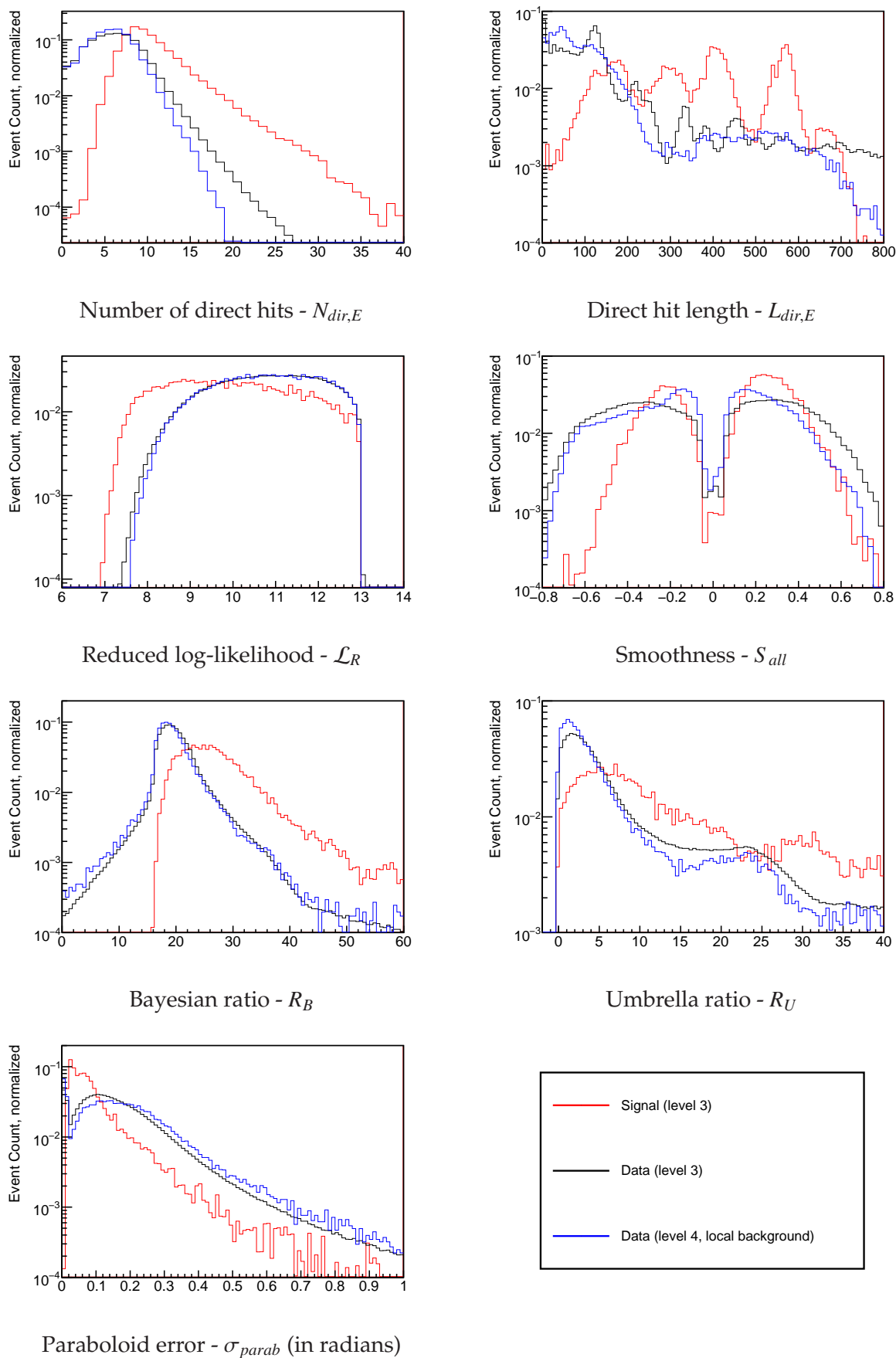


Figure 5.14: Normalized histograms of cut parameters used in this analysis in logarithmic scaling. Shown are: 34,740 simulated and weighted signal events at level 3 (red), 15.11 days of full sky data at level 3 (black), and data within 10° of the SN 2008D coordinates.

5.7.2 Multivariate Classifiers

Having identified a number of reconstruction parameters, which on average take different values for signal/background events (Fig. 5.14), one could naively place a number one-dimensional selection cuts, e.g. $N_{dir,E} > 8$, $\mathcal{L}_R < 10$ etc. If we think of events as points (x_1, \dots, x_N) in a N -dimensional space, where N is the number of cut parameters, signal events should cluster in one region and background events in another. A set of N one-dimensional cuts can be represented by a surface which divides the space in two. If there is, however, a second (third...) cluster of signal events "behind" the cut surface, i.e. in the background half of the parameter space, its events would be lost. There are a number of strategies to overcome the shortcomings of such simple cuts, collectively called *multivariate classifiers*. A multivariate classifier is a function $f(x_1 \dots x_N)$ of the cut parameters quantifying the signal (background) likeness of an event. As a result, cuts can be placed on a single parameter, the classifier value, with efficiencies generally exceeding those of manually selected cuts. To construct a multivariate classifier, one might for example populate a cut parameter space with some events known to be background and others known to be signal, e.g. from Monte Carlo simulations. Then, by splitting up the N -dimensional cut parameter space into small hypercubes and counting the number of signal/background events in each of these cells, one can construct a probability density function for signal/background events and use the normalized ratio of the two as a multivariate classifier. Numerous other methods to compute such classifiers exist. Many of them are conveniently implemented in the ROOT library TMVA (Toolkit for MultiVariate data Analysis).

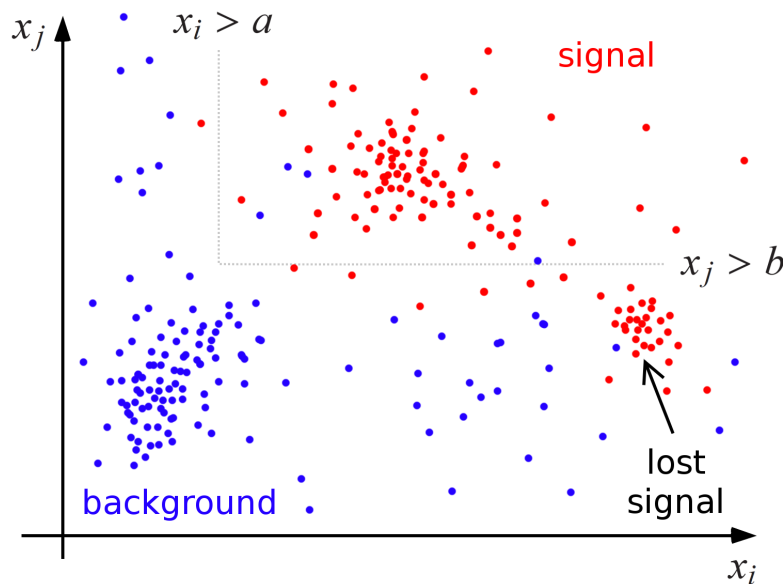


Figure 5.15: Schematic distribution of signal (red dots) and background (blue dots) events in an N -dimensional cut parameter space in the (x_i, x_j) projection. Simple cuts fail to include the cluster of signal event marked with the arrow. In this simple two-dimensional example, it is obvious, that a combination of rectangular cuts would be more effective. In higher dimensions, however, manually finding such cuts becomes extremely difficult.

The TMVA⁴ library offers a number of the most commonly used multivariate classifiers including artificial neural networks, Fisher discriminants, nearest neighbor methods, projective likelihood estimation, support vector machines, and boosted decision trees. Given two samples of events known to be signal/background, TMVA *trains* its classifiers to best separate the two, that is it maximizes a measure of their separation with respect to the classifier parameters.

To identify the classifier best suited for this analysis, all available classifiers in TMVA were trained using a reduced sample of 10,000 data events and 10,000 signal Monte Carlo events⁵. The performances of the various methods were evaluated by comparison of their signal efficiency vs. background rejection graphs shown in Fig. 5.16.

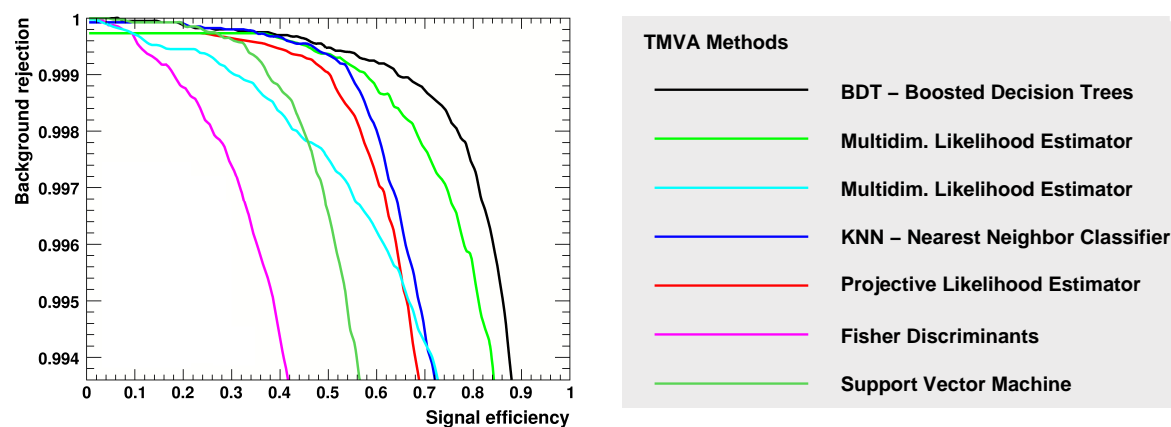


Figure 5.16: Performance of different multivariate classifiers compared on the basis of their background rejection vs. signal efficiency curves. The closer a curve approaches the upper right corner, the higher its performance.

5.7.3 Boosted Decision Trees

After multiple tests of all available classifiers with various sets of cut parameters the *boosted decision tree* (BDT) classifier was chosen because of its performance as well as its transparent and fast algorithm facilitating training and testing with high statistics.

Decision Trees

A *decision tree* is a classification structure through which events are processed, starting from a *root node*, passing several split nodes which guide them into *branches*, and finally arriving at end nodes called *leaves*. At each node, the event is directed to one of two branches based on a binary greater/less decision $x_i \geq a$. Thus at each split level, the number of branches increases by a factor of two. Splitting stops when a stop criterion is reached and each leaf is classified signal or background based on the number of signal/background events it contains. This procedure splits the parameter space into multiple boxes, partially or fully bounded depending on whether a cut parameter appears only once ($x_i > a$) or at several nodes ($x_i > a$ and $x_i < b$).

⁴<http://tmva.sourceforge.net>

⁵TMVA offers the possibility to use the signal weights described in Sec. 5.4.3.

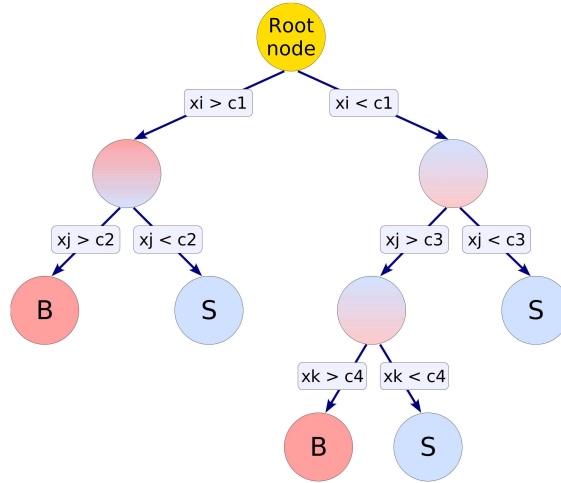


Figure 5.17: Schematic decision tree: Starting at the root node, each event undergoes a series of yes/no decisions based on the value of one of the cut parameters $\{x_1 \dots x_N\}$ and arrives at a certain leaf. Each leaf is classified signal (S) or background (B) based on the number of signal/background events arriving at it.

Training

In the training process, all nodes of the tree are optimized top to bottom to obtain a high signal/background purity in each leaf. At each node, cuts are varied for all parameters in $N_{steps} = 20$ steps until the cut providing the best separation is found. The two resulting subsamples are passed to the subsequent nodes. This splitting stops when a node contains less than twice the minimum number N_{min} of events per leaf. In TMVA, N_{min} depends on the number of training events N_{train} and the number of cut parameters N_{params} via $N_{min} = N_{train}/N_{params}^2/10$. In other words, the maximum number of leaves is limited to $N_{leaves} = 10 N_{params}^2$. The corresponding values chosen for this analysis are listed in Table 5.5.

Decision Forests and Boosting

When several decision trees are combined in a *decision forest*, the number of trees in which an event is channeled into a signal leaf provides a simple classifier for the signal likeness of the event. To improve the classification in the BDT method, this decision forest is grown by re-training the initial tree with a sample in which the signal events previously misdirected into background leaves are given a higher weight - this procedure is referred to as *boosting*. The final BDT classifier value is computed as a weighted mean of the classifications by each tree in the forest.

Parameter	Value	Description
N_{train}	70,000	Number of training events for each, signal and background
N_{params}	8	Number of cut parameters used
N_{leaves}	640	Maximum number of leaves per decision tree
N_{min}	109	Maximum number of events in each leaf
N_{trees}	100	Number of trees in the decision forest

Table 5.5: Parameters of the BDT classifier used in this analysis.

Classifier Values

We shall denote the BDT classifier by $\mathcal{K} : \text{event} \rightarrow \mathbb{R}$, $-1 \leq \mathcal{K} \leq 1$. The classifier is suitable to distinguish between signal and background events assigning values between -1 (background-like) and 1 (signal-like) as shown in Fig. 5.18. Selecting only events with $\mathcal{K} > \mathcal{K}^*$, background is reduced by a factor $\epsilon_b(\mathcal{K}^*)$, the *background efficiency*⁶, while only reducing the signal by a factor $\epsilon_s(\mathcal{K}^*)$, the *signal efficiency*. $\epsilon_b(\mathcal{K}^*)$ and $\epsilon_s(\mathcal{K}^*)$ can be determined by computing \mathcal{K} for samples of signal simulation and background data and sliding a cut \mathcal{K}^* across the distribution of \mathcal{K} -values. Thus, we obtain the signal and background efficiency curves shown in Figs. 5.19 - 5.21. In these plots, an ideal classifier would yield a graph exactly tracing the right and top axes. Note that the curves used for evaluation were generated using background/signal events which were not contained in the training sample.

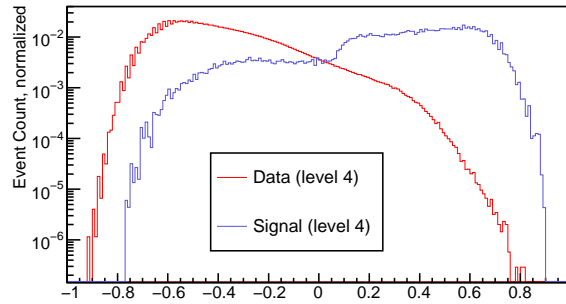


Figure 5.18: Value \mathcal{K} of the BDT classifier for data and signal at level 3.

Testing BDT

With its short computing times, simple accommodation of an arbitrary number of cut parameters, the BDT classifier proved to be very user friendly and allowed extensive testing of the classifier response. To study the stability of the classification results, all relevant training parameters - N_{train} , N_{trees} , N_{params} - were varied over a large range and the resulting signal efficiency vs. background rejection graphs were compared. In addition, training and evaluation were repeated with independent signal and background samples.

To put these results into context, the simple cuts used in the IceCube 22 Point Source Analysis [50] were implemented and applied to the available data and simulation. These cuts, referred to as *PS cuts* in the following, were optimized manually for a half-sky search for clusters of cosmic neutrinos. To pass, an event must fulfill the following conditions⁷:

$$\begin{aligned} \sigma_p < 3^\circ \quad \mathcal{L}_R < 9.5 \quad \theta_{ST,min} > 70^\circ \quad R_U > 15 \quad R_B > 30 \\ (\mathcal{L}_R > 7.8 \quad \wedge \quad N_{dir,C} < 7) \neq \text{true} \\ (\mathcal{L}_R > 8.5 \quad \wedge \quad N_{dir,C} < 8) \neq \text{true} \end{aligned}$$

The PS cuts yielded a signal efficiency of $\epsilon_s^{(PS)} = 0.14$ and a background efficiency of $\epsilon_b^{(PS)} = 6.4 \times 10^{-5}$ with respect to level 4. These values are indicated as a benchmark in the following figures.

⁶The *background rejection* is defined as $\rho_b = 1 - \epsilon_b$

⁷Here, the notation of Table 5.1 is used. Implicitly, these cuts also require that the paraboloid fit and at least one split track fit have succeeded. $N_{dir,C}$ is defined as the number of hits with $-15 \text{ ns} < t_{res} < 75 \text{ ns}$.

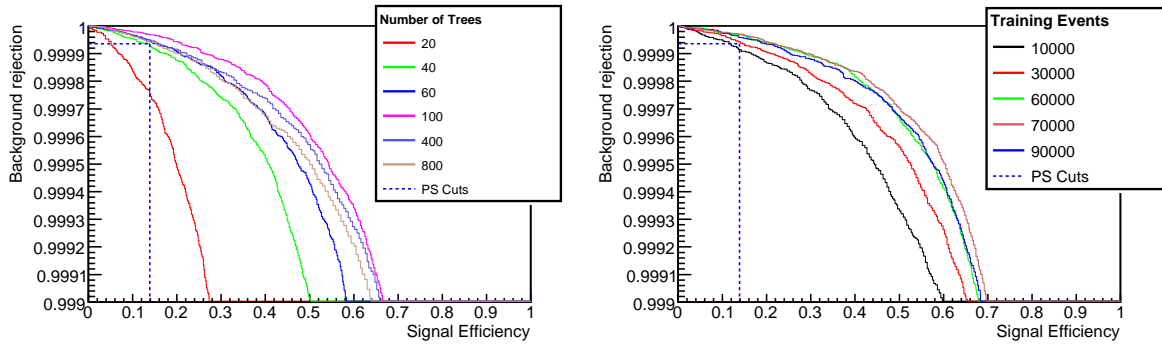


Figure 5.19: Left: BDT performance for differently sized decision forests using 40,000 training events. Right: BDT performance for training samples of various sizes using 100 decision trees.

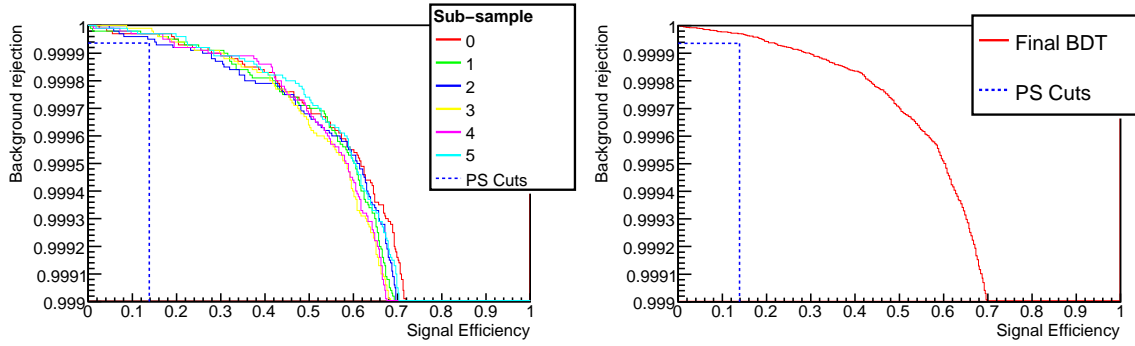
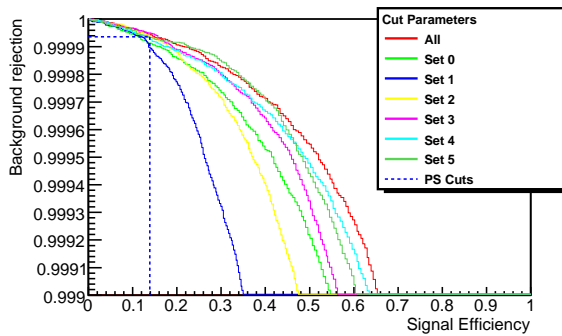


Figure 5.20: Left: Comparison of BDT performances for six independent data samples of 100,000 events each while the signal sample is identical in all cases. The variations are consistent with a purely Poissonian variance \sqrt{N} for each bin. Compare with the figure on the right which uses all 657,000 data events. All graphs were produced using the final settings of $N_{train} = 70,000$ and $N_{trees} = 100$.



	$N_{dir,E}$	$L_{dir,E}$	S_{all}	\mathcal{L}_R	R_U	R_B	$\theta_{ST,min}$	σ_p
All	x	x	x	x	x	x	x	x
Set 0	x	x	x	x	x	x		x
Set 1	x			x			x	x
Set 2	x	x		x			x	x
Set 3	x	x	x	x			x	x
Set 4	x	x	x	x		x	x	x
Set 5	x	x	x			x	x	x

Figure 5.21: Left: BDT performance for different sets of cut parameters. Right: Sets of cut parameters used to train the classifiers shown on the left. x indicates that a parameter was used. The combinations were chosen to study the effect of excluding certain parameters.

In conclusion, the BDT method proved remarkably stable in its response to variations of the training sample and produced a smoothly distributed classifier. This allowed for a

precise tuning of the cuts which shall be presented in the following.

5.7.4 Model Discovery Factor

Which cut is ideal for this analysis? Rejecting a lot of background increases the significance of a possible discovery, however, in doing this we also reject more and more signal, which makes it less likely to see the signal even if it is there. This problem boils down to the question at which point in the distribution of the BDT values a cut shall be placed. Luckily, a well-defined algorithm exists to find the ideal cut: The optimization of the *model discovery factor* (MDF).

We assume we have measured the number of events n_{obs} in a window around SN 2008D, and that this measurement is the sum of a Poisson distributed background (constant in time) with mean μ_b plus an also Poisson distributed signal with mean μ_s . The mean background is to be understood as a long time average; its value is known precisely from the 275-days of IceCube 22 operation. The signal mean μ_s must be understood as the number of events per supernova that would be measured on average if a large number of identical supernovae were observed; this value was calculated in Sec. 5.4.3.

In a real experiment, cuts are applied and n_{obs} is measured with a known background of μ_b , while μ_s is to be derived from the measurement. For a given n_{obs} and μ_b , a lower limit for the signal expectation μ_s can be calculated with the Feldman&Cousins method [64]. This lower limit $\mu_{s,\ell\ell}$ describes above which value μ_s must lie with a probability of $1 - p$. The probability p (p-value) can be set e.g. at $1 - p = 99.865\%$ which corresponds to a $\delta = 3\sigma$ significance level⁸.

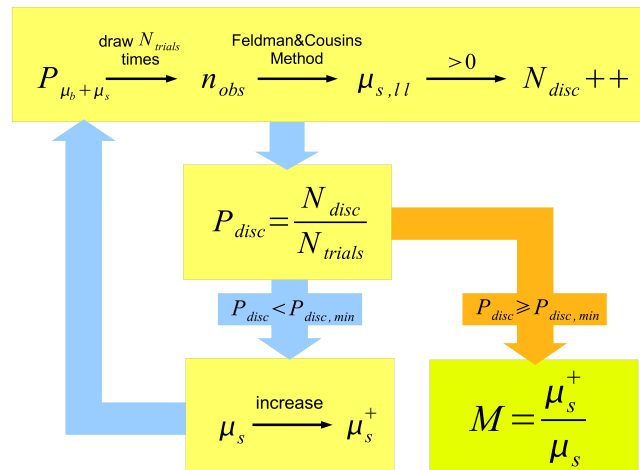


Figure 5.22: Flow diagram of the calculation of a model discovery factor for a given signal expectation μ_s and background expectation μ_b .

Evidently, $\mu_{s,\ell\ell}(n_{obs}, \mu_b | p)$ is equal to 0 when $n_{obs} = 0$ events are observed, i.e. measuring no event is consistent with no signal. However, if the expected background μ_b is

⁸Significance can be stated in terms of the *p-value*, the probability of that the background-only hypothesis is true or alternatively as multiples of the *Gaussian variance* σ in the form $\delta = n\sigma$. The conversion formula is given in Appendix A.1.2. All quoted p-values are understood to be one-sided Gaussian. For details see [9, Ch. 32].

extremely low, measuring $n_{obs} = 1$ events can already give $\mu_{s,\ell\ell} > 0$, which means that the signal is greater than 0 with a probability p and we have made a discovery with a significance of p .

Now let $\mu_{s,0}$ and $\mu_{b,0}$ be the expected mean signal and background contributions at level 4 and $\mu_s = \mu_{s,0} \cdot \epsilon_s(\mathcal{K}^*)$ and $\mu_b = \mu_{b,0} \cdot \epsilon_b(\mathcal{K}^*)$ the same quantities after a BDT cut has been applied. In an imaginary experiment, we can draw random n_{obs} from a Poisson distribution $P_{\mu_s+\mu_b}$ with mean $\mu_s + \mu_b$ to simulate the measurement.

After repeating this N_{trials} times, the number N_{disc} of experiments in which the lower limit for signal is greater than zero $\mu_{s,\ell\ell}(n_{obs}, \mu_b | p) > 0$ is counted and the discovery probability $P_{disc} = N_{disc}/N_{trials}$ is calculated for the chosen cut.

In the last step, a minimum discovery probability $P_{disc,min}$ is fixed at some arbitrary value, e.g. $P_{disc,min} = 50\%$, and an optimization routine determines by which factor M the signal expectation μ_s has to be increased (or decreased) to reach $P_{disc,min}$. This is done by repeating the sampling of $P_{\mu_s+\mu_b}$ while varying μ_s until $P_{disc} = P_{disc,min}$ is reached at $\mu_s^+ = M \cdot \mu_s$. This equation is in fact the definition of the *model discovery factor* (MDF):

$$M(\mathcal{K}^* | p) = \frac{\mu_s^+(\mathcal{K}^*)}{\mu_s(\mathcal{K}^*)} \quad (5.17)$$

where \mathcal{K}^* is the value at which the BDT cut is placed and p is the p-value of the significance level required for a discovery. The cut with the lowest value of M is the ideal one since it provides the most beneficial combination of a low background expectation and a high probability of detecting a significant signal. In other words M_{min} best combines the adverse requirements of a high sensitivity and a high significance.

5.7.5 Optimization for Discovery

The model discovery factor is not necessarily a function of the BDT cut \mathcal{K}^* only. It can easily be extended to include angular and time window cuts as well.

As discussed in Sec. 5.6.2, angular cuts are parametrized by the opening angle ω of the circular aperture. The signal (background) expectation is multiplied with the fraction $f_s(\omega)$ ($f_b(\omega)$) of signal (background) events contained in the aperture with opening Angle ω . These fractions were determined relative to level 4 ($\omega = 10^\circ$) and are shown in Fig. 5.11.

The duration of the search window Δt determines the background expectation via $\mu_{b,0} = b \cdot \Delta t$ where $b = 0.0025$ Hz is the level 4 background rate. Signal is assumed to be fully contained in any chosen time window. The background and signal expectation can be expressed as $\mu_b = b \cdot \Delta t \cdot \epsilon_b(\mathcal{K}^*) \cdot f_b(\omega)$ and $\mu_s = \mu_{s,0} \cdot \epsilon_s(\mathcal{K}^*) \cdot f_s(\omega)$, respectively. The model factory factor becomes a function of all cut variables and the chosen significance level:

$$M = M(\mathcal{K}^*, \Delta t, \omega; p) \quad (5.18)$$

To find the minimal model discovery factor, M was calculated according to the prescription described in the previous section. Conservatively, the signal (background) expectation for each window was calculated using the corresponding efficiency *minus* (*plus*) its statistical error, $\epsilon_s^{min} = \epsilon_s - \Delta\epsilon_s$ ($\epsilon_b^{max} = \epsilon_b + \Delta\epsilon_b$). Parameters were varied on a lattice spanned by:

$$\begin{aligned} \mathcal{K}^* &= [-0.4, -0.42, -0.44, \dots, 0.9] \\ \omega &= [2^\circ, 3^\circ, 4^\circ, \dots, 10^\circ] \\ \delta &= [3\sigma, 5\sigma, 5.1\sigma] \\ \Delta t &= [10\text{ s}, 50\text{ s}, 100\text{ s}, 1000\text{ s}, 10000\text{ s}] \end{aligned}$$

The additional short time windows were included to study whether a single event could constitute a 5σ discovery on such short time scales. A first coarse sampling of the parameter space was visualized by sets of $M(\mathcal{K}^*)$ -curves for different opening angles ω . The curves were cut-off at cut levels, where the initial discovery probability fell short of $1/N_{trials}$. Fig. 5.23 illustrates how the MDF graphs were interpreted.

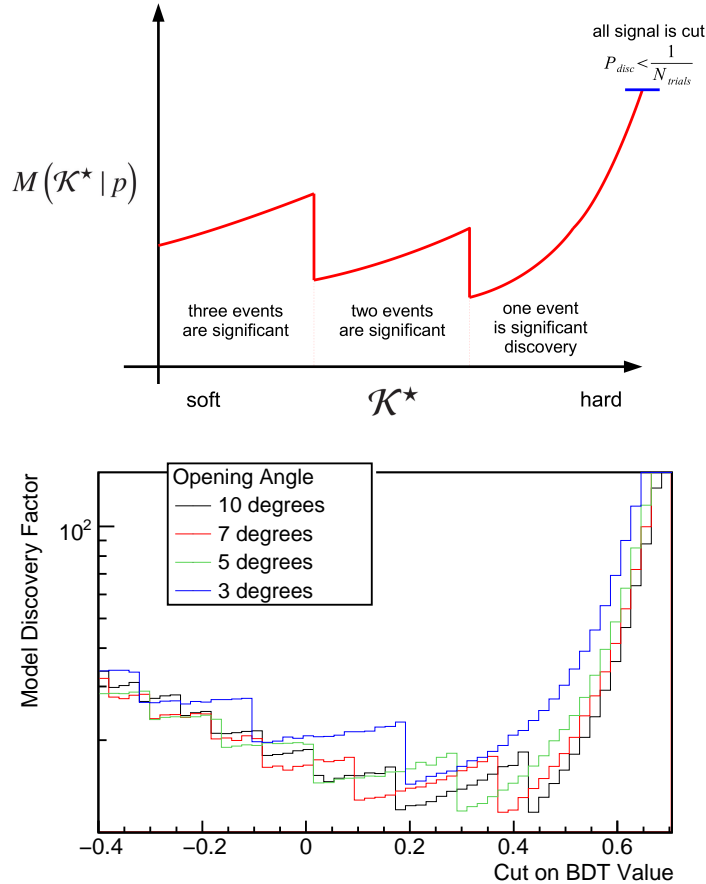
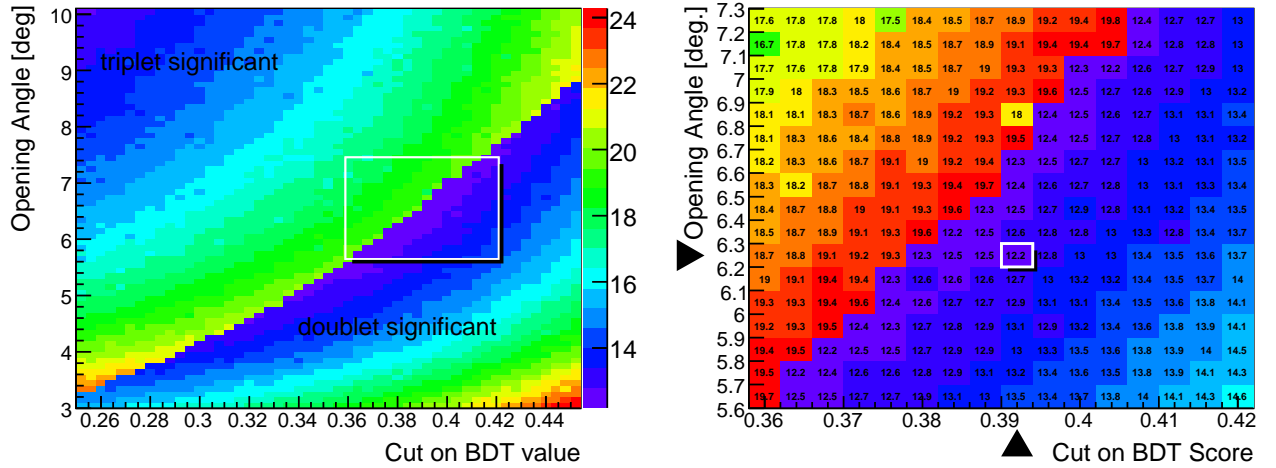
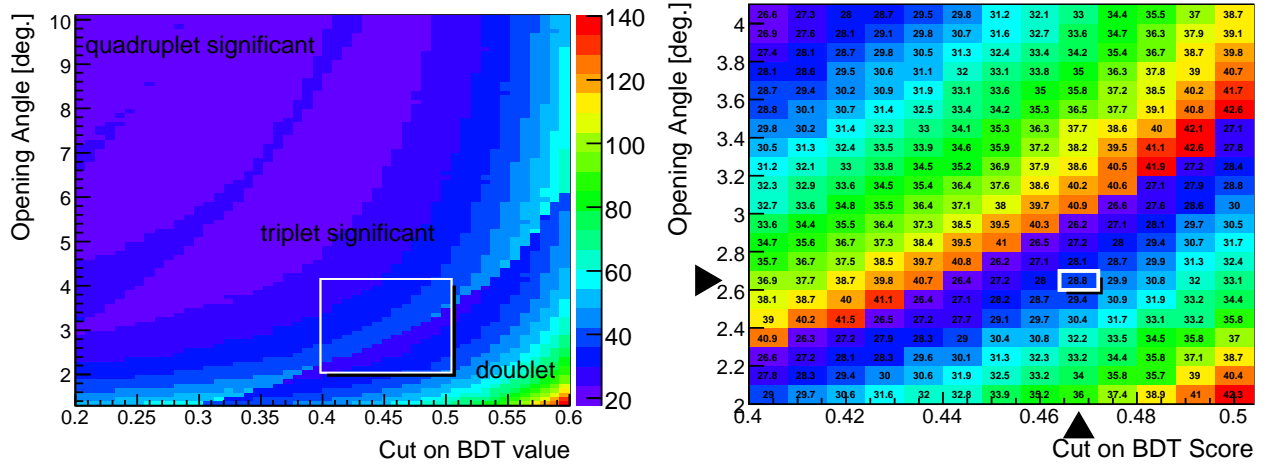


Figure 5.23: Top: Schematic graph of the model discovery factor M as a function of the BDT cut \mathcal{K}^* . **Bottom:** Example of a coarse MDF plot used to identify the minima which were studied in detail. The graphs were calculated for a 100 s time window requiring a significance of 5σ ($p = 2.85 \times 10^{-7}$) for a discovery. The signal expectation in this time window is $\mu_{s,0} = 0.27$, the background expectation is $\mu_{b,0} = 3$ at level 4.

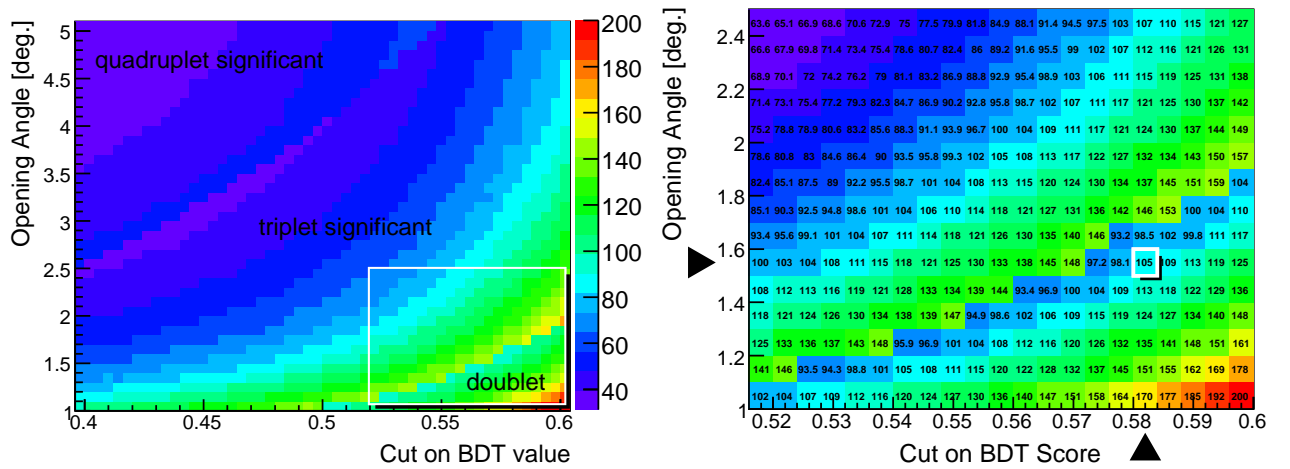
The minima found in these plots were then studied with an increased resolution of $\Delta\omega = 0.1^\circ$ and $\Delta\mathcal{K}^* = 0.002$. The results are shown in Fig. 5.24. To implement the strategy of using three overlapping search windows, the opening angle and BDT cut yielding a minimal model discovery factor were first determined separately for each time window. Since the introduction of additional search window increases the chance of picking up a random background fluctuation, the significance of a possible detection with three search windows decreases compared to the use of a single window. Therefore an increased significance of 5.1σ was required for each individual search window. The final significances were later determined in a Monte Carlo study presented in Sec. 5.8.



100 s time window, 5.1σ significance required



1,000 s time window, 5.1σ significance



10,000 s time window, 5.1σ significance

Figure 5.24: Values of the model discovery factor as a function of aperture and BDT cut. Color scale indicates MDF value. In all plots, the significance required for a discovery is 5.1σ . The boxed region in each plot on the left is zoomed in in the corresponding plot on the right where the selected final cuts are marked by arrows. These cuts were placed manually with the requirement that a neutrino doublet would constitute a discovery.

5.7.6 Final Cuts

As indicated by the arrows in Fig. 5.24, the following cuts were chosen for the three different time windows:

		Window 1	Window 2	Window 3
Duration	Δt	100 s	1,000 s	10,000 s
Aperture	ω	6.2°	2.6°	1.5°
BDT cut	\mathcal{K}^*	0.39	0.464	0.58
Efficiencies relative to level 4				
Angular cut				
signal	$f_s(\omega)$	0.83	0.47	0.28
background	$f_b(\omega)$	0.38	0.07	0.02
BDT cut				
signal	$\epsilon_s(\mathcal{K}^*)$	0.50	0.48	0.22
background	$\epsilon_b(\mathcal{K}^*)$	3.2×10^{-4}	2.8×10^{-3}	7.5×10^{-5}
Angle + BDT cut				
signal	$\epsilon_s(\mathcal{K}^*) \cdot f_s(\omega)$	0.42	0.23	0.06
background	$\epsilon_b(\mathcal{K}^*) \cdot f_b(\omega)$	1.2×10^{-4}	1.8×10^{-3}	1.5×10^{-6}
MDF	M	12.2	28.8	106
Optimized for		5.1σ	5.1σ	5.1σ
Discovery with		doublet	doublet	doublet

Table 5.6: Final search windows and corresponding cuts.

In all three windows, taken separately, a neutrino doublet would have a significance of 5.1σ . The resulting significances for the combined search shall be discussed in the following section.

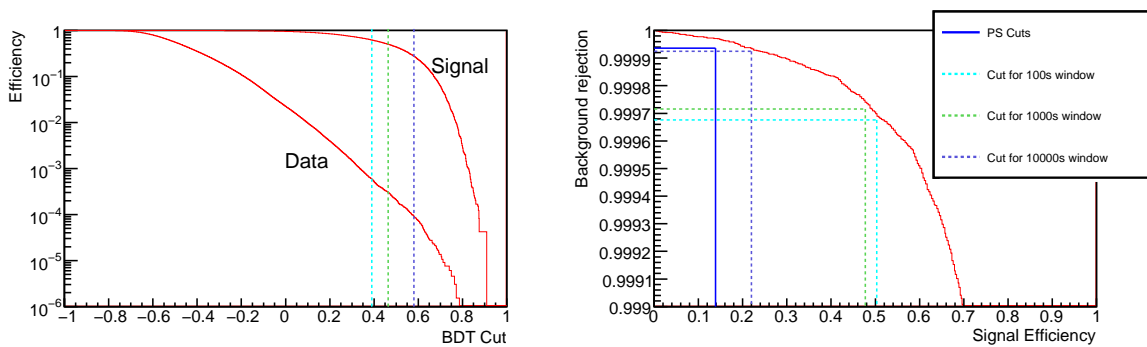


Figure 5.25: Signal and background efficiencies $\epsilon_s(\mathcal{K}^*)$ and $\epsilon_b(\mathcal{K}^*)$ for the BDT classifier settings. **Right:** Signal efficiency vs. background rejection with final cuts indicated by dashed lines.

5.8 Significance

5.8.1 Monte Carlo Study

In an experiment using two search windows with different cuts, durations, and apertures, it is not immediately clear what the significance of detecting for example two events in window 1 and one event in window 2 are. To answer this question, a Monte Carlo study was conducted. The experiment was simulated with a background-only hypothesis: Observations denoted by (N_1, N_2) were drawn from two background Poissonians P_{μ_1} and P_{μ_2} . For window i the duration is represented by Δt_i , the aperture by ω_i , and the contained background fraction by $f_b(\omega_i)$; the cut placed on events inside the window is denoted by \mathcal{K}_i^* and the corresponding background efficiency by $\epsilon_b(\mathcal{K}_i^*)$. For both windows, the background rate before cuts shall be b . With this notation, the means of the two Poisson distribution describing the background in window 1 and 2 are given by:

$$\mu_b^{(1)} = b \Delta t_1 \epsilon_b(\mathcal{K}_1^*) f_b(\omega_1) \quad (5.19)$$

$$\mu_b^{(2)} = b (\Delta t_2 - \Delta t_1) \epsilon_b(\mathcal{K}_2^*) f_b(\omega_2) \quad (5.20)$$

The overlap of the two time windows is taken into account as follows: In every trial, each of the N_1 events drawn in the first window was looped over and added to N_2 with a probability given by the ratio of both windows' efficiencies. Assuming that the second, longer window, has tighter cuts, i.e. $\epsilon_b(\mathcal{K}_1^*) f_b(\omega_1) > \epsilon_b(\mathcal{K}_2^*) f_b(\omega_2)$, the probability of an event detected in window 2 to be found in window 1 as well is given by:

$$P_{1 \text{ in } 2} = \frac{\epsilon_b(\mathcal{K}_2^*) f_b(\omega_2)}{\epsilon_b(\mathcal{K}_1^*) f_b(\omega_1)} \quad (5.21)$$

Both background Poissonians were randomly sampled n_{trials} times and the number of occurrences $n(N_1, N_2)$ was counted for each observation (N_1, N_2) and then normalized by the number of trials n_{trials} :

$$P(N_1, N_2) = \frac{n(N_1, N_2)}{n_{\text{trials}}} \quad (5.22)$$

After ordering these probabilities, the p-value for each observation was computed using the prescription:

$$p(N_1, N_2) = \sum_{\substack{N'_1, N'_2 \\ P(N'_1, N'_2) \leq P(N_1, N_2)}}^{\infty} P(N'_1, N'_2) \quad (5.23)$$

In words, the p-value for an observation (N_1, N_2) is the sum of its own probability and those of all *less likely* observations, that is the "unlikeliness" of the observation under a background-only hypothesis. Conversely, $1 - p$ is the probability of the observation being caused by an additional source. p-values were converted into significances for a one-sided Gaussian (expressed in multiples of σ , $\delta = n \sigma$) by inverting the relation $p = [1 - \text{erf}(n/\sqrt{2})]/2$.

This procedure - described here for two search windows - was generalized to three windows in a straight-forward manner.

5.8.2 Significances of Possible Observations

Significances were computed as described above using a compiled C++ macro under ROOT. For 10^{10} trials, ~ 30 minutes of CPU time were needed. As in the MDF optimization, the

background expectation for each window was calculated using the corresponding efficiency *plus* its statistical error. Moreover, for each time window the maximum local background contained in the aperture as it tracks SN 2008D is assumed. The used values are $\mu_b^{(1)} = 3.67 \times 10^{-4}$, $\mu_b^{(2)} = 5.52 \times 10^{-4}$, and $\mu_b^{(3)} = 5.55 \times 10^{-4}$. The probability of an event in window 1 to be observed in window 2 was 15%; for the same event to also appear in window 3, the probability is 1.3%, and for an event seen in window 2 (not in window 1) to pass the cuts of window 3, the chance is 8.8%. Table 5.7 lists the significances obtained with 10^{10} trials.

	N_1	N_2	N_3	δ/σ
	0	2	1	6.361
$> 5\sigma$	2	0	0	5.336
	0	2	0	5.112
	1	1	0	4.989
$> 4\sigma$	0	0	2	4.909
	1	0	1	4.848
	0	1	1	4.778
	1	0	0	3.422
$> 3\sigma$	0	1	0	3.163
	0	0	1	3.004

Table 5.7: Significances of possible observations in multiples of one-sided Gaussian σ . N_i denotes the number of events detected in window i . Any single event would provide evidence for a neutrino emission by SN 2008D, any two events within 1000 s or less of the X-ray observation would constitute a discovery.

For the interested reader, a more detailed listing is provided in Appendix A.2 in which scenarios are further subdivided. For example, for the observation $(N_1, N_2, N_3) = (1, 1, 0)$, cases where a single event appears in two windows can be distinguished from those in which two separate events are detected in each window. Since in IceCube, each event is given a unique event ID, such a distinction *could* have been implemented experimentally, if several neutrinos had been detected.

5.9 Error Analysis

Event expectations and limits quoted in the following sections were derived under a maximum-background, minimum-signal hypothesis. The signal and background expectations for the final search windows are given by:

$$\mu_s^{(i)} = \mu_{s,0} \epsilon_s(\mathcal{K}_i^*) f_s(\omega_i) \quad (5.24)$$

$$\mu_b^{(i)} = \underbrace{\mu_{b,0}}_{b \Delta t_i} \epsilon_b(\mathcal{K}_i^*) f_b(\omega_i) \quad (5.25)$$

$$(5.26)$$

With the exception of Δt_i , the quantities on the right hand side shall be examined with respect to their uncertainty. Two contributions, $f(\omega)$ and $\epsilon(\mathcal{K}^*)$ shall be discussed in greater detail, because of their particular importance to this analysis. The discussion of the remain-

ing uncertainties of signal simulation ($\mu_{s,0}$) and background measurement ($\mu_{b,0}$) builds on the results of other studies and is summarized shall be kept brief.

5.9.1 Direction Reconstruction

The fractions $f_s(\omega)$ and $f_b(\omega)$ of contained signal (background) in an aperture with opening angle ω shown in Fig. 5.12 were calculated using $\Delta\mu_s/\mu_s$ samples of $N \gtrsim 100,000$ events and therefore have a negligible uncertainty:

$$\Delta f(\omega)/f = 1/\sqrt{N(\omega)} \approx 0.3\% \quad (5.27)$$

Still, angular uncertainty shall be examined more closely for another reason: If neutrinos *are* detected in coincidence with SN 2008D, the quality of their directional reconstruction is essential to the validity of the claim that they must be attributed to SN 2008D. As shown here, the standard estimator for angular uncertainty used in IceCube, the paraboloid error σ_p cannot be used here and the deviation is much higher (4.7°) than generally quoted for IceCube 22 (1.5° , [50]).

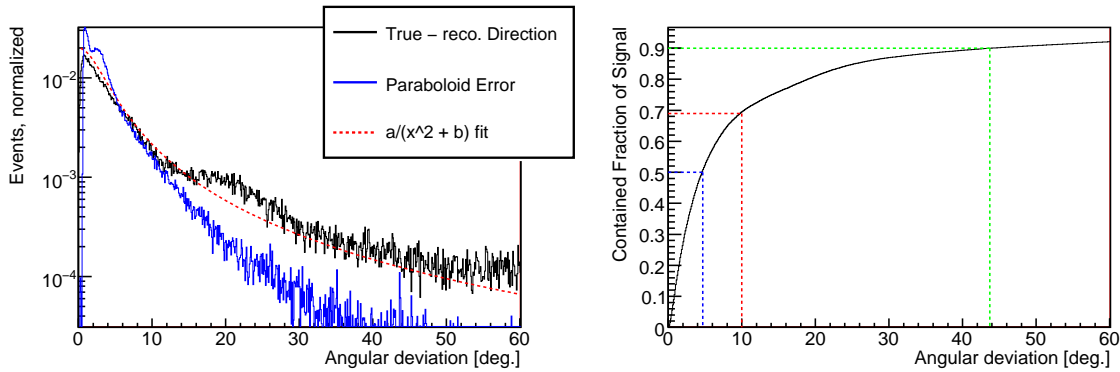


Figure 5.26: **Left:** Histogram of the angle $\angle(\vec{n}_{true}, \vec{n}_{reco})$ between the true and the reconstructed direction of simulated signal events. A fit with $y(x) = 0.24/(x^2 + 12)$ describes the distribution fairly well. Also shown is the distribution of σ_p , the paraboloid error which underestimates the angular uncertainty. **Right:** Cumulative distribution $\angle(\vec{n}_{true}, \vec{n}_{reco})$. Lines from left to right mark: 50% of signal contained within 4.7° , 69% within 10° , and 90% within 43.7° .

Therefore all background rates for a given direction as well as the signal prediction of 0.26 events for SN 2008D were determined by averaging over a 10° degree region around the respective direction. As another result of the large angular uncertainty, the fraction of signal lost through the angular cuts is significant - 62% / 84% / 90% at level 4 with respect to level 1 for window 1/2/3.

In the case of a neutrino detection, the local background (see Fig. 5.12) for the detected direction can be used to derive signal limits. For the calculation of an upper limit one has to use an average background over the respective time window. To be conservative, the limits quoted in Sec. 6.0.6 were computed based on the assumption of the maximum background expected while tracking the supernova for the entire duration of the search. This resulted in a 0.5% / 3% / 25% higher background expectation in window 1/2/3.

5.9.2 Cut Efficiencies

To evaluate, whether the BDT cuts introduce a relevant systematic uncertainty, we compare the variations of the classification with purely statistical fluctuations. Background (signal) efficiencies were derived from a limited data sample of $N_b = 657,000$ ($N_s = 264,000$) events using:

$$\epsilon_{b/s}(\mathcal{K}^*) = \frac{N'_{b/s}(\mathcal{K}^*)}{N_{b/s}} \quad (5.28)$$

where $N'_{b/s}(\mathcal{K}^*)$ is the number of background (signal) events pass a cut at \mathcal{K}^* . The uncertainty due to statistical fluctuations $\Delta N'_{b/s} = \sqrt{N'_{b/s}}$ and $\Delta N_{b/s} = \sqrt{N_{b/s}}$ are easily calculated ⁹:

$$\Delta \epsilon_{b/s} = \frac{1}{N_{b/s}} \Delta N'_{b/s} - \frac{N'_{b/s}}{N_{b/s}^2} \Delta N_{b/s} = \begin{cases} \frac{1}{\sqrt{N_{b/s}}} \sqrt{\epsilon_{b/s}} & \text{high cut levels} \\ \frac{1}{\sqrt{N_{b/s}}} (\sqrt{\epsilon_{b/s}} - \epsilon_{b/s}) & \text{low cut levels} \end{cases} \quad (5.29)$$

This calculation assumes that both fluctuations are uncorrelated which is roughly true at high cut levels, but becomes more and more inaccurate at low cut levels, where $N \approx N'$. Dropping the $-\epsilon_{b/s}$ term is justified at high cut efficiencies, where $N' \ll N$. At low efficiencies, the second term dominates, although correlation apparently reduces its effect, as Figs. 5.27 and 5.28 illustrate.

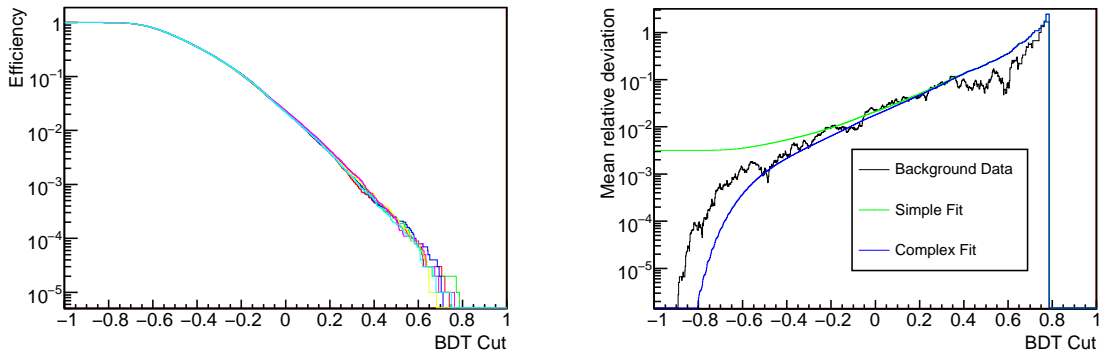


Figure 5.27: Left: Background efficiency of BDT cut, evaluated with 6 independent data samples of 100,000 events. Right: Mean fluctuations of ϵ_b derived from the plot on the left; simple fit (top in Eq. 5.29) and complex fit (bottom in Eq. 5.29).

⁹Although N_b and N_s are fixed, $\Delta N_{b/s} = \sqrt{N_{b/s}}$ can be interpreted as describing fluctuations in the *composition* of the samples.

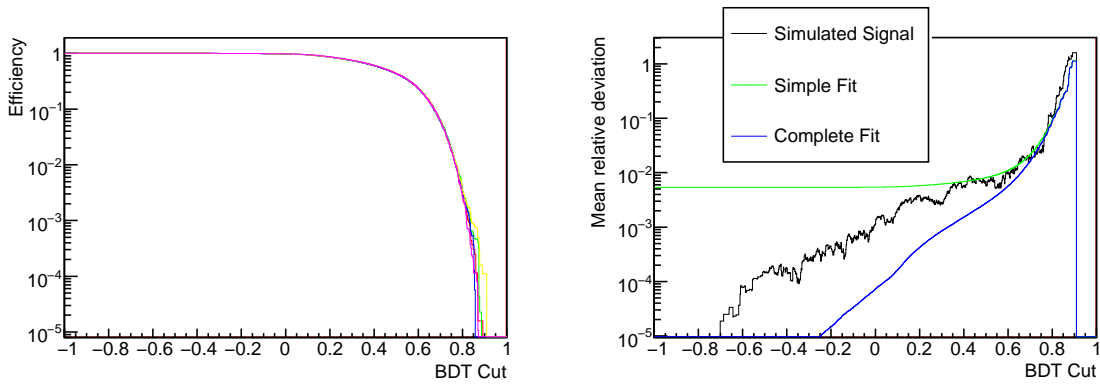


Figure 5.28: Left: Signal efficiency of BDT cut, evaluated with 5 independent data samples of 35,000 events. Right: Mean relative fluctuations of ϵ_s derived from the plot on the left; simple fit (top in Eq. 5.29) and complex fit (bottom in Eq. 5.29).

Overall, the observed fluctuations in the classification of different data samples match the predicted behavior. The figures show that the variations are consistent with purely statistical fluctuations and that the uncertainty in the response of the BDT classifier is negligible.

For the cuts applied in this analysis ($\mathcal{K}^* \approx 0.4 - 0.6$), the relative uncertainty of the cut efficiency was below 1% for signal and 10% for background. As mentioned above, background (signal) efficiencies were increased (decreased) by their statistical error to $\epsilon_b^{max} = \epsilon_b + \Delta\epsilon_b$ ($\epsilon_s^{min} = \epsilon_s - \Delta\epsilon_s$) when calculating model discovery factors and significances. The increased background efficiency was also used to calculate the upper limits given in Sec. 6.0.6.

5.9.3 Background Measurement

The expected background rate is based on a long-term measurement rather than simulation and is therefore free of systematic uncertainties. Like any counting experiment, however, the measurement of the background rate is subject to statistical fluctuations. In the case of the IceCube 22 measurement with a total livetime $\tau_{tot} = 275.72$ d and $N_4 = 657,000$ level 4 events, the uncertainty in the mean level 4 background rate \bar{b} is negligible:

$$\bar{b} = \frac{N_4}{\tau_{tot}} = 2.76 \times 10^{-2} \text{ Hz} \quad \frac{\Delta\bar{b}}{\bar{b}} = \frac{1}{\sqrt{N_4}} = 0.1 \% \quad (5.30)$$

The seasonal variations (see Fig. 5.2) of the background rate with an amplitude of roughly ± 0.1 were treated as a systematic correction rather than an uncertainty. Since this analysis was performed on data from January, a background rate of $b = 1.1 \bar{b} = 3.0 \times 10^{-2}$ Hz was assumed instead of the all-year average rate \bar{b} .

5.9.4 Signal Simulation

Signal simulation is known to diverge from measured event rates from the comparison of CORSIKA simulation data with experimental data (see e.g. Appendix A.3). For astrophysical sources where the true signal has not yet been measured, a predicted event number suffers from a number of difficulties in modeling the complex Earth-ice-detector system. The most important contributions to this systematic uncertainty in the signal expectation $\mu_{s,0}$ have been roughly constrained and are listed in Table 5.8.

Contribution	Estimated uncertainty	Description
Earth Density	$\pm 5\%$	Uncertainties in the density profile of the Earth, particularly the rock density just below the detector linearly affect modeled event rates [67]
Neutrino Cross Sections	$\pm 2\%$	insufficient knowledge of the parton functions of nuclei, leading to a $\sim 2\%$ uncertainty in the νN cross sections used in simulation at $E_\nu < 10^5$ GeV; linearly affects event rates [56]
Muon Propagation	$\pm 3\%$	how many secondary muon arrive at the detector depends on their average energy loss which is a stochastic process modeled imperfectly [68]
Photon propagation in ice and PMT response	$\pm 15\%$	the ice model used for photon propagation and the assumed quantum efficiencies photomultiplier (measured under laboratory conditions) fail to reproduce long-term integrated photon counts at the modules, corrections which deliver matching rates, lead to variations in event rates $\sim 15\%$ [66]
Reconstruction bias	$\pm 2\%$	Selection cuts applied on real events have a different effect than on simulated events, which causes a bias in predictions; studied for a E^{-3} spectrum and simple cuts on R_B , σ_p , \mathcal{L}_R in [65]

Table 5.8: Summary of significant systematic uncertainties in signal simulation.

Adding these contributions in quadrature, we obtain the total systematic uncertainty of the signal prediction:

$$\sigma_{tot} = \sqrt{\sum_i \sigma_i^2} \simeq 17\% \quad (5.31)$$

Chapter 6

Results

6.0.5 Unblinding

Like all analyses in IceCube, this analysis had to pass a two-stage refereeing process. The method was first scrutinized by referees assigned by the GRB working group and finally vetted in a collaboration-wide unblinding process with two additional referees. This process proved very productive, giving rise to new ideas such as the second and third search window and corroborating results by requiring a variety of tests, e.g. of the BDT classifier. On December 10, 2009, the analysis received authorization to unblind the experimental data from January 9, 2008. The complete unblinding procedure was included in a single C++ script which was vetted by IceCube collaborators.

No events passing cuts were found in any of the search windows. This result is consistent with the predicted discovery probabilities of 10%, 6%, and 2% for windows 1, 2, and 3 which are further diminished by the only 5% chance of the predicted jet pointing towards Earth.

	Window 1 100 s, 6.2°	Window 2 1,000 s, 2.6°	Window 3 10,000 s, 1.6°
Observed Events	0	0	0
Expected Events			
Signal μ_s	0.11	0.058	0.016
Background μ_b	3.67×10^{-4}	5.52×10^{-4}	5.55×10^{-4}

Table 6.1: Summary of the unblinding results and comparison with expectations. The expected event numbers were calculated based on the conservative assumptions discussed in Sec. 5.9.

The best candidate for a signal event with a relatively high signal likeness of $\mathcal{K} = 0.34$ was found at 13:26:13 UT, 6 minutes before the X-ray flash and thus within the 1,000 s search window. The reconstructed direction was offset from the direction of SN 2008D by 1.7°. If the measurement had used window 2 as the only search window with a slightly lower BDT cut at $\mathcal{K}^* = 0.34$, this event would have been classified signal at a confidence level of $\delta = 2.97 \sigma$ (one sided p-value $p = 0.9985$).

6.0.6 Limits on the Slow Jet Model

Under the assumption that the supernova jet was indeed pointing towards Earth, a conditional upper limit on the slow jet model can be derived. Using the Feldman&Cousins method [64], the signal upper limit $\mu_{s,ul}^{(90)}$ for N_i observed events given an expected background of μ_b was calculated separately for each time window for a 90% confidence level. In the absence of more precise theoretical predictions on the time profile of the emission, quoting limits for particular time scales is the only viable way to constrain the slow jet model. Since $N_1 = N_2 = N_3 = 0$ and $\mu_b^{(1)} \approx \mu_b^{(2)} \approx \mu_b^{(3)}$, the upper limits were identical to the fourth significant digit:

$$\mu_{s,ul}^{(90)} = 2.44 \quad (6.1)$$

The upper limits on the slow jet flux derived from this, diverge due to the different signal expectations $\mu_s^{(i)}$ for each search window:

$$\Phi_{\nu,ul}^{(90)} = \Phi_{\nu} \cdot \frac{\mu_{s,ul}^{(90)}}{\mu_s^{(i)}} = \Phi_{\nu} \cdot \begin{cases} 24.4 \pm 3.5 & \text{for 100 s window} \\ 40.6 \pm 6.7 & \text{for 1,000 s window} \\ 122 \pm 24 & \text{for 10,000 s window} \end{cases} \quad (6.2)$$

Each limit is only valid under the assumption that the entire neutrino signal is contained in the corresponding time window. In other words, Eq. 6.2 gives upper limits for each of the given time scales. The values are derived under the conservative signal and background expectations listed in Table 6.1, the quoted errors account for the systematic uncertainties $\Delta\mu_s/\mu_s = 16\%$ of the signal expectations.

The result of this analysis can be summed up in one sentence: If the slow jet model is the correct scenario for SN 2008D, the predicted jet *was* pointing in the direction of the Earth, and the neutrino emission lasted no more than 100 (1,000, 10,000) seconds, the supernova *must* have emitted at most 24 (41, 122) times more neutrinos or have occurred 5 (7, 12) times closer than assumed. Otherwise, this analysis would have detected it with a probability of 90%.

For completeness, the constraints on Φ_{ν} shall also be quoted at a reference energy of $E_{\nu} = 100 \text{ GeV}$ and for each emission time scale τ_e in a more convenient form:

$$\left[\frac{\Phi_{\nu,ul}^{(90)}(100 \text{ GeV})}{\text{GeV}^{-1} \text{cm}^{-2}} \right] = \left[\frac{d}{10 \text{ Mpc}} \right]^2 \times \begin{cases} 3.5 \times 10^{-2} \pm 14\% & \text{for } \tau_e = 100 \text{ s} \\ 5.8 \times 10^{-2} \pm 17\% & \text{for } \tau_e = 1,000 \text{ s} \\ 1.7 \times 10^{-1} \pm 20\% & \text{for } \tau_e = 10,000 \text{ s} \end{cases} \quad (6.3)$$

Finally, to derive simple constraints on the main parameters of the model, the kinetic energy release E_j and the Lorentz factor of the jet Γ_b , we assume incorrectly that the shape of the slow jet neutrino flux Φ_{ν} (Eq. 3.8) is independent of E_j and Γ_b so that Φ_{ν} is simply proportional to the product $E_j \Gamma^2$. This assumption is conservative, since the break energies in the slow jet spectrum increase with Γ_b which places more neutrinos at higher energies where IceCube is more sensitive. The correct parameter dependencies are found in Table 3.5.2. With this simplification, Eq. 6.2 becomes:

$$\left[\frac{\Gamma_b}{\Gamma_3} \right]^2 \left[\frac{E_j}{E_{51.5}} \right] < \begin{cases} 24.4 \pm 3.5 & \text{for } \tau_e = 100 \text{ s} \\ 40.6 \pm 6.7 & \text{for } \tau_e = 1,000 \text{ s} \\ 122 \pm 24 & \text{for } \tau_e = 10,000 \text{ s} \end{cases} \quad (6.4)$$

with $E_{51.5} = 3 \times 10^{51}$ erg and $\Gamma_3 = 3$. The constraints on the jet energy and Lorentz factor derived in this way are shown in Fig. 6.1.

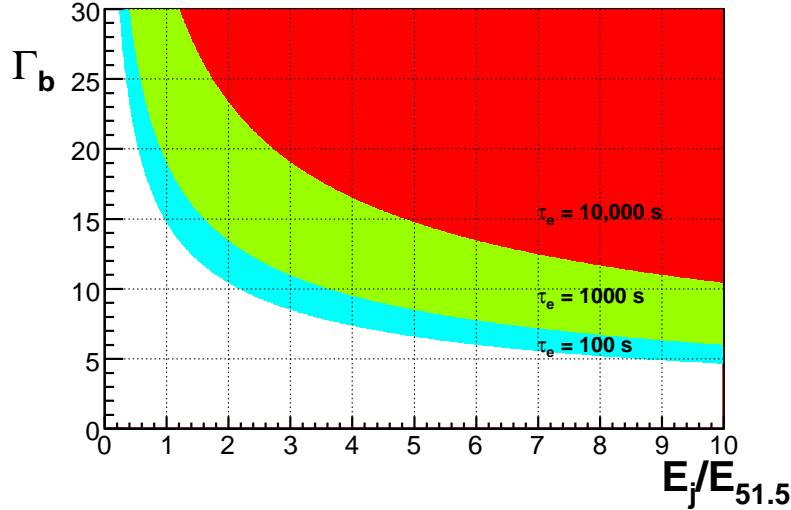


Figure 6.1: Constraints on the jet parameters E_j and Γ_b based on the assumption that only the normalization of Φ_ν depends on E_j and Γ_b . The colored regions are ruled out at 90% confidence level.

6.0.7 Summary and Outlook

This analysis has prepared the ground for future analyses in reaction to otherwise detected supernovae. The lowest model discovery factor of 12 reached with this analysis method, shows that even the small IceCube 22 detector would have detected SN 2008D with a probability of 50% if it had been ~ 3.5 times closer¹. The online multiplet trigger, scanning IceCube data for multiplets of collinear neutrinos, might soon lead to the first neutrino-triggered supernova detection. In such a case, the method presented in this work can be used to scan the vicinity of the trigger events. Roughly scaling the event expectation of SN 2008D in IceCube 22 to a supernovae at distances $\lesssim 10$ Mpc observed with IceCube 86, $\gtrsim 100$ neutrinos are expected. For the next nearby core collapse supernova, IceCube might thus be able to deliver “neutrino lightcurves” and approximate spectra. If a sufficient number of supernovae are observed in neutrinos, parameters of core collapse supernova models can be constrained, providing insights into the inner processes of these explosions.

All techniques used in this analysis are easily adaptable to the current detector configuration which allows for further studies to be completed on much shorter time scales (\sim weeks). Future analysis will greatly benefit from using the full sized 86 string detector with an at least 4 times greater sensitivity and possibly the inclusion of ν_e and ν_τ events which could increase the overall signal expectation by another factor of up to 3.

In conclusion, it appears to be only a matter of time until IceCube detects the first high energy supernova neutrinos. The author would be pleased if his work could contribute to such a detection in the future.

¹assuming that the slow jet model holds, and that neutrinos are emitted in a short 100 s burst

Appendix A

A.1 Important Symbols and Abbreviations

A.1.1 Abbreviations

AGN	Active Galactic Nucleus
BDT	Boosted Decision Tree
CORSIKA	COsmic Ray Simulations for KAscade, a cosmic ray air shower simulation software
GRB	Gamma Ray Burst
MDF	Model Discovery Factor
ROOT	no abbreviation; an object-oriented program and library for data analysis
SN (SNe)	Supernovae (Supernovae, Plural)

A.1.2 Symbols

δ	Significance in multiples $\delta = n\sigma$ of the Gaussian variance σ
p	p-value, probability that an observed event is consistent with the null hypothesis. For a significance level quoted in terms of $n\sigma$, the one-sided p-value is given by $p = \left[1 - \operatorname{erf}\left(n/\sqrt{2}\right)\right]/2$
$\operatorname{erf}(x)$	error function, defined by an integral, see [9, Ch. 32, Eq.(32.42)]
\mathcal{K}	Value assigned to an event by the Boosted Decision Tree classifier
\mathcal{K}^*	Value of \mathcal{K} where a selection cut $\mathcal{K} > \mathcal{K}^*$ is placed
ϵ_b, ϵ_s	background, signal efficiency
Φ	flux of muon neutrinos and anti neutrinos according to the slow jet model

A.2 Detailed Significances

N_1	N_2	N_3	$N_{1\wedge 2}$	$N_{2\wedge 3}$	$N_{1\wedge 2\wedge 3}$	n_1	n_2	n_3	Occurrences	$1 - p$	δ/σ
0	0	2	1	0	0	1	1	2	1	≈ 1	6.361
0	2	1	0	0	0	0	2	1	1	≈ 1	6.254
0	0	0	1	0	1	2	2	1	2	≈ 1	6.145
0	0	0	0	1	1	1	2	2	3	≈ 1	6.055
0	0	0	2	0	0	2	2	0	10	≈ 1	5.911
0	0	0	0	2	0	0	2	2	11	≈ 1	5.828
1	0	0	0	0	1	2	1	1	12	≈ 1	5.768
0	1	0	0	0	1	1	2	1	21	0.99999999	5.697
0	0	0	1	1	0	1	2	1	23	0.99999999	5.642
0	0	1	0	0	1	1	1	2	26	0.99999999	5.595
1	0	0	0	1	0	1	1	1	142	0.99999997	5.45
1	0	0	1	0	0	2	1	0	186	0.99999996	5.351
0	1	0	0	1	0	0	2	1	209	0.99999994	5.28
0	1	0	1	0	0	1	2	0	234	0.99999991	5.223
0	0	1	0	1	0	0	1	2	235	0.99999989	5.179
0	0	1	1	0	0	1	1	1	284	0.99999986	5.136
2	0	0	0	0	0	2	0	0	473	0.99999981	5.081
0	2	0	0	0	0	0	2	0	1119	0.99999997	4.992
1	1	0	0	0	0	1	1	0	1447	0.99999956	4.915
0	0	2	0	0	0	0	0	2	1528	0.99999994	4.857
1	0	1	0	0	0	1	0	1	1657	0.99999924	4.808
0	1	1	0	0	0	0	1	1	2615	0.99999898	4.749
0	0	0	0	0	1	1	1	1	49355	0.99999404	4.379
0	0	0	0	1	0	0	1	1	454971	0.99994854	3.884
0	0	0	1	0	0	1	1	0	508694	0.99989767	3.713
1	0	0	0	0	0	1	0	0	3.1011e+06	0.99958756	3.344
0	1	0	0	0	0	0	1	0	4.68935e+06	0.99911863	3.128
0	0	1	0	0	0	0	0	1	5.51451e+06	0.99856718	2.982
0	0	0	0	0	0	0	0	0	9.98567e+09	≈ 0	0

Table A.1: Detailed significances for all possible experimental scenarios taking into account that events can be tagged. Results shown for 10^{10} trials. N_i denotes the number of events *exclusively* found in window i ; $N_{i\wedge j}$ represents the number of events detectable in both, window i and window j ; and n_i stands for the total number of events seen in window i . Scenarios are ordered by decreasing significance. Horizontal lines mark decreases in the leading digit of the significance.

A.3 Data-Monte-Carlo Comparison

Figs. A.1 - A.1 show a comparison of:

- Data, 15.11 days, 3,500,000 events
- standard CORSIKA dataset 1541, 930,000 events, (“single CORSIKA”)
- coincident CORSIKA dataset 1731, 76,000 events, (“double CORSIKA”)
- atmospheric neutrino simulation dataset 1834, 946,000 events
- SN 2008D signal simulation, 120,000 events

All data was filtered to level 3. Note that all CORSIKA and atmospheric Monte Carlo is weighted and scaled to the data livetime, whereas the signal is weighted to the slow jet spectrum and scaled to the atmospheric Monte Carlo to facilitate comparing the two. The fact that the total CORSIKA distributions lie slightly below data, can be explained partly by the fact, that CORSIKA is compared to data from January, where trigger rates are elevated with respect to the annual mean (see Fig. 5.2). The small differences in the *shape* of the distributions could, however, not be remedied. Still, the discrepancy is within the systematic uncertainty for simulations discussed in Sec. 5.9.4 and agreement between simulation and data is remarkable.

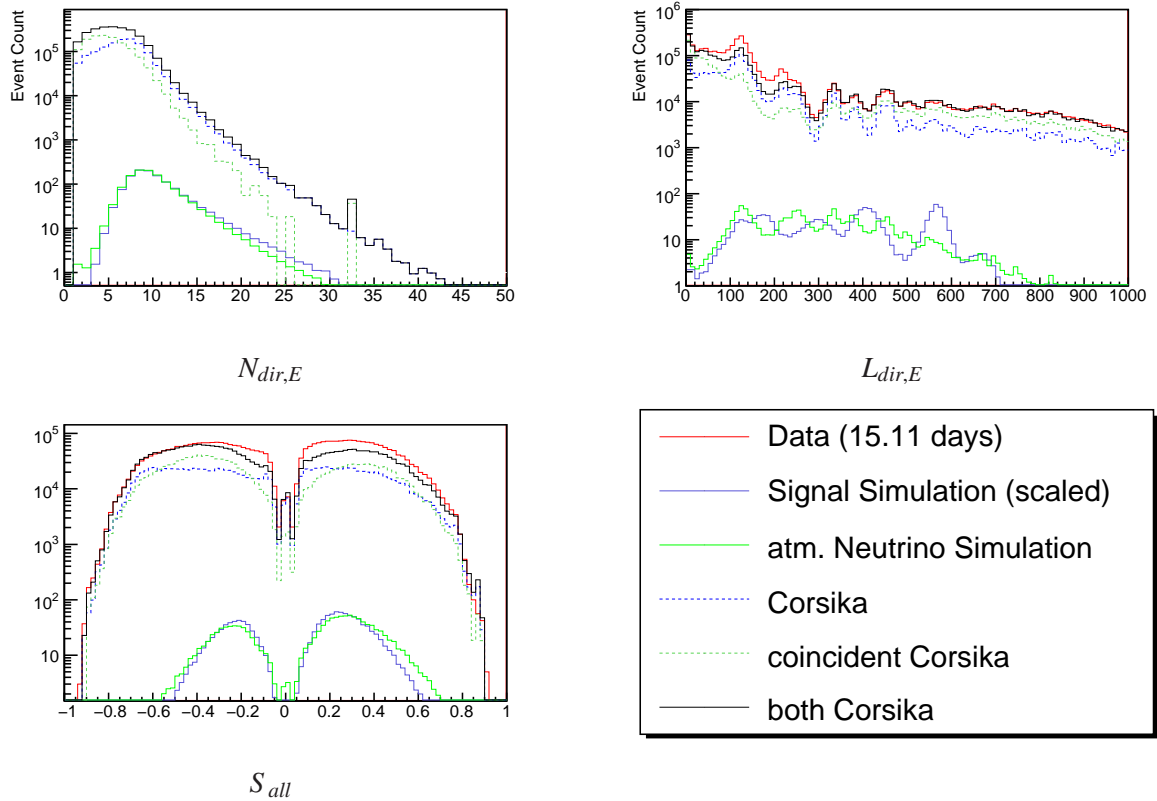


Figure A.1: Data - Monte Carlo comparison.

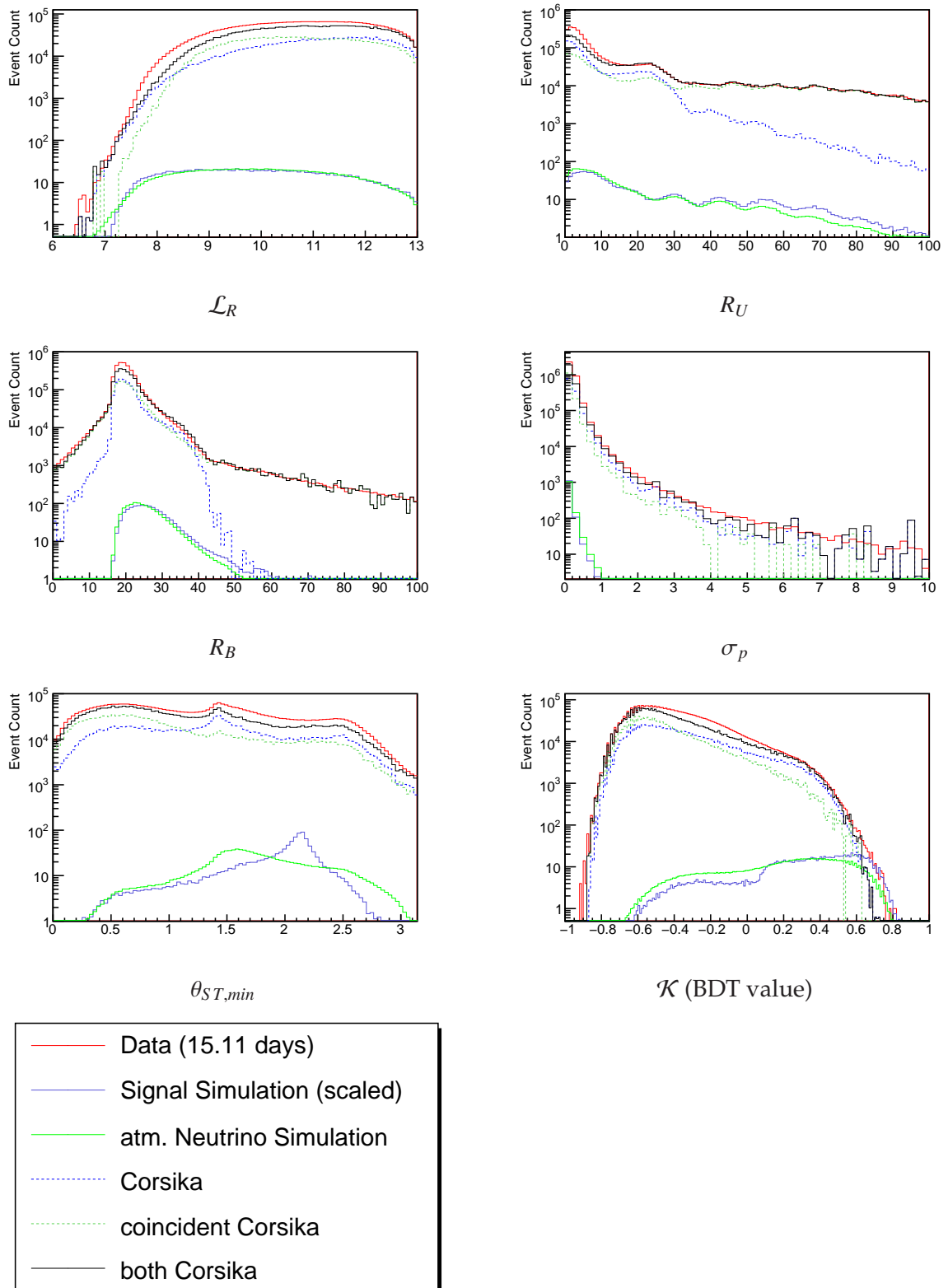


Figure A.2: Data - Monte Carlo comparison.

A.4 Comparison with Point Source Cuts

Some additional plots comparing the BDT cuts used in this analysis with the cuts used in the IceCube 22 Point Source Analysis [50] shall be presented here. They show, that the PS cuts would not have been suitable for this analysis.

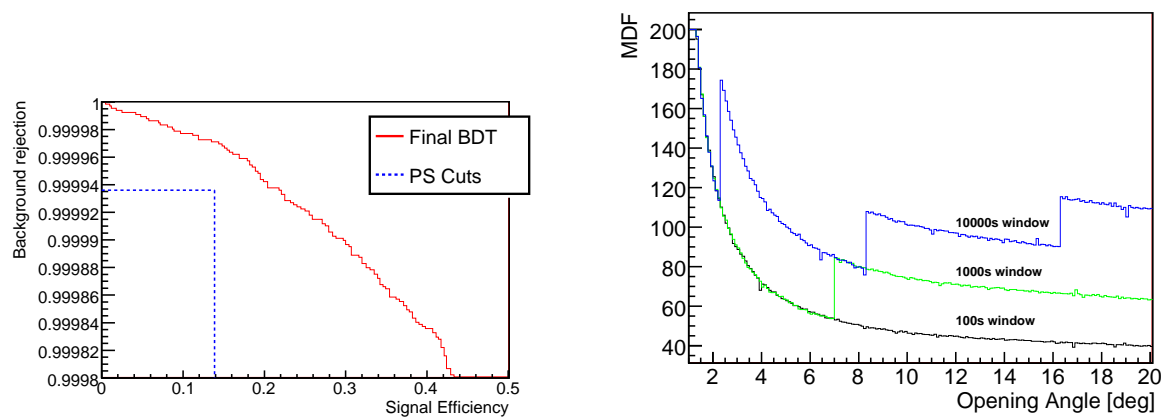


Figure A.3: Left: Zoomed comparison of the signal efficiency and background rejection using the PS cuts and using the BDT cut developed in this analysis. Right: Model discovery factor for three search windows all using the PS cuts. Even minimum values are ~ 4 times above those achieved in this analysis.

Appendix B

B.1 Acknowledgments

This analysis is really the result of the support by the entire IceCube collaboration, the brave men and women who are crazy enough to go to the South Pole drill two and a half kilometers into the ice and sink millions worth of equipment into the holes just to see that one first comic neutrino. I am glad to have been a part of this collaboration.

In chronological order, I would like to thank: Buford Price, Kirill Filimonov, Kurt Woschnagg, Justin Vandenbroucke, Michelangelo D'Agostino, and Ingacio Taboada for introducing me into the world of IceCube and giving me this exciting analysis topic. I would like to thank Kirill and Ignacio in particular for their continued support.

Next, I wish to thank Marek Kowalski for immediately integrating me into the IceCube group at Humboldt University and giving me a chance to continue this analysis and expand it into a Diploma thesis.

Moreover, I would like to thank Anna Franckowiak for her valuable feedback on my analysis and Sebastian Panknin for his generous programming help.

I also would like to thank the folks at Desy Zeuthen, namely Jose Bazo, Robert Franke, and Fabian Kislat for their invaluable support in software issues.

I especially thank my parents for their financial and moral support; also my brother, my sister, and my friend Alsino Skowronnek for not giving up on me even in times when I ceased to be a social being.

I also owe my gratitude to the referees of this analysis, Peter Redl, Alexander Kappes, and Ignacio Taboado in the GRB working group and Kyler Kuehn and Chad Finley in the unblinding process.

Last but not least, I thank the referees of this Diplomarbeit, Marek Kowalski and Heiko Lacker, for fairly judging my work and for possibly being the only people who actually read the whole thesis.

B.2 Erklärung

Hiermit versichere ich, dass ich diese Arbeit nur unter Zuhilfenahme der angegebenen Quellen und Hilfsmittel selbstständig angefertigt habe.

Berlin, 28. Februar 2010

Niklaus Kemming

Bibliography

- [1] D. A. Green, F. R. Stephenson, "The Historical Supernovae", astro-ph/0301603v1, published in *Supernovae and Gamma Ray Bursters*, Springer-Verlag (2003)
- [2] P. F. Winkler, "SN1006: a thousand-year perspective", *Highlights of Astronomy*, Vol. **14** (2006)
- [3] K. Hirata et al., "Observation of a neutrino burst from the supernova SN1987A", *Phys. Rev. Lett.* **58** (1987)
- [4] W. Pauli, Letter to Lise Meitner, December 4, 1930, *The CERN Pauli Archive*
- [5] K. Zuber, "Neutrino Physics", *Institute of Physics Publishing* (2004)
- [6] C.L. Cowan, Jr., F. Reines et al., "Detection of the Free Neutrino: A Confirmation", *Science* **124** (1956)
- [7] G. Danby et al., "Observation of High-Energy Neutrino Reactions and the Existence of Two Kinds of Neutrinos", *Phys.Rev.Lett.* **9** (1962)
- [8] DONUT Collaboration, K. Kodama et al., "Observation of tau neutrino interactions", *Physics Letters B* **504** (2001)
- [9] C. Amsler et al. (Particle Data Group), "Review of Particle Physics", *Physics Letters B*, **667**, 1 (2008)
- [10] S. Weinberg, "The Making of the Standard Model Authors: Steven Weinberg", *Eur. Phys. J. C* **34** (2004)
- [11] F. Halzen, A.D. "Quarks and Leptons", *Wiley-VCH*, Ed. 1 (1984)
- [12] M. Peskin and D. V. Schroeder, "An Introduction to Quantum Field Theory", *Westview Press* (1995)
- [13] J. Becker, "High-energy neutrinos in the context of multimessenger astrophysics", Preprint submitted to *Physics Reports*, astro-ph:0710.1557v2 (2005)
- [14] P. Berghaus, "Direct Measurement of the Atmospheric Muon Energy Spectrum with IceCube", *Proceedings of the 31st ICRC, Lodz* (2009)
- [15] H. Geenen for the AMANDA Collaboration, "Atmospheric Neutrino and Muon Spectra Measured with the AMANDA-II Detector", *Proceedings of the 28th International Cosmic Ray Conference* (2003)

- [16] R. Lauer for the IceCube Collaboration, "Extended search for point sources of neutrinos below and above the horizon: Covering energies from TeV to EeV with IceCube", *Int.J.Mod.Phys.D* **18** (2009)
- [17] The Pierre Auger Collaboration, "Measurement of the energy spectrum of cosmic rays above 10^{18} eV using the Pierre Auger Observatory", accepted for publication in *Physics Letters B*, astro-ph.HE:1002.1975v1 (2010)
- [18] R. W. Klebesadel et al., "Observations of Gamma-Ray Bursts of Cosmic Origin", *Astrophysical Journal* **182** (1973)
- [19] W. S. Paciesas et al., "The Fourth BATSE Gamma-Ray Burst Catalog (Revised)", *The Astrophysical Journal Supplement Series* **122**, (1999)
- [20] L. Amati et al., "Intrinsic spectra and energetics of BeppoSAX Gamma-Ray Bursts with known redshifts", *Astronomy&Astrophysics* 390 (2002)
- [21] T. Prian, "Gamma-Ray Bursts and the Fireball Model", *Phys.Rept.* **314** (1999)
- [22] E. Waxman, J. Bahcall, "High Energy Neutrinos from Cosmological Gamma-Ray Burst Fireballs", *Phys.Rev.Lett.* **78** (1997)
- [23] P. Mészáros, S. Razzaque, "Gamma-ray Bursts and High Energy Neutrinos", *Nuclear Physics B* **145** (2005)
- [24] J. G. Kirk et al., "Particle acceleration and relativistic shocks", *J. Phys. G: Nucl. Part. Phys.* **25** (1999)
- [25] M. Schmidt, "3C 273 : A Star-Like Object with Large Red-Shift", *Nature* **197** (1963)
- [26] A. Weigert, H.J. Wendker, L. Wisotzki, "Astronomie und Astrophysik", Wiley-VCH (2009)
- [27] F.W. Stecker, C. Done, "High-energy neutrinos from active galactic nuclei", *Phys. Rev. Lett.* **66** (1991)
- [28] Adam Burrows, "Supernova explosions in the Universe", *Nature* **403**, 727 (2000)
- [29] T. Kowarik et al., "Supernova Search with the AMANDA / IceCube Detectors", *Proceedings of the 31st ICRC, Łódz* (2009)
- [30] E. Bissaldi et al., "The connection between Gamma-ray bursts and Supernovae Ib/c", accepted by *Astronomy&Astrophysics* (2009)
- [31] S. Woosley, J. Bloom, "The Supernova Gamma-Ray Burst Connection", *Annual Rev. Astron. Astrophys.* (2006)
- [32] R. Yamazakia, "A unified model of short and long gamma-ray bursts, X-ray rich gamma-ray bursts, and X-ray flashes", *The Astrophysical Journal*, 607 (2004)
- [33] D. Q. Lamb et al., "A unified jet model of X-ray flashes and γ -ray bursts", *New Astronomy Reviews* **48** (2004)
- [34] T. J. Galama et al. "An unusual supernova in the error box of the γ -ray burst of 25 April 1998", *Nature* **395** (1998)

- [35] J. Hjorth et al., "A very energetic supernova associated with the γ -ray burst of 29 March 2003", *Nature* **423** (2003)
- [36] Malesani, J. et al., "SN 2003lw and GRB 031203: a bright supernova for a faint gamma-ray burst", *Astrophys. J.* **609** (2004)
- [37] E. Pian et al., "An optical supernova associated with the X-ray flash XRF 060218", *Nature* **442** (2006)
- [38] Z. Paragi et al., "A mildly relativistic radio jet from the otherwise normal Type Ic Supernova 2007gr", *Nature* **463**, (2010)
- [39] A. Soderberg et al., "An extremely luminous X-ray outburst at the birth of a supernova", *Nature* **453** (2008)
- [40] D. Pooley, A. Soderberg, "Chandra detection of the Type Ibc SNe 2007uy and 2008D in NGC 2770", *The Astronomer's Telegram* **1368**, 1 (2008)
- [41] E. Waxman, A. Loeb, "TeV Neutrinos and GeV Photons from Shock Breakout in Supernovae", *Phys. Rev. Lett.* **87** (2001)
- [42] S. Razzaque, P. Meszaros, E. Waxman, "High Energy Neutrinos from a Slow Jet Model of Core Collapse Supernovae", *Modern Physics Letters A* **20** (2005)
- [43] S. Ando, J.F. Beacom, "Revealing the Supernova–Gamma-Ray Burst Connection with TeV Neutrinos", *Phys.Rev.Lett.* **95** (2005)
- [44] Personal communication with John Beacom (2009)
- [45] P. Mazzali et al., "The Metamorphosis of Supernova SN 2008D/XRF 080109: A Link Between Supernovae and GRBs/Hypernovae", *Science* **321** (2008)
- [46] R. Abbasi et al., "The IceCube data acquisition system: Signal capture, digitization, and timestamping", *Nucl. Instrum. and Meth. A* **601** (2009)
- [47] J. Lundberg et al., "Light tracking through ice and water – Scattering and absorption in heterogeneous media with PHOTONICS", *Nucl. Instrum. Meth. A* **581** (2007)
- [48] AMANDA Collaboration, J. Ahrens et al., "Muon track reconstruction and data selection techniques in AMANDA," *Nucl. Instrum. Meth. A* **524** (2004)
- [49] D. Pandel, "Bestimmung von Wasser- und Detektorparametern und Rekonstruktion von Myonen bis 100 TeV mit dem Baikal-Neutrino teleskop NT-72", *Diplomarbeit*, Humboldt-Universität zu Berlin (1996)
- [50] The IceCube Collaboration, "First Neutrino Point-Source Results from the 22 String Ice-Cube Detector", *ApJ* **701** (2009)
- [51] M. Honda, T. Kajita, "Calculation of atmospheric neutrino flux using the interaction model calibrated with atmospheric muon data", *Phys.Rev.D* **75** (2007)
- [52] G. Fiorentini, V.A. Naumov, F.L. Villante, "Atmospheric neutrino flux supported by recent muon experiments", *Phys.Lett. B* **510**, (2001)

- [53] J. R. Hoerandel, "Models of the knee in the energy spectrum of cosmic rays", *Astropart. Phys.*, **21** (2004)
- [54] M. Kowalski, A. Gazizov, "High Energy Neutrino Generator for Neutrino Telescopes", *Computer Physics Communications* **172**, 3 (2005)
- [55] H. L. Lai et al. "Global QCD Analysis of Parton Structure of the Nucleon: CTEQ5 Parton Distributions", *Eur. Phys. J. C* **12** (2000)
- [56] J. Pumplin et al., "New generation of parton distributions with uncertainties from global QCD analysis", *JHEP*, **07**:012 (2002)
- [57] A. Franckowiak et al., "Optical follow-up of high-energy neutrinos detected by IceCube", *Proceedings of the 31st ICRC, Lodz, Poland, July 2009*
- [58] IceCube Collaboration, "IceCube Preliminary Design Document" (2001)
<http://www.icecube.wisc.edu/science/publications/pdd/pdd.pdf>
- [59] U. Jacob AND T. Piran, "Neutrinos from gamma-ray bursts as a tool to explore quantum-gravity-induced Lorentz violation", *nature physics* Vol. **3** (2007)
- [60] M. D'Agostino, "First Evidence For Atmospheric Neutrino-Induced Cascades with the IceCube Detector", PhD Thesis, astro-ph.HE:0910.2555v1 (2009)
- [61] J. Learned, K. Mannheim, "High-energy neutrino astrophysics", *Ann. Rev. Nucl. Part. Sci.* **50** (2000)
- [62] B. Price, K. Woschnagg, D. Chirkin, "Age vs depth of glacial ice at South Pole", *Geophysical Research Letters*, **27** (2000)
- [63] M. Ackermann et al., "Optical properties of deep glacial ice at the South Pole", *J. Geophys. Res.* **111** (2006)
- [64] G.J. Feldman, R.D. Cousins, "A Unified Approach to the Classical Statistical Analysis of Small Signals", *Phys. Rev. D*:**57** (1998)
- [65] J. Bazo, E. Bernadini, "IC 22 Point Source Search, Systematic Errors", IceCube internal webpage, http://wiki.icecube.wisc.edu/index.php/IC22_Point_Source_Search
- [66] A. Kappes, "Systematics for IC9 Analysis of GRB080319B", IceCube internal webpage, http://www.icecube.wisc.edu/~kappes/icecube_restricted/GRB080319B/systematicerrors.html
- [67] T. Montaruli, I. Sokalski, "Influence of neutrino interaction and muon propagation media neutrino-induced muon rates in deep underwater detectors", IceCube internal document, https://docushare.icecube.wisc.edu/dsweb/Get/Document-48841/Montaruli_and_Sokalski_Media_Study.pdf
- [68] D. Chirkin, W. Rhode, "Propagating leptons through matter with Muon Monte Carlo (MMC)", hep-ph/0407075v2 (2008)